

TRANSPORT AND GUEST-HOST INTERACTIONS IN
AMORPHOUS AND CRYSTALLINE ICE

by

Sergey Malyk

A Dissertation Presented to the
FACULTY OF THE GRADUATE SCHOOL
UNIVERSITY OF SOUTHERN CALIFORNIA
In Partial Fulfillment of the
Requirements for the Degree
DOCTOR OF PHILOSOPHY
(CHEMISTRY)

May 2009

Copyright 2009

Sergey Malyk

Dedication

To my wife Olga and my son Alexander

Acknowledgements

First of all, I would like to thank my research advisors, Curt Wittig and Hanna Reisler. I am grateful to them for giving me the opportunity to work in their research lab and for their wise guidance and support throughout the years. Because of to them I have acquired many valuable skills and greatly improved my ability to think and work independently. I would also like to thank all of the other professors in the USC chemistry department that have taught and helped me along the way.

During my time here I have been able to work alongside of some great people: Samantha Hawkins, George Kumi and Oscar Rebolledo-Mayoral. I highly value the experience of working with these individuals; and it was nice to have coworkers to lighten the mood during those days when experiments were not working out as planned.

It is my pleasure to thank fellow graduate students and postdoctorals from the Chemistry department for support, friendship, smiles, fruitful discussions, and their readiness to lend us some scientific equipment. Specifically I would like thank Andrew Mollner, Anton Zadorozhnyy, Askat Jailaubekov, Blithe Casterline, Boris Karpichev, Chris Nemirow, Christi Chester, Daniil Stolyarov, Dmitry Skvortsov, Elena Polyakova, Guosheng Li, Igor Fedorov, Jordan Fine, Kadir Diri, Kirill Kuyanov, Laura Edwards, Lee-Ann Smith-Freeman, Mikhail Slipchenko, Misha Ryazanov, Nikolay Markovskiy, Piotr Pieniazek, Russell Sliter, Sergey Levchenko, Vadim Mozhayskiy, William Schroeder, and Zhou Lu.

I would like to specially thank Andrew Mollner, Chris Nemirow, Christi Chester , Oscar Rebolledo-Mayoral and William Schroeder for proofreading some parts of this dissertation.

Our experimental work would have been incredibly more difficult without the help of Ross Lewis from our electronics shop and Don Wiggins from the USC Machine shop. Also, thank you to all the support staff at the USC Chemistry department, especially to Danielle Hayes, Heather Meunier-Connor, Michele Dea, Valerie Childress and Yuki Yabuta.

Finally, I would like to thank my family for their unwavering support and encouragement over these years.

Table of Contents

Dedication	ii
Acknowledgements	iii
List of Tables	vii
List of Figures	viii
Abstract	xii
Chapter 1: Introduction	1
1.1 Properties of Amorphous Solid Water	2
1.2 Trapping and Release of Guest Molecules by ASW	10
1.3 References	14
Chapter 2: Experimental Details	19
2.1 UHV System	19
2.2 FTIR Chamber	21
2.3 FTIR Setup	23
2.4 The Surface Manipulator	25
2.5 Substrate Preparation	27
2.6 Sample Preparation	28
2.7 Sample Holder	29
2.8 Laser Induced Desorption Setup	32
2.9 Time of Flight Mass Spectrometer	35
2.10 References	38
Chapter 3: Infrared Laser Source Based on Gaseous Deuterium Raman Shifter	39
3.1 Overview	39
3.2 Experimental Setup	44
3.3 Optimum Conditions for the Second Stokes Generation	48
3.4 References	56

Chapter 4: Trapping and Release of CO₂ Guest Molecules by Amorphous Ice	57
4.1 Introduction	57
4.2 Experimental	59
4.3 Results	62
4.4 Discussion	72
4.5 Summary	79
4.6 References	80
Chapter 5: Laser Induced Desorption of Water Molecules: Preliminary Results and Future Work	83
5.1 Introduction	83
5.2 Experimental Details	86
5.3 Preliminary Results and Discussion	88
5.4 Future Work	98
5.5 References	103
Bibliography	106

List of Tables

Table 3.1	Wavelengths and frequencies for Raman output.	47
Table 3.2	Properties of common optical window materials [10].	47

List of Figures

- Figure 2.1** Drawing of the UHV chamber. The UHV system has three levels with the surface manipulator attached to the upper level. The entire system is pumped by a turbomolecular pump connected to the level B. 20
- Figure 2.2** A schematic of FTIR chamber. 22
- Figure 2.3** Schematic drawing of the optical setup for FTIR spectroscopy. The entire beam path is purged to remove atmospheric water and carbon dioxide. 24
- Figure 2.4** Schematic of the custom-made surface manipulator. The stainless steel tube is used as a liquid nitrogen reservoir with a copper piece silver-brazed to the end. 26
- Figure 2.5** Drawing of a sample holder (most recent design). The sample holder consists of two main copper parts labeled A and B. The surface resides on a piece C made from copper foil that is attached to A using a screw. The homemade resistive heating element D is glued to the back of the copper foil piece C. 31
- Figure 2.6** Schematic of level B of the UHV chamber. The TOF mass spectrometer is attached to the UHV chamber through an adapter flange. 33
- Figure 2.7** Schematic of linear time-of-flight (TOF) mass spectrometer. 36
- Figure 3.1** Energy diagram for Stokes and Anti-Stokes Raman processes. 41
- Figure 3.2** A schematic of the Raman shifter. 45
- Figure 3.3** Dependence of the 2nd Stokes pulse energy and 2nd Stokes conversion efficiency on D_2 pressure at 150 mJ/pulse pump pulse energy. 50
- Figure 3.4** Dependence of the 2nd Stokes energy on pump pulse energy at D_2 pressure of 750 PSI. 51

- Figure 3.5** Distributions of the 2nd Stokes energy for ~250 consecutive laser shots at three different pump energies. 54
- Figure 4.1** $^{13}\text{CO}_2$ was deposited (4×10^{-8} Torr, 3 minutes) onto MgO(100) at 90 K, at which time FTIR and TPD traces were recorded. Entries (a) and (b) show the $^{13}\text{CO}_2$ ν_3 spectral region and the TPD trace, respectively. The LO and TO modes of the $^{13}\text{CO}_2$ film are indicated in (a). TPD was carried out by heating the surface at 1 K / s while monitoring $m/e = 45$. 64
- Figure 4.2** $^{13}\text{CO}_2$ was deposited (4×10^{-8} Torr, 30 s) onto an ASW film of ~40 layers (5×10^{-8} Torr, 8 minutes). H_2O and $^{13}\text{CO}_2$ desorption was monitored at $m/e = 18$ and 45, respectively. (a) and (b) show TPD traces for CO_2 and H_2O , respectively. Note that the H_2O TPD trace is scaled by a factor of 0.1. The scale factor of 0.3 shown in (a) is for comparison with Figures 4.3 - 4.5. 65
- Figure 4.3** (a) FTIR spectra (p -polarization) of (i) ASW film (~40 layers) exposed to $^{13}\text{CO}_2$ and (ii) ASW film (~40 layers) deposited onto $^{13}\text{CO}_2$ film. Each sample was annealed to 115 K and re-cooled to 90 K. CO_2 was deposited at 4×10^{-8} Torr for 30 s. The inset shows the expanded scale of the $^{13}\text{CO}_2$ ν_3 region. (b) TPD spectra of $^{13}\text{CO}_2$ recorded for the samples in (a): (i) ASW film (~40 layers) exposed to $^{13}\text{CO}_2$ and (ii) ASW film deposited onto $^{13}\text{CO}_2$ film (TPD spectra were recorded after FTIR spectra). The scale factor of 1.0 is for comparison with Figures 4.2, 4.4, and 4.5. 67

Figure 4.4 TPD and FTIR spectra of co-deposited (through separate dosers) $^{13}\text{CO}_2$ with H_2O : H_2O pressures and exposure times were the same in all experiments (5×10^{-8} Torr, 8 minutes); $^{13}\text{CO}_2$ pressures are given as fractions of the H_2O pressure $P_{\text{CO}_2}/P_{\text{H}_2\text{O}}$. Samples were annealed to 115 K and re-cooled to 90 K before recording each trace. Spectra are offset for clarity. (a) FTIR spectra (*p*-polarization); the bumps at 2256 cm^{-1} are due to $^{13}\text{C}^{18}\text{O}^{16}\text{O}$ (b) TPD spectra; the inset shows an expanded scale of the $^{13}\text{CO}_2$ codesorption peak (*i.e.*, $^{13}\text{CO}_2$ desorbing with the polycrystalline water film). TPD traces of H_2O were approximately the same. 69

Figure 4.5 (a) FTIR spectra (*p*-polarization): (i) $^{13}\text{CO}_2$ deposited (4×10^{-8} Torr, 30 s) onto ASW film; (ii) $^{13}\text{CO}_2$ deposited (4×10^{-8} Torr, 30 s) before formation of ASW film; and (iii) $^{13}\text{CO}_2$ (2×10^{-9} Torr) codeposited with H_2O . Each sample was annealed to 165 K and re-cooled to 90 K. The H_2O exposure was approximately the same (5×10^{-8} Torr, 8 minutes) for all experiments. The inset shows the expanded scale of the $^{13}\text{CO}_2$ ν_3 region. (b) TPD spectra were recorded for the samples in (a) immediately after recording the FTIR spectra. 71

Figure 5.1 The H_2O LID relative desorption yield versus the number of laser pulses obtained for samples of ~ 3000 layers of ASW ice film (averaging results from 9 experiments). The IR laser energy was ~ 1.5 mJ. 89

Figure 5.2 A sequence of 96 TOF mass spectra ($5\ \mu\text{s}$ intervals) of water desorbing from the ASW film (~ 3000 layers) following the IR laser pulse (1.5 mJ) at time zero. The inset shows an expanded scale of a single TOF spectrum from the sequence with masses assigned. 93

Figure 5.3 The velocity distribution of water molecules desorbing from the ASW film (~ 3000 layers) following the IR laser pulse (1.5 mJ) at time zero. The smooth thick line shows the best fit by a combination of two Maxwellian distributions. 94

Figure 5.4 Fabrication of isolated regions of ASW on a supporting substrate. (a) Stainless steel mesh is placed in front of the ASW film, and the film is irradiated. (b) All the ASW in open areas desorb, leaving the structure shown in blue. (c), (d) To form isolated columns of ASW with the axes of the columns parallel to the y-axis shown, the mesh can be translated along the y-axis. After translation the substrate is irradiated to desorb any exposed ASW. (e), (f) To form isolated areas of ASW (blue squares), this process has to be repeated along x-axis.

101

Abstract

Interactions of $^{13}\text{CO}_2$ guest molecules with vapor-deposited porous H_2O ices have been examined using temperature programmed desorption (TPD) and Fourier transform infrared (FTIR) techniques. Specifically, the trapping and release of $^{13}\text{CO}_2$ by amorphous solid water (ASW) has been studied.

Samples were prepared by: (i) depositing $^{13}\text{CO}_2$ on top of ASW; depositing $^{13}\text{CO}_2$ underneath ASW; and (iii) co-depositing $^{13}\text{CO}_2$ and H_2O during ASW formation. The use of $^{13}\text{CO}_2$ eliminates problems with background $^{12}\text{CO}_2$. Some of the deposited $^{13}\text{CO}_2$ becomes trapped when the ice film is annealed. The amount of $^{13}\text{CO}_2$ trapped in the film depends on the deposition method (*i.e.*, on top of the ASW, underneath the ASW, and co-deposition).

The release of trapped molecules occurs in two stages. The majority of the trapped $^{13}\text{CO}_2$ escapes during the ASW-to-cubic ice phase transition at 165 K and the rest desorbs together with the cubic ice film at 185 K. We speculate that the presence of $^{13}\text{CO}_2$ at temperatures up to at 185 K is due to $^{13}\text{CO}_2$ that is trapped in cavities within the ASW film. These cavities are similar to ones that trap the $^{13}\text{CO}_2$ that is released during crystallization. The difference is that $^{13}\text{CO}_2$ that remains at temperatures up to 185 K does not access escape pathways to the surface during crystallization.

The UHV system was modified to incorporate a novel laser induced desorption (LID) technique in addition to TPD and FTIR. The source of the IR laser radiation

at 2.92 μm based on the deuterium gas Raman shifter was developed as a part of the LID setup. Preliminary results of the H_2O LID from the ASW films are discussed. Future experiments to investigate the phase transformations of ASW and participation of boundaries in it, dopant transport, and lateral flow of amorphous materials and supercooled liquids are outlined.

Chapter 1: Introduction

Water is the most abundant compound on the surface of the earth and it is the principal constituent of all living organisms. Depending on pressure and temperature, water can be found in gas, liquid, and solid phases. It forms more solid phases (each with distinct properties) than any other known substance [1]. The predominant interaction that holds water molecules together in the solid form is hydrogen bonding [1,2], which is a difficult interaction to model [3]. It is still not fully understood how to bridge the gap between the molecular properties of water and the corresponding macroscopic behavior [4].

Solid water, or ice, has attracted significant attention as an important system for heterogeneous reactions [5,6]. Surface interactions can lower activation energy barriers for reactions that would not normally occur in the gas phase. Some of the well-studied heterogeneous interactions involve reactions on polar stratospheric clouds between the water ice surface and halogens and acids [3,5].

The amorphous form of solid water (a glassy, solid form) has gained significant attention. Amorphous ice (AI), also referred to as amorphous solid water (ASW), is the most abundant form of water in the universe [7]. It is believed to be the major constituent of comets, interstellar clouds, and planetary rings [8,9]. Interactions between ASW and an adsorbate have important implications to atmospheric and astrophysical science [8,10-14]. In particular, the kinetics of adsorption, desorption, trapping and release of an adsorbate interacting with ASW are important if we are

to quantitatively model macroscopic processes [3]. It is also believed that a better understanding of the nature of the ASW phase will aid in the development of a complete, comprehensive picture of liquid water physics and other amorphous solid systems [7,10,15,16].

1.1 Properties of Amorphous Solid Water

The idea that there is an amorphous solid form of water was first proposed in 1935 when Burton and Oliver [17] deposited water molecules onto a cold copper plate ($T < 130$ K) and showed that the X-ray diffraction pattern of the deposited sample lacked any Bragg peaks. ASW is a solid phase of water that is metastable with respect to its crystalline phase [10,16], because it is "trapped" in a configuration that has a higher free energy than its equilibrium crystalline configuration [18]. Amorphous solids are most often formed when a liquid is cooled so fast that crystallization does not occur prior to the system reaching a temperature where the structural relaxation timescale is long compared to the experimental timescale [19]. The temperature where this occurs is called the glass transition temperature (T_g).

Amorphous ice can be formed via several methods: vapor deposition onto a cold substrate ($T < 130$ K) [17,20], high pressure amorphization of crystalline ice (high density amorphous, HDA) [21,22], rapid cooling of water droplets (hyperquenched glassy water, HGW) [15,23], and electron beam or radiation induced amorphization of crystalline ice (HDA) [24]. Some authors have argued that several different

forms of amorphous ice exist [16,25-29], which are distinguished by specific physical properties, rather than by a measure of long-range disorder [30]. One of these properties is the density. There is a high-density form of ASW (1.1 g/cm^3), which grows by vapor deposition at $T \leq 10 \text{ K}$ [25]. The high-density phase transforms into a low-density form of ASW (0.94 g/cm^3) at $\sim 115 \text{ K}$ [26]. The pressurizing of crystalline (hexagonal) ice produces an AI that has a density 1.31 g/cm^3 [21]. This ice stays amorphous after releasing the pressure and transforms slowly into an ice with a density 1.17 g/cm^3 [31]. It is still not clear whether these varying densities of ASW are due to several different forms of ASW or a manifestation of some other effect.

The porosity of ASW plays a significant role for transport of molecules through the ASW media and heterogeneous processes. In general, porosity is a measure of the void spaces in a material, and is measured as a normalized fraction. The porosity of ASW may be deduced from measurements of the index of refraction, which is related to the porosity by the Lorentz-Lorentz relation [32]. The range of values reported in the literature is very wide (from 0.05 to 0.6) [33,34]. This shows that the typical assumption of ASW always being porous does not universally apply.

Quite often the surface area of ASW is used to characterize its porosity. The surface area may be derived from nitrogen adsorption experiments at low temperatures ($< 30 \text{ K}$) [12,35,36]. At this temperature only a single monolayer of nitrogen is adsorbed on the walls of the pores. Thus, the surface area of ASW can

be obtained by measuring the quantity of gas released as the ice is heated [19]. The information obtained in these experiments is analogous to isothermal gas adsorption measurements, often called BET isotherms, which are typically done at higher temperatures [15,37-39]. It is important to note that gas adsorption measurements provide only information on the pores that are connected to the surface of the ice film, but not of the enclosed pores.

Many studies reported widely varying values (from 0.1 to 3000 m²/g) for the effective surface area for gas adsorption [12,15,28,35,40-42]. Recently Kimmel et al. [36] pointed out that the different values of density and surface area reported in different studies could be explained by an increase of porosity with incident growth angle of the water molecules from the gas phase [12,36]. ASW films with structures varying from nonporous to highly porous can be grown by increasing the angle of incidence of the collimated H₂O molecular beam [12,36]. This effect can be qualitatively explained by using a simple ballistic deposition model [36]. At glancing angles, random height differences that arise during the initial film growth can block the incoming flux of molecules essentially creating shadows that result in void space in the shadowed regions [36]. The main assumption of this model is that the surface and bulk diffusion at low temperatures are very slow compared to the incident flux of molecules, i.e., the incoming molecules "stick" to the surface where they "hit" it [36]. It is not yet fully understood how the kinetic and condensation energy of incoming water molecules dissipate in space and time upon collisions with the surface [30].

Several studies have shown that the porosity of ASW depends on the deposition temperature [36] and its thermal history [20,36,43]. Kimmel et al. showed that despite the high incident growth angle, ASW films grow dense at high deposition temperatures ($T > 100$ K) [36]. This result is consistent with the ballistic deposition model where the increased surface temperature leads to enhanced diffusion of incident molecules upon collision with the surface [36]. They also reported that the surface area decreases irreversibly for annealed ASW films [36]. Similarly, Manca et al. observed changes in the ASW spectral features and decrease in the ASW surface area upon annealing (56 K to 140 K) [43]. Ghormey observed heat release when the ASW film was heated (for the first time) from 20 K to 77 K [44]. This heat release signals structural relaxation towards equilibrium [44]. It was proposed that an increase in ASW temperature induces slight molecular rearrangements that result in permanent pore closure [35].

To predict the thermal evolution of ASW, it is important to know its thermal conductivity. As expected from its microscopic disorder, the thermal conductivity of amorphous ice, like other amorphous solids, is much smaller than that of crystalline ice [33]. In addition, porosity, which increases phonon scattering, will further reduce the thermal conductivity [45]. Kouchi reported a value of the thermal conductivity of ASW three orders of magnitude smaller than the estimate for a non-porous amorphous ice [46,47]. The difference in the reported values of thermal conductivity of ASW is attributed to variations in sample porosity and measurement difficulties [33,45]. The small value for the porous ASW thermal

conductivity suggests that the heat transferred by radiation and desorbed gases might be also important in certain situations [46].

ASW films will irreversibly crystallize when heated to a high enough temperature for a sufficient amount of time. The metastable ASW phase irreversibly converts to the more stable cubic ice (CI) [1]. Cubic ice is also a metastable phase with respect to hexagonal ice (HI) [1]. The first report on CI dates back to 1941 when Konig observed that the diffraction pattern of ASW, which consists of diffuse rings, changed upon heating (~ 140 K) into a pattern consisting of sharp rings (consistent with the cubic structure of the diamond type) [1]. Unlike ASW, cubic ice shows properties of a single well defined phase. It is believed to be nonporous with a density ~ 0.94 g/cm³[1,16].

Typically, crystallization occurs between 140 and 170 K with crystallization times depending on experimental parameters such as the temperature ramp [20,28,30,48,49]. The crystallization temperature (T_c) represents a characteristic temperature at which the crystallization rate of ASW becomes significantly high so that the time required for complete conversion of an ASW sample to crystalline form is shorter than the typical time scale of an experiment (10–200 s). The crystallization kinetics of ASW have been studied via several techniques including electron diffraction [8,50], Fourier transform infrared spectroscopy (FTIR) [49,51,52], and temperature programmed desorption (TPD) [53,54]. The amorphous phase has a higher desorption rate than cubic ice because of the excess free energy of the metastable phase [54,55]. The change in the desorption rate

during conversion from amorphous to crystalline phase results in a bump in the TPD spectrum [54,55]. TPD is only sensitive to the outer surface of the thin ice film. Infrared (IR) spectra of ice also provide clear indication of ASW-to-crystalline phase transition and, unlike TPD, FTIR is sensitive to changes that occur within the entire ice film [51,52].

In most studies, it was concluded that crystallization proceeds via homogeneous nucleation and isotropic growth of crystallites [20,54,56]. However, the studies reach different conclusions as to whether transfer of H₂O molecules across the crystal-amorphous matrix interface [54,57,58] or long-range diffusion controls the rate of grain growth [51,58,59]. Dohnalek and coworkers observed a dramatic acceleration of the crystallization rate in thin (< 10 nm) ASW films supported on a crystalline ice substrate [56,57]. This acceleration was attributed to removal of the activation barrier for nucleation, because the substrate served as a two-dimensional nucleus for crystalline ice growth [56,57]. The crystallization rate decreased rapidly with increasing distance from the crystalline ice substrate [56,57]. This was ascribed to crystallization-induced cracking of the films that result from stresses that develop during crystallization due to density differences between amorphous and crystalline phase [56,57]. Reported values for the activation energy for the crystallization of ASW vary from 44 kJ/mole [53] to 70 kJ/mole [51,54,56]. The discrepancies in these values could be attributed to substrate effects [56,57] or differences in ASW preparation [19].

Liquids cooled below their freezing point can form an amorphous solid (glass) on experimental time scales if crystallization is avoided. A long-standing question has been whether the melt of ASW is connected to normal supercooled water or it is a distinct liquid phase [10,60]. Just above the glass transition temperature (T_g), the diffusion coefficients of supercooled liquids display either strong or fragile temperature dependencies [10,60]. Fragility is a term used to characterize the temperature dependence of relaxation processes in liquids. The viscosity of a fragile liquid displays a non-Arrhenius dependence on temperature, and a fragile liquid becomes very fluidic, relative to its glassy state, in a short temperature range above T_g [10]. In the case of a strong liquid, the variation of viscosity with temperature closely follows the Arrhenius law as the liquid is cooled toward its glass transition temperature. Despite numerous studies, there is still uncertainty about water-glass transition temperature and whether supercooled water is a strong or fragile liquid at low temperatures ($T < 160$ K) [20,23,44,52,61-63].

Transport processes in ASW below 150 K are sluggish [7,60,64,65]. This makes study of water-glass transition (if there is one below 160 K) using bulk samples difficult experimentally. Smith et al. have used nanoscale thin films of ASW to overcome the problem of observing an extremely small diffusion length on an experimental timescale [62,66,67]. They observed self-mixing in thin isotopically labeled, nanoscale ASW layers near 150 K [62]. These results were interpreted as bulk diffusion of a fragile liquid and this has also provided support for the conventional estimate of the water glass transition temperature of ~ 140 K [62,66].

In contrast, more recent studies by Mullins and coworkers have shown that the mixing observed in thin ASW films is primarily due to transport through an interconnected porous network created in the film upon crystallization [68,69]. Their findings suggest that the self-diffusivity of water between 150 and 160 K is significantly smaller than previously thought [62,66], thus indicating that water undergoes either a glass transition or a fragile-to-strong transition at temperatures above 160 K [68,69].

The supercooled water crystallizes rapidly as temperature approaches ~ 228 K (T_s) and there is a long-standing discussion in the literature whether it is a thermodynamic singularity point or not [62,64]. ASW becomes crystalline at temperatures above 160 K (T_c) [64]. This marks the borders of the temperature region (160-228 K) that is so-called "no man's land", where studies of noncrystalline phases of water seem to be impossible [64]. While T_s may be a singularity point, the ASW crystallization rate constant is governed by an Arrhenius dependence on temperature [54,56]. Therefore, the temperature range of experimental studies of ASW can be extended with an instrument capable of measurements during rapid heating before the significant fraction of ASW sample has crystallized [70]. Chonde and coworkers conducted the first direct measurement of ASW properties above 160 K by using an ultrafast scanning microcalorimetry apparatus capable of heating rates $> 10^5$ K/s [70]. They observed rapid crystallization of ASW at 205 K and argued that a glass transition exists at 140 K [70].

1.2 Trapping and Release of Guest Molecules by ASW

The interactions between volatile gas phase molecules and the ASW surface are important for determining the composition, history, and outgassing kinetics of astrophysical multicomponent ices [71-73]. For instance, the desorption of volatile gases from comets is used to determine their present molecular composition and to estimate the astrophysical conditions at the time of their formation [71-73]. Several laboratory studies have shown that ASW can trap a variety of volatile gas molecules and release them at higher temperatures [35,39,73-76].

Experimental observations of gas trapping and release by ASW began with Ghormley [39]. His observations of O₂ trapped in the amorphous ice showed that when the ice was warmed from 77 K, O₂ was not released continuously, but rather at temperatures around 95, 160, and 214 K [39]. A more sophisticated version of Ghormley's experiment has been reported by Bar-Nun and co-workers [28,40,71,73,77] who used mass spectrometry to study gas release as gas/H₂O ices (several micrometers thick ice films) were heated from 15 K. In some ices gases were released in as many as seven distinct temperature ranges [40]. Sanford and Allamandola have published a large number of results on gas/H₂O ices [13,76,78]. They have used infrared spectroscopy to observe molecules residing on the surface rather than the gas phase species desorbing from the surface [13,76,78]. Infrared spectra of ices were recorded for many temperatures and gas/H₂O ratios, and the positions, shapes, widths, and intensities of infrared absorptions were studied in detail [13,76,78]. Decreases in the intensity of IR bands of guest molecules were

used to follow the sublimation of trapped species. As in the works of Ghromey [39] and Bar-Nun et al. [28,40,71,73,77], gas release occurred in well-defined temperature regions and sometimes gas was retained up to sublimation of the ice film itself [13,76,78]. An extension of these trapping studies were done by Kouchi [27] and Hudson and Donn [75]. Kouchi [27] examined CO trapping in mixtures with water using a combination of vapor pressure studies and electron diffraction, while Hudson and Donn [75] investigated the same system in a combined TPD and IR spectroscopy study. By combining two techniques, both research groups were able to correlate the observation of gas release with changes in the solid ice [27,75]. More recent TPD studies by Ayotte et al. [35] and Collings et al. [74,79] have extended the previous work by examining the dependence of trapping and release of volatile gases by ASW films on ASW morphology and gas deposition conditions.

The important condition for trapping of deposited molecules is for guest molecules to possess enough mobility to diffuse into the porous ASW film [29,35,36,80]. Ayotte et al. suggested that an increase in ASW temperature induces slight molecular rearrangements that result in permanent pore closure and trapping of guest molecules residing in pores [35]. They showed that transport and trapping of volatile gas molecules are highly dominated by ASW porosity [35]. The concentration of trapped molecules also shows a strong dependence on the gas deposition technique (whether gas molecules deposited on top of ASW, underneath ASW or gas co-deposited during ASW formation) [35,74].

It is widely accepted that for thin ASW films (< ~100 layers thick) the release of trapped molecules takes place during the ASW-to-CI transition, as well as during the sublimation of the CI ice film [35,73-75]. The abrupt release of guest molecules during crystallization (often referred to as molecular volcano [67]) apparently occurs through connected desorption pathways in the film; these pathways can be formed from structural changes such as cracks and fractures that occur during the ASW-to-CI transition [35,81]. Cracks and fractures are believed to occur due to stresses created within the film during crystal grain growth and grain-grain impingement [36].

Some molecules are not released during the ASW-to-CI transition and stay trapped in the CI until the sublimation of the film [35,74,75]. The nature of these trapping sites is not fully resolved. Ayotte et al. have suggested that these molecules could be trapped in a simple pore, clathrate hydrate cage, or simply covered by a water overlayer [35]. However, only a few species form clathrate hydrates under low-temperature and ultrahigh vacuum (UHV) conditions [82-84]. It is also unclear what (porosity, deposition conditions, etc.) mediates the ratio of trapped species released during the phase transition to trapped species that are retained within CI.

The primary goal of the research described in this dissertation is to study trapping and release of guest molecules by amorphous ice. The interactions of $^{13}\text{CO}_2$ guest molecules with amorphous ice were examined via a combination of FTIR and TPD techniques. The experimental details will be discussed in Chapter 2.

Chapter 3 will focus on a Raman shifter developed to employ resonant laser induced desorption. Chapter 4 will be devoted to experimental results and discussion. Chapter 5 will focus on preliminary work and suggestions for future experiments.

1.3 References

1. P.V. Hobbs, *Ice Physics*, Claderon Press: Oxford, 1974.
2. F. Franks, *The properties of Aqueous Solutions at Subzero Temperatures*, in *Water: A comprehensive treatise*, F. Franks, Editor; Plenum Press: New York, 1982.
3. V. Buch and J.P. Devlin, *Introduction*, in *Water in Confining Geometries*, V. Buch and J.P. Devlin, Editors; Springer: Berlin, 2003.
4. C. Girardet and C. Toubin, *Surface Science Reports*, **44**, 163, (2001).
5. A.B. Horn, J.R. Sodeau, T.B. Roddis, and N.A. Williams, *J. Phys. Chem. A*, **102**, 6107, (1998).
6. Z.Y. Wang and S.K. Zhou, *Progress in Chemistry*, **16**, 49, (2004).
7. C.A. Angell, *Annu. Rev. Phys. Chem.*, **55**, 559, (2004).
8. P. Jenniskens and D.F. Blake, *Science*, **265**, 753, (1994).
9. R. Smoluchowski, *Science*, **201**, 809, (1978).
10. C.A. Angell, *Science*, **267**, 1924, (1995).
11. L.J. Allamandola, S.A. Sandford, A.G.G.M. Tielens, and T.M. Herbst, *Astrophys. J.*, **399**, 134, (1992).
12. K.P. Stevenson, G.A. Kimmel, Z. Dohnalek, R.S. Smith, and B.D. Kay, *Science*, **283**, 1505, (1999).
13. L.J. Allamandola, S.A. Sandford, and G.J. Valero, *Icarus*, **76**, 225, (1988).
14. S.A. Sandford and L.J. Allamandola, *J. Astrophys.*, **355**, 357, (1990).
15. E. Mayer and R. Pletzer, *Nature*, **319**, 298, (1986).
16. M.G. Sceats and S.A. Rice, *Amorphous Solid Water and Its Relationship to Liquid Water: A Random Network Model for Water*, in *Water: A comprehensive treatise*, F. Franks, Editor; Plenum Press: New York, 1982.
17. E.F. Burton and W.F. Oliver, *Proceedings Royal Society*, **A153**, 166, (1935).

18. R. Zallen, *The Physics of Amorphous Solids*, John Wiley and Sons, Inc.: New York, 1983.
19. R.S. Smith, Z. Dohnalek, G.A. Kimmel, G. Teeter, P. Ayotte, J.L. Daschbach, and B.D. Kay, *Molecular Beam Studies of Nanoscale Films of Amorphous Solid Water*, in *Water in Confining Geometries*, V. Buch and J.P. Devlin, Editors; Springer: Berlin, 2003.
20. P. Jenniskens, S.F. Banham, D.F. Blake, and M.R.S. McCoustra, *J. Chem. Phys.*, **107**, 1232, (1997).
21. O. Mishima, L.D. Calvert, and E. Whalley, *Nature*, **310**, 393, (1984).
22. O. Mishima, L.D. Calvert, and E. Whalley, *Nature*, **314**, 76, (1985).
23. G.P. Johari, A. Hallbrucker, and E. Mayer, *Nature*, **330**, 552, (1987).
24. N. Sartori, J. Bednar, and J. Dubochet, *Journal of Microscopy-Oxford*, **182**, 163, (1996).
25. A.H. Narten, C.G. Venkatesh, and S.A. Rice, *J. Chem. Phys.*, **64**, 1106, (1976).
26. Y.P. Handa, O. Mishima, and E. Whalley, *J. Chem. Phys.*, **84**, 2766, (1986).
27. A. Kouchi, *Journal of Crystal Growth*, **99**, 1220, (1990).
28. D. Laufer, E. Kochavi, and A. Bar-Nun, *Phys. Rev. B*, **36**, 9219, (1987).
29. V. Sadtchenko, K. Knutsen, C.F. Giese, and W.R. Gentry, *J. Phys. Chem. B*, **104**, 4894, (2000).
30. R.A. Baragiola, *Microporous Amorphous Water Ice Thin Films: Properties and Their Astronomical Implications*, in *Water in Confining Geometries*, V. Buch and J.P. Devlin, Editors; Springer: Berlin, 2003.
31. C.A. Tulk, C.J. Benmore, J. Urquidi, D.D. Klug, J. Neuefeind, B. Tomberli, and P.A. Egelstaff, *Science*, **297**, 1320, (2002).
32. B.S. Berland, D.E. Brown, M.A. Tolbert, and S.M. George, *Geophys. Res. Lett.*, **22**, 3493, (1995).
33. J. Hessinger, B.E. White, and R.O. Pohl, *Planetary and Space Science*, **44**, 937, (1996).

34. J. Kruger and W.J. Ambs, *Journal of the Optical Society of America*, **49**, 1195, (1959).
35. P. Ayotte, R.S. Smith, K.P. Stevenson, Z. Dohnalek, G.A. Kimmel, and B.D. Kay, *J. Geophys. Res. Plan.*, **106**, 33387, (2001).
36. G.A. Kimmel, K.P. Stevenson, Z. Dohnalek, R.S. Smith, and B.D. Kay, *J. Chem. Phys.*, **114**, 5284, (2001).
37. R. Pletzer and E. Meyer, *J. Chem. Phys.*, **90**, 5207, (1989).
38. B. Schmitt, J. Ocampo, and J. Klinger, *Journal De Physique*, **48**, 519, (1987).
39. J.A. Ghormley, *J. Chem. Phys.*, **46**, 1321, (1967).
40. A. Bar-Nun, J. Dror, E. Kochavi, and D. Laufer, *Physical Review B*, **35**, 2427, (1987).
41. J.P. Devlin, *J. Phys. Chem.*, **96**, 6185, (1992).
42. A. Hallbrucker, E. Mayer, and G.P. Johari, *J. Phys. Chem.*, **93**, 7751, (1989).
43. C. Manca, C. Martin, and P. Roubin, *Chem. Phys.*, **300**, 53, (2004).
44. J.A. Ghormley, *J. Chem. Phys.*, **48**, 503, (1968).
45. O. Andersson and A. Inaba, *Phys. Chem. Chem. Phys.*, **7**, 1441, (2005).
46. A. Kouchi, J.M. Greenberg, T. Yamamoto, and T. Mukai, *Astrophys. J.*, **388**, L73, (1992).
47. O. Andersson and H. Suga, *Solid State Communications*, **91**, 985, (1994).
48. C.A. Angell, *Annu. Rev. Phys. Chem.*, **34**, 593, (1983).
49. C. Manca, C. Martin, and P. Roubin, *Chem. Phys.*, **300**, 53, (2004).
50. A. Kouchi, T. Yamamoto, T. Kozasa, T. Kuroda, and J.M. Greenberg, *Astronomy and Astrophysics*, **290**, 1009, (1994).
51. W. Hage, A. Hallbrucker, E. Mayer, and G.P. Johari, *The Journal of Chemical Physics*, **100**, 2743, (1994).

52. M. Fisher and J.P. Devlin, *J. Phys. Chem.*, **99**, 11584, (1995).
53. N.J. Sack and R.A. Baragiola, *Physical Review B*, **48**, (1993).
54. R.S. Smith, C. Huang, E.K.L. Wong, and B.D. Kay, *Surf. Sci.*, **367**, L13, (1996).
55. R.S. Smith and B.D. Kay, *Surf. Rev. Lett.*, **4**, 781, (1997).
56. Z. Dohnalek, G.A. Kimmel, R.L. Ciolli, K.P. Stevenson, R.S. Smith, and B.D. Kay, *J. Chem. Phys.*, **112**, 5932, (2000).
57. Z. Dohnalek, L.C. Ryan, A.K. Greg, K.P. Stevenson, R.S. Smith, and D.K. Bruce, *J. Chem. Phys.*, **110**, 5489, (1999).
58. W. Hage, A. Hallbrucker, E. Mayer, and G.P. Johari, *The Journal of Chemical Physics*, **103**, 545, (1995).
59. P. Jenniskens and D.F. Blake, *The Astrophysical Journal*, **473**, 1104, (1996).
60. C.A. Angell, *Chem. Rev.*, **102**, 2627, (2002).
61. G.P. Johari, *J. Phys. Chem. B*, **102**, 4711, (1998).
62. R.S. Smith and B.D. Kay, *Nature*, **398**, 788, (1999).
63. Y.Z. Yue and C.A. Angell, *Nature*, **427**, 717, (2004).
64. O. Mishima and H.E. Stanley, *Nature*, **396**, 329, (1998).
65. D.E. Brown and S.M. George, *J. Phys. Chem.*, **100**, 15460, (1996).
66. R.S. Smith, Z. Dohnalek, G.A. Kimmel, K.P. Stevenson, and B.D. Kay, *Chem. Phys.*, **258**, 291, (2000).
67. R.S. Smith, C. Huang, E.K.L. Wong, and B.D. Kay, *Phys. Rev. Lett.*, **79**, 909, (1997).
68. S.M. McClure, E.T. Barlow, M.C. Akin, D.J. Safarik, T.M. Truskett, and C.B. Mullins, *J. Phys. Chem. B*, **110**, 17987, (2006).
69. S.M. McClure, D.J. Safarik, T.M. Truskett, and C.B. Mullins, *J. Phys. Chem. B*, **110**, 11033, (2006).

70. M. Chonde, M. Brindza, and V. Sadtschenko, *J. Chem. Phys.*, **125**, 094501, (2006).
71. A. Bar-Nun and I. Kleinfeld, *Icarus*, **80**, 243, (1989).
72. J.A. Nuth, H.G.M. Hill, and G. Kletetschka, *Nature*, **406**, 275, (2000).
73. A. Bar-Nun, G. Herman, D. Laufer, and M.L. Rappaport, *Icarus*, **63**, 317, (1985).
74. M.P. Collings, M.A. Anderson, R. Chen, J.W. Dever, S. Viti, D.A. Williams, and M.R.S. McCoustra, *Mon Not R Astron Soc*, **354**, 1133, (2004).
75. R.L. Hudson and B. Donn, *Icarus*, **94**, 326, (1991).
76. S.A. Sandford and L.J. Allamandola, *Icarus*, **76**, 201, (1988).
77. A. Bar-Nun, J. Dror, E. Kochavi, D. Laufer, D. Kovetz, and T. Owen, *Origins of Life and Evolution of the Biosphere*, **16**, 220, (1986).
78. S.A. Sandford and L.J. Allamandola, *Astrophys. J.*, **355**, 357, (1990).
79. M.P. Collings, J.W. Dever, H.J. Fraser, and M.R.S. McCoustra, *Astrophysics and Space Science*, **285**, 633, (2003).
80. G.A. Kimmel, K.P. Stevenson, Z. Dohnalek, R.S. Smith, and B.D. Kay, *Journal of Chemical Physics*, **114**, 5284, (2001).
81. R.S. Smith, C. Huang, and B.D. Kay, *J. Phys. Chem. B*, **101**, 6123, (1997).
82. H.H. Richardson, P.J. Wooldridge, and J.P. Devlin, *J. Chem. Phys.*, **83**, 4387, (1985).
83. D. Blake, L. Allamandola, S. Sandford, D. Hudgins, and F. Freund, *Science*, **254**, 548, (1991).
84. G. Notesco and A. Bar-Nun, *Icarus*, **148**, 456, (2000).

Chapter 2: Experimental Details

The experiments described in this dissertation were performed in an ultrahigh vacuum (UHV) chamber designed to employ several surface diagnostic techniques. A thorough description of this setup can be found elsewhere [1-3] and only a brief description will be outlined here. However, during the course of these experiments the experimental setup was modified to incorporate additional techniques and these modifications will be discussed below in details.

2.1 UHV System

The ultrahigh vacuum system has three levels as shown in Figure 2.1 where the surface manipulator is attached to the upper level. The upper level is used mainly for FTIR spectroscopy and will be referred to as the FTIR chamber. The two bottom levels of UHV system have numerous ports that allow the chamber to house several experimental techniques simultaneously. In current configuration the level B is equipped with instrumentation to perform laser induced desorption experiments. The entire system is pumped by a turbomolecular pump (Leybold Turbovac 600, 560 l/s) attached to the level B. The gate valve separates the FTIR chamber from the bottom levels, and this permits the FTIR chamber to be opened without pressurizing bottom levels. The pressure in the chamber is typically $\sim 2 \times 10^{-10}$ Torr after baking at 120°C for 3 – 4 days. After venting the chamber to atmosphere, it must be baked in order to remove the residual water adsorbed on the

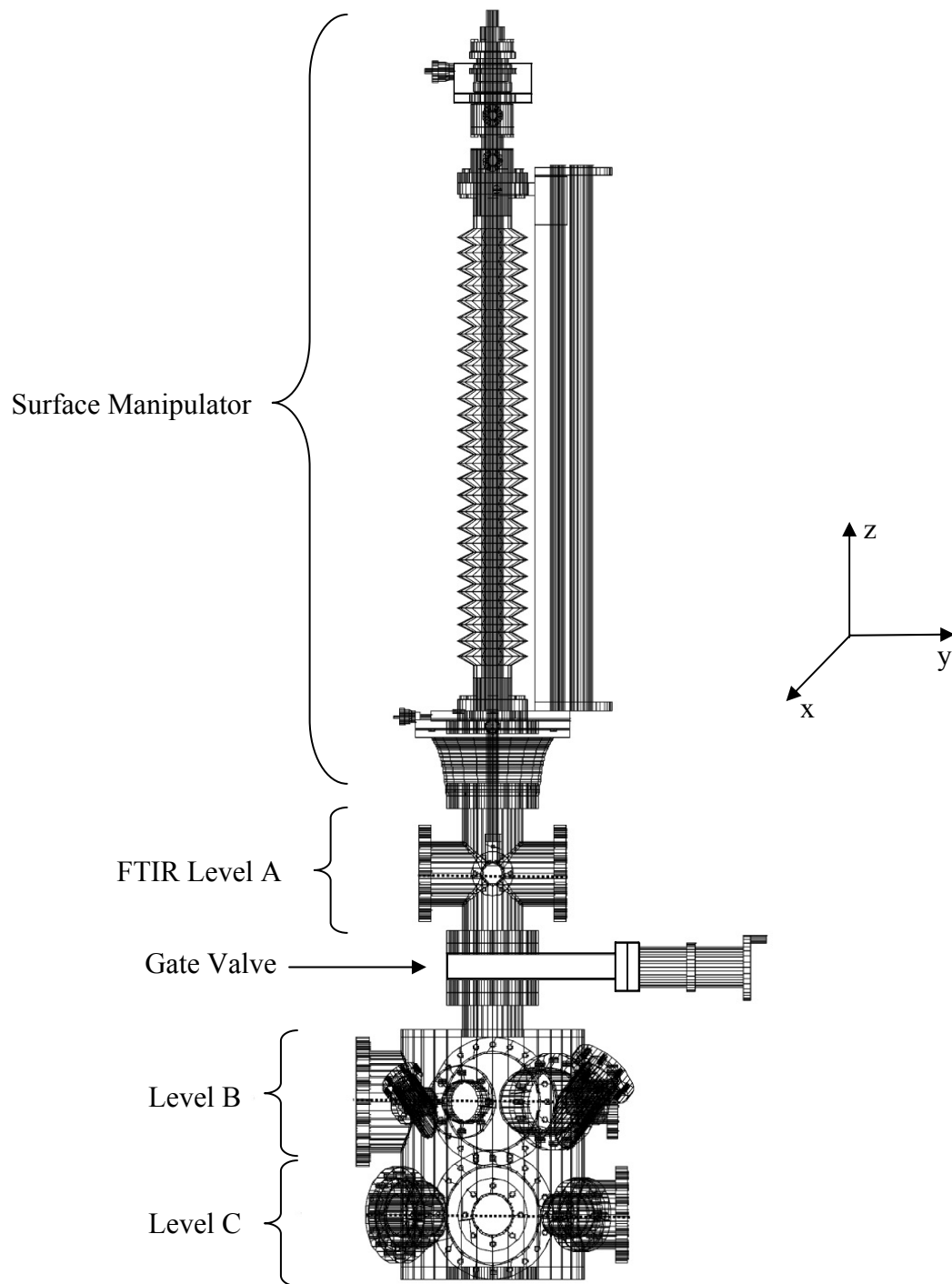


Figure 2.1. Drawing of the UHV chamber. The UHV system has three levels with the surface manipulator attached to the upper level. The entire system is pumped by a turbomolecular pump connected to the level B.

walls of the system. The resistive heating tapes, controlled individually by Variac potentiometers, are used to heat the chamber. Insulated K-type thermocouples (Omega) are attached at various places of the chamber to insure adequate, even heating.

2.2 FTIR Chamber

The top level of the UHV system was designed to perform FTIR experiments. The schematic of the FTIR level is shown in Figure 2.2. A separate level was necessary in order to minimize the IR beam path length and increase signal to noise ratio. The surface manipulator is attached to the top port of the FTIR chamber. The FTIR level is separated from the levels below by a UHV gate valve (MDC GV-4000M, bakeout temperature up to 250°C in open position).

Calcium fluoride (CaF_2) windows are attached to two smaller ports that allow the IR radiation to pass through the FTIR chamber. In experiments involving combined FTIR and TPD studies a residual gas analyzer (SRS RGA 300) was attached to the FTIR chamber (Figure 2.2). The RGA has a specifically designed cone with a small aperture (~8 mm). The small aperture reduces RGA signal due to molecules desorbing from surfaces other than the sample surface. Two precision leak valves (MDC ULV-075) connected using a "tee" to the FTIR chamber port and used to introduce sample gases into the UHV system.

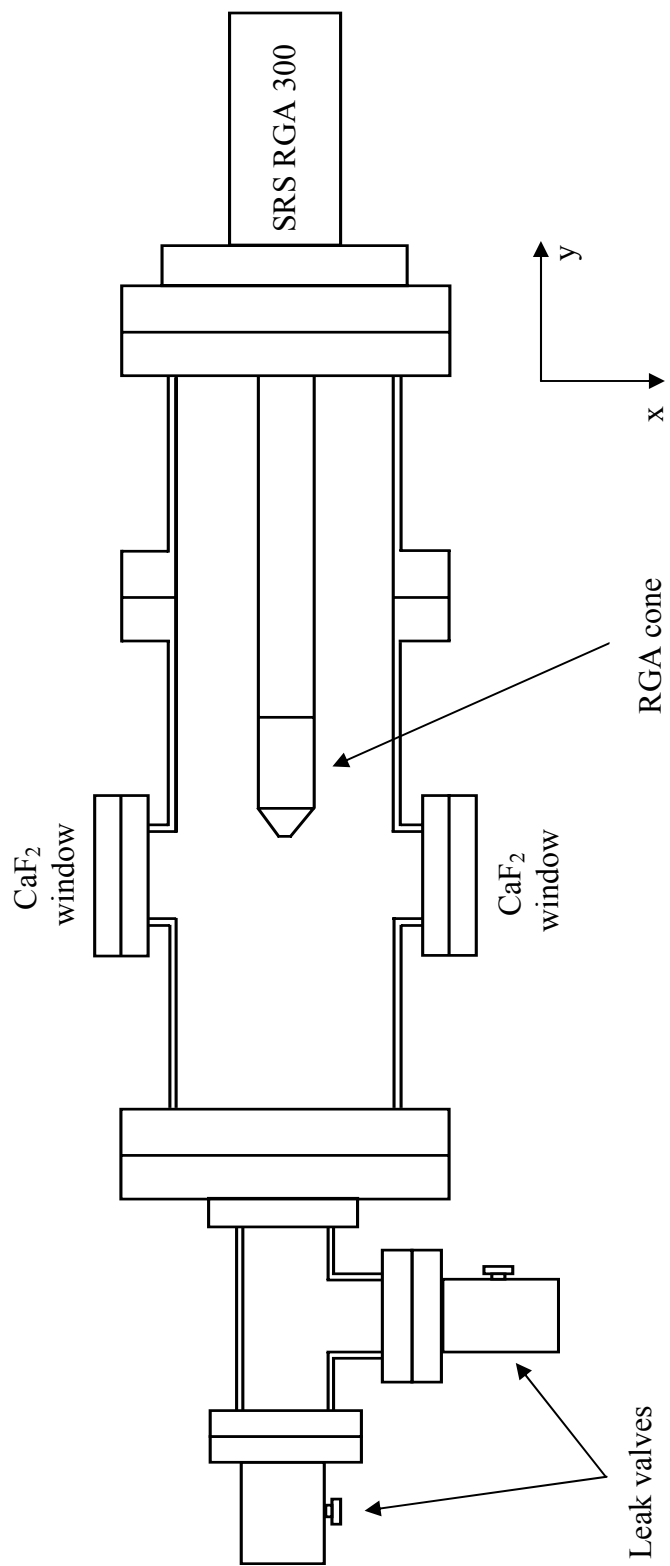


Figure 2.2. A schematic of FTIR chamber

2.3 FTIR Setup

The FTIR spectrometer (Nicolet Protégé 460) and steering optics (Nicolet) are located at the same level as the FTIR chamber. The IR beam is directed into the chamber to record the IR spectrum of the sample located in the center of the FTIR chamber (Figure 2.3). The spectrometer bench contains the IR source (a glowbar [4]) and the Michelson interferometer [5,6]. The IR source has effective area $\sim 5 \times 5$ mm and situated at the focal point of a mirror with the focal length 3.43". This mirror collimates the IR beam and steers it to the interferometer, as shown in Figure 2.3. The IR interference beam is directed to the external port of the FTIR bench. Upon exiting the FTIR bench the beam is turned 90° by a flat mirror to the first focusing mirror (6" focal length). The focusing mirror turns the beam 90° and focuses it into the chamber through the CaF_2 window. As a result of this configuration, the focused beam is approximately 9 mm in diameter when it passes through the sample. The sample can be positioned with its surface either normal to the IR beam or at an angle.

After traveling through the IR transparent sample, the beam exits the UHV chamber through another CaF_2 window, and then it is focused onto the liquid nitrogen cooled indium antimonide (InSb) detector. The InSb detector ($\sim 2 \times 2$ mm) converts the IR intensity into an electrical current. The InSb detector requires liquid nitrogen cooling, as it has to operate at cryogenic temperatures (typically 80 K) to reduce the noise from thermally induced transitions. The liquid nitrogen cooled

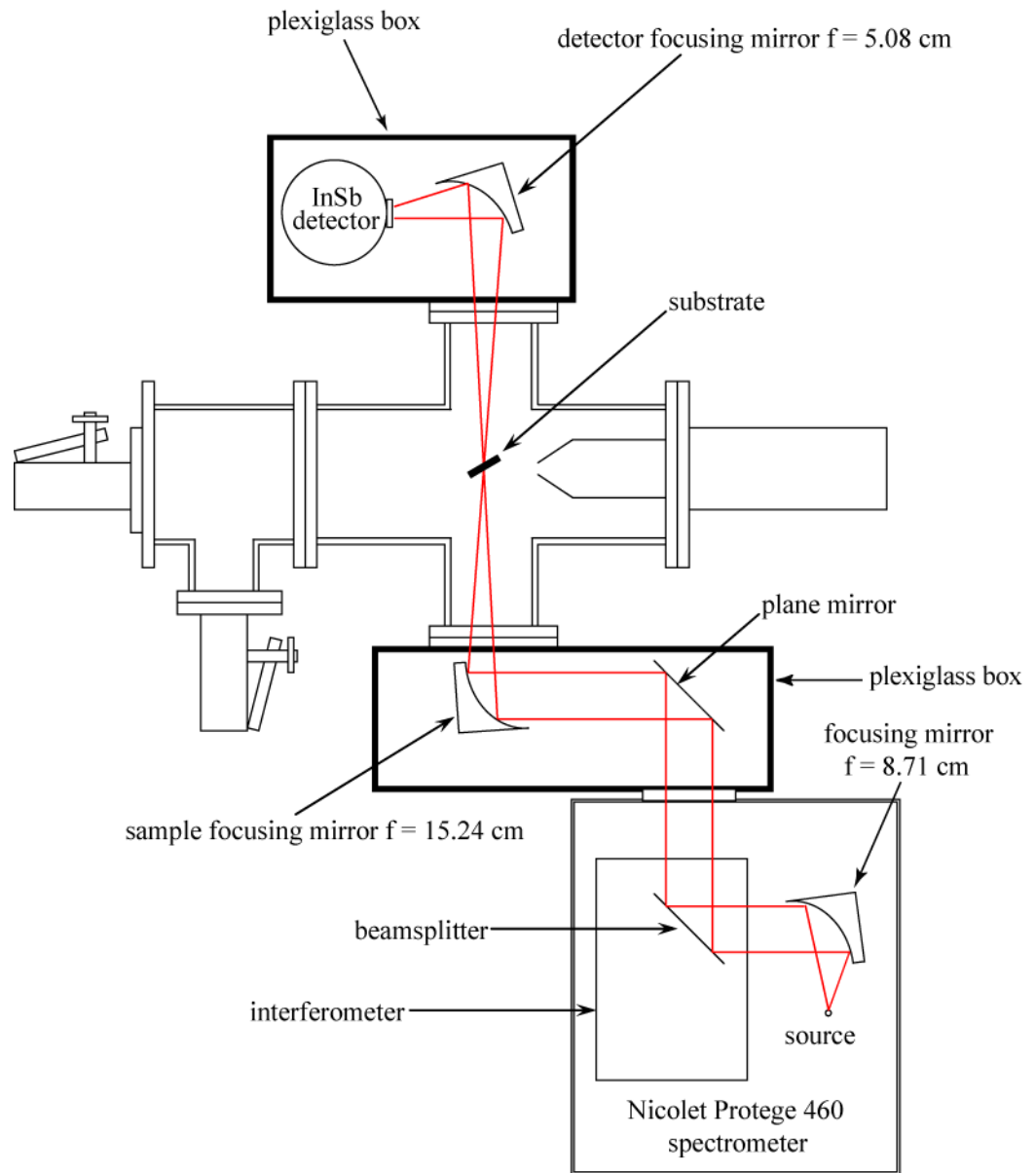


Figure 2.3. Schematic drawing of the optical setup for FTIR spectroscopy. The entire beam path is purged to remove atmospheric water and carbon dioxide.

InSb detectors are the most efficient in the mid-infrared wavelength range with a specific detectivity, D^* , of $\sim 2.4 \times 10^{10}$ cm \cdot Hz²/W [5].

During experiments in which polarized light is used, a wire-grid polarizer (Molelectron, 93-98% purity) is placed in the IR beam path between the CaF₂ window and the detector focusing mirror. The wire-grid polarizer consists of a regular array of fine parallel aluminum wires, placed on a barium fluoride surface in a plane perpendicular to the incident beam. The polarizer only transmits the electric field component perpendicular to the wires, the electric field component parallel to the wires is absorbed or reflected [7].

CO₂ and H₂O have relatively strong absorptions in the mid-IR region (4000 - 2000 cm⁻¹). Fluctuation noise occurs when the air composition between the interferometer and detector changes. It is necessary to purge all the optics and the FTIR spectrometer in order to achieve high signal-to-noise ratio. To that end, all optics outside the FTIR bench was placed in Plexiglas boxes. The FTIR bench and Plexiglas boxes are purged by a dry air gas provided by a purge gas generator (Whatman FT-IR 75-62). The purge gas generator filters out H₂O and CO₂ from an in-house compressed air supply line.

2.4 The Surface Manipulator

The sample's position and temperature are controlled through a custom made manipulator (Figure 2.4). The original manipulator was made by the Kurt J. Lesker from Vacuum Generator parts [3]. The original surface holder rod of the

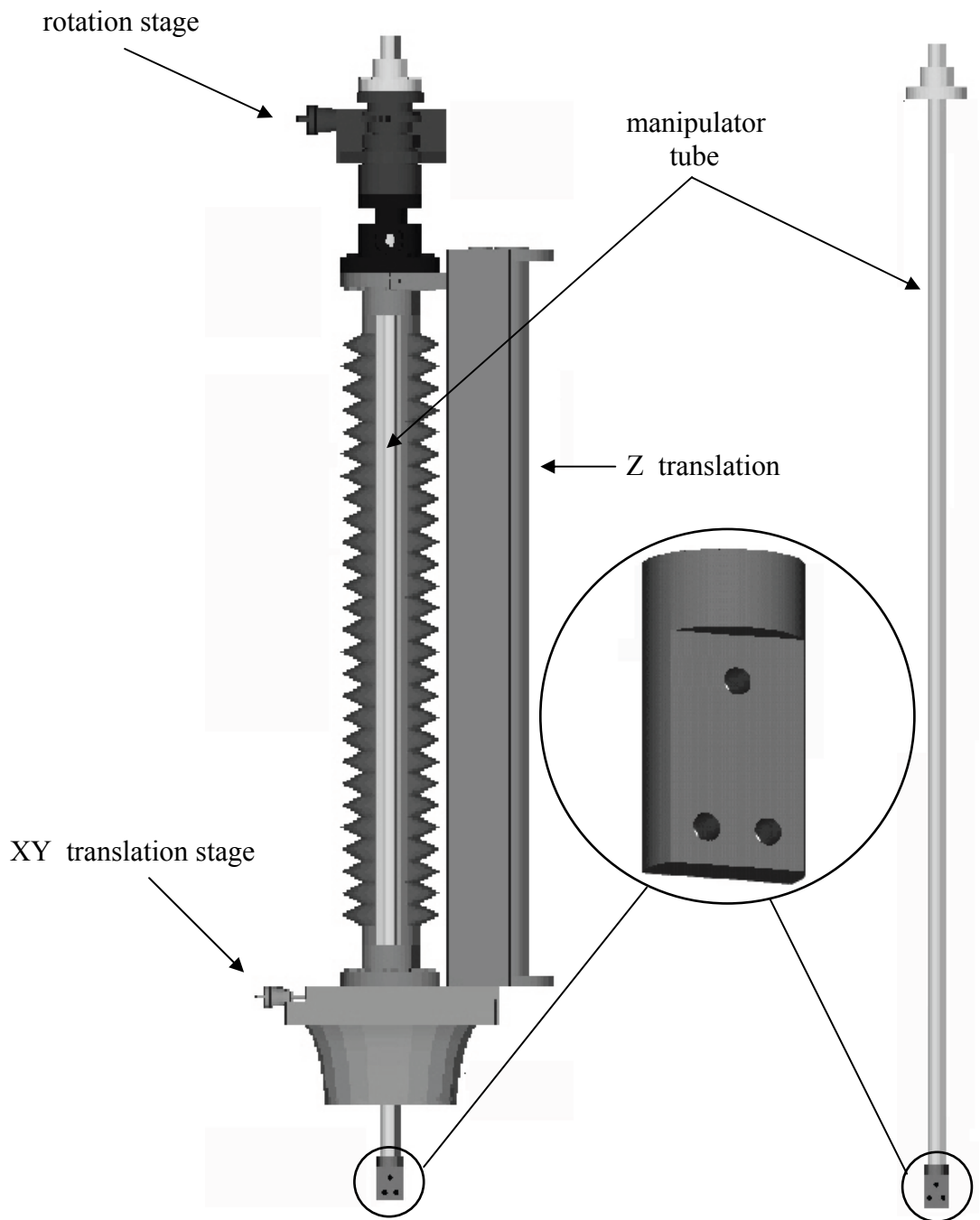


Figure 2.4. Schematic of the custom-made surface manipulator. The stainless steel tube is used as a liquid nitrogen reservoir with a copper piece silver-brazed to the end.

manipulator could not provide efficient cooling of the sample and was redesigned by McAllister Technical Services [3]. The redesigned rod is a stainless steel tube that is open to the atmosphere on one end while the other end has a copper block silver-brazed to it (Figure 2.4). In this design the liquid nitrogen is poured into the tube and has direct contact with the copper piece attached to it. The reservoir length shortens by about 3 - 4 mm along the z-direction upon cooling with liquid nitrogen. The surface manipulator allows 600 mm translation along z-axis, permitting movement of the sample between the different levels of the UHV system. It also features 25 mm translation along the x and y axes and permits 360° sample rotation.

2.5 Substrate Preparation

MgO(100) single crystals ($\sim 1 \times 10 \times 10$ mm) were used as substrates in all studies presented in this dissertation. The MgO(100) single crystal is among the simplest and best known insulator surfaces. Magnesium oxide has a face-centered cubic (fcc) lattice structure with the lattice constant 2.98 Å [8]. The (100), (010), and (001) surfaces are most thermally stable and are identical due to the fcc symmetry. The MgO single crystal can be easily cleaved along the (100) plane [9]. MgO(100) is transparent (> 90%) in the infrared region of interest (4000 – 2000 cm^{-1}) and it can be easily prepared and cleaned in-situ [9,10].

The MgO(100) substrate was prepared by cleaving a MgO single crystal (MTI Corporation, 10 × 10 × 30 mm fine ground) inside a Plexiglas box purged by dry

nitrogen gas. The cleavage is done twice to expose two fresh MgO(100) crystal surfaces. Defect sites introduced during cleavage in a dry atmosphere are mostly oxygen vacancies, and step defects [9]. After cleavage, a K-type thermocouple (Omega) is cemented to the edge of the crystal face (Aremco 835M, 30 min in the dry nitrogen atmosphere). The substrate is then placed in a copper sample holder and inserted into the UHV chamber. The chamber is closed and pumped down to UHV conditions. The UHV system is baked for several days, as described above. In order to minimize oxygen vacancies the MgO(100) surface has to be annealed to 600 K for 1 hour in 10^{-7} Torr of oxygen (research grade) [3,10]. Annealing also removes any carbon contamination from the surface [10]. This procedure of substrate preparation has been shown to produce a clean, defect free Mg(100) substrate [10,11] and it was applied to all substrates used for the experiments reported in this dissertation.

2.6 Sample Preparation

Two precision leak valves (MDC ULV-075) are used to introduce sample gases into the UHV system. The leak valves have different stainless steel dosing lines that enables dosing of two different gases simultaneously. The non-water gas line is built from 1/2" stainless steel tubing, 1/2" swagelock fittings, and bakeable needle valves and it is pumped using cryogenic sorption pumps. The non-water line is baked thoroughly above 100°C to remove any water contamination. The purity of the gas is checked using the RGA mass spectrometer during backfilling of the

chamber with this gas. The other dosing line is used for dosing water and oxygen only. It is made of 1/4" stainless steel tubing and pumped with a mechanical pump.

Before performing experiments the MgO substrate was heated to 400 K to desorb any contaminants then cooled to 90 K for dosing. H₂O (distilled and purified by osmosis) was degassed by several freeze-pump-thaw cycles and used to produce vapor deposited ice films. This deposition process was performed typically at ~90 K. CO₂ (Gilmore, 99.99% purity) and ¹³CO₂ (Icon Isotopes, 99%) were used without further purification. These gases were introduced into the chamber through the non-water leak valve.

2.7 Sample Holder

The sample holder, which is attached to the copper block at the end of the cooling stainless steel tube (Figure 2.4), must satisfy several requirements to allow TPD and FTIR experiments with ASW and ASW/CO₂ mixtures. The surface must be able to be cooled below 120 K to form ASW and heated above 500 K to clean it. Moreover, in order to physisorb CO₂ on the MgO(100) surface or ASW film the substrate should have a temperature less than 95 K. The sample holder must not restrict the IR radiation for FTIR transmission experiments. It is very important to have an even cooling of the sample to avoid large temperature gradients across the surface. The sample holder must allow positioning of a sample surface close (within ~1 mm) to the mass spectrometer aperture to exclude the detection of desorbing species not originating from the sample surface. Several versions of a

sample holder were designed in order to meet these requirements. The early versions of a sample holder have been detailed previously in [1,2]. The only most recent design of a sample holder (used for the experiments reported in this dissertation) is described below and is shown in Figure 2.5.

Two main copper parts of the sample holder (labeled A and B in Figure 2.5), separated by a ceramic spacer (USC Machine Shop), are attached to the liquid nitrogen cooled copper block at the end of the surface manipulator rod. This is accomplished by using three screws that are electrically insulated from the copper parts and the rod by ceramic hat washers (McAllister Technical Services, screw size 4-40). A sapphire disc (Esco Products G110040) is inserted between the sample holder and the copper block. This disk is used for electrical insulation and as a thermal switch. The thermal conductivity of sapphire is high at low temperatures ($\sim 10 \text{ W}\cdot\text{cm}^{-1}\cdot\text{K}^{-1}$ at 80 K) and low at high temperatures ($\sim 0.03 \text{ W}\cdot\text{cm}^{-1}\cdot\text{K}^{-1}$ at 400 K) [12]. This arrangement suppresses the heat transfer from the sample holder to the liquid nitrogen reservoir during substrate heating. Thus, the liquid nitrogen reservoir remains cold while the sample temperature is increased, which allows the surface to be quickly heated and quickly re-cooled after heating.

The substrate is placed on a thin copper plate (ESPI, 3N8 purity, 0.25 mm thick) ($\sim 0.3 \times 10 \times 14 \text{ mm}$) and is attached to it by folding two opposite edges of the plate over the crystal (Figure 2.5). The plate has a protruding arm that is attached to one of the copper parts of the sample holder using a screw (Figure 2.5). A homemade

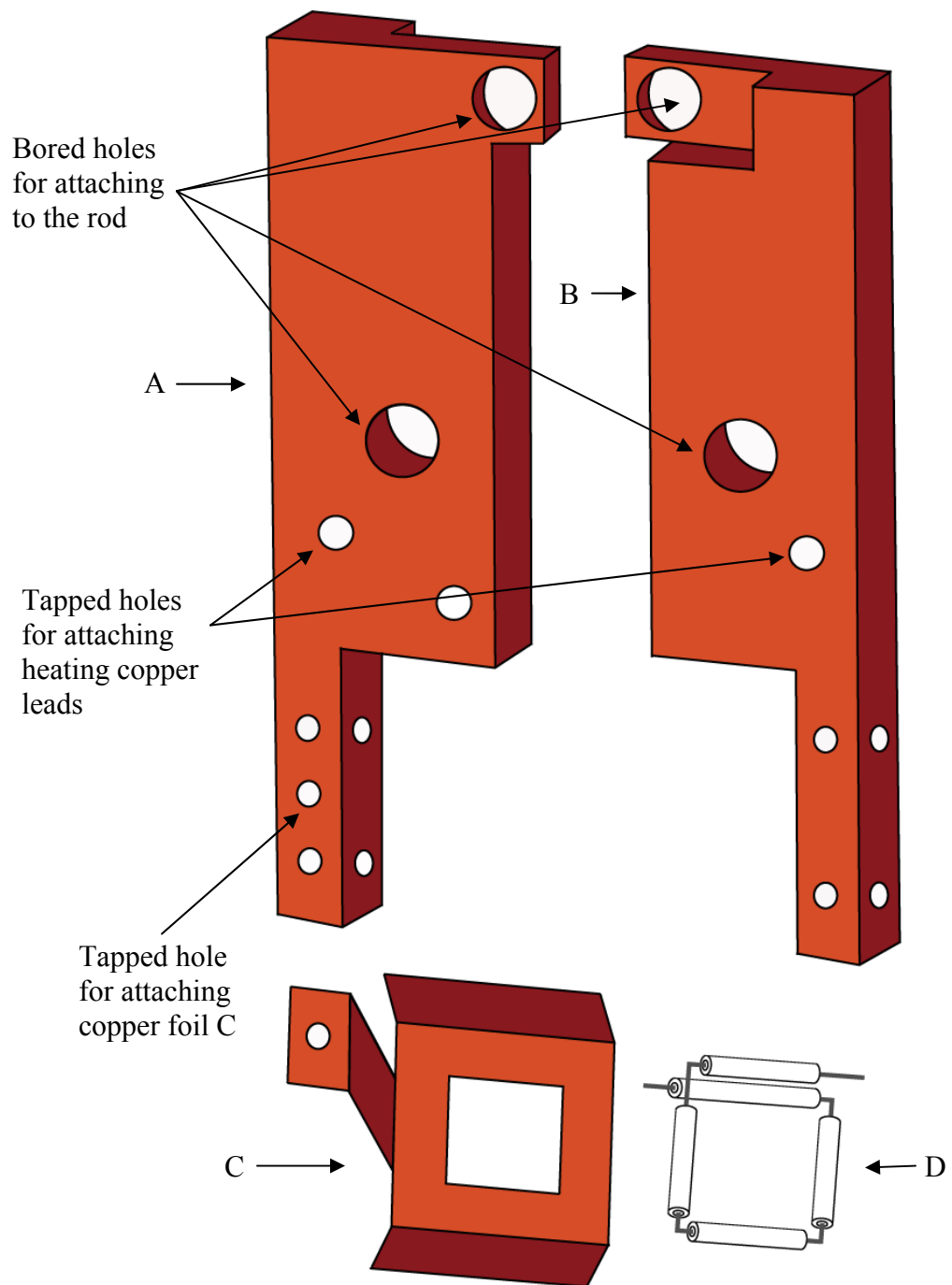


Figure 2.5. Drawing of a sample holder (most recent design). The sample holder consists of two main copper parts labeled A and B. The surface resides on a piece C made from copper foil that is attached to A using a screw. The homemade resistive heating element D is glued to the back of the copper foil piece C.

resistive heater is glued (Aremco 835M) to the other side of the thin copper plate. The homemade resistive heater is a wire coil made from tantalum wire (ESPI, 3N8 purity, 0.38 mm). The wire is insulated by a ceramic, single-hole, round insulator tube (Omega ORX-020132). Each end of the wire is threaded through one of the bored holes in the sample holder copper part and is compressed against the copper by a stainless steel screw. A substrate temperature of ~ 100 K is achieved with this surface holder. However, by bubbling helium gas (high pure grade) through the liquid nitrogen reservoir, a colder substrate temperature of ~ 90 K is achieved [13].

Two 18-gauge copper leads are attached to the different isolated copper parts of the sample holder (Figure 2.5). This allows passing an electrical current through the resistive heater. The heating rate of the sample can be adjusted by changing the current through the heater. The maximum current (~ 18 A) is limited by the copper electrical leads and feedthroughs (Insulator Seal, 1000 V, 15 A) on the manipulator. Using an electrical current of ~ 10 A, the surface could be heated from 90 K to 400 K, at a rate ~ 2 K/s.

2.8 Laser Induced Desorption Setup

Originally, the level B (Figure 2.1) of the UHV system was designed as a surface analysis level [1,3]. Later it was modified to house the equipment for the laser induced desorption (LID) studies. The experimental setup employed in the (LID) measurements is shown schematically in Figure 2.6. The time of flight

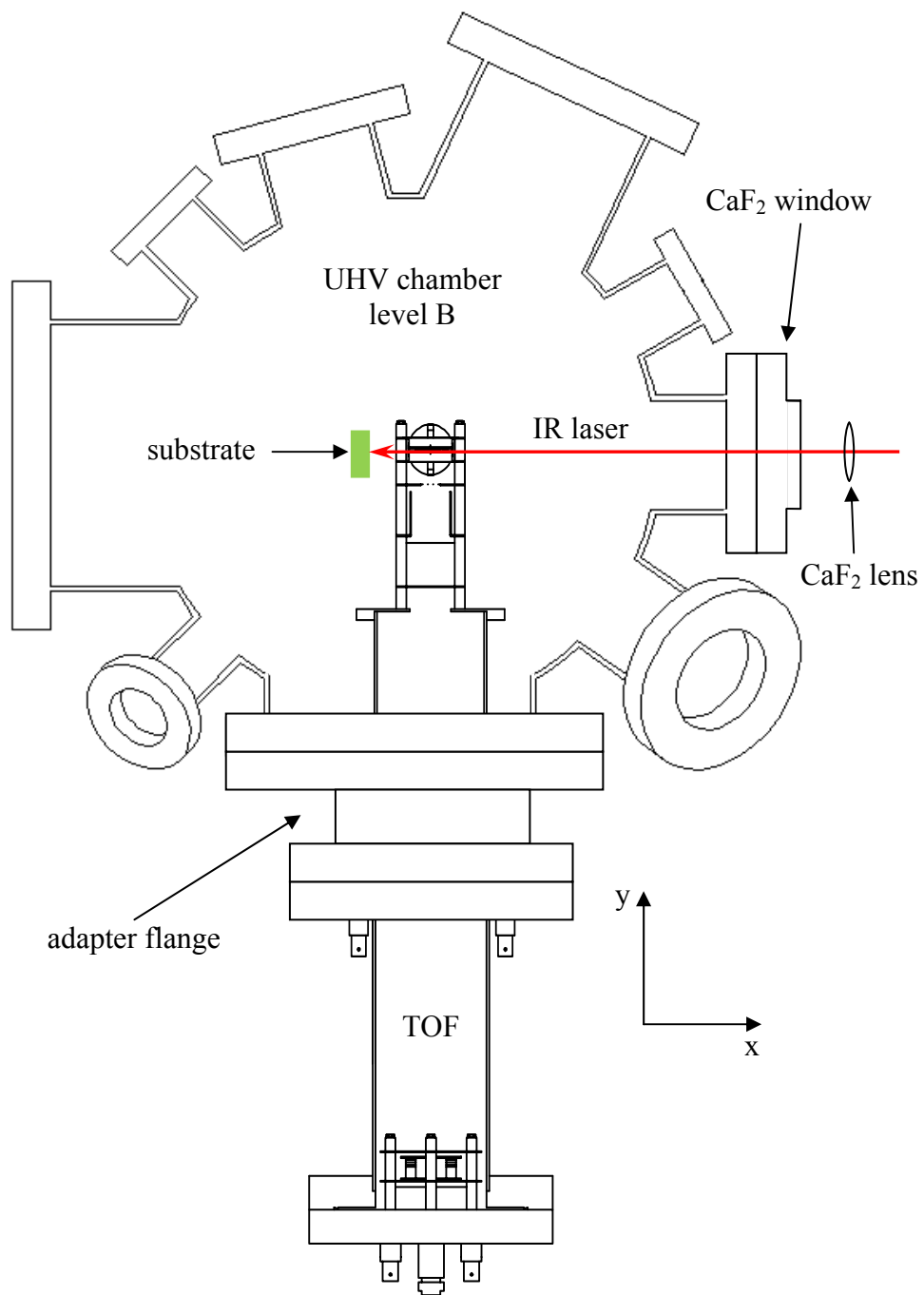


Figure 2.6. Schematic of level B of the UHV chamber. The TOF mass spectrometer is attached to the UHV chamber through an adapter flange.

(TOF) mass spectrometer (described in the next section) is used to detect molecules desorbing from the surface. It is attached to the chamber through a custom made reducing nipple (USC Machine Shop). The nipple also offsets the TOF spectrometer along the x axis by ~ 2.5 cm from the center of the chamber to allow for sufficient clearance to the surface holder.

The $2.93 \mu\text{m}$ IR radiation used for LID experiments is generated by Raman shifting $1.064 \mu\text{m}$ light from a pulsed Nd:YAG (10 Hz, 9 ns) laser using a 1.1 m Raman cell filled with 900 PSI of deuterium gas. This laser system is described in the next chapter. The laser beam enters the chamber through a CaF_2 window and is focused onto the substrate by a CaF_2 lens (ISP Optics CF-PX-25-500, 50 cm focal lens) at a normal incidence angle (Figure 2.6). The laser beam passes between the repeller and extractor plates of the TOF mass spectrometer before it reaches the substrate. The substrate is positioned perpendicularly to the repeller and extractor plates. The distance from the substrate to the center of the ionization region of the TOF mass spectrometer is ~ 3 cm. This geometrical arrangement ensures that most of the desorbed molecules reach the ionization region of the TOF mass spectrometer. An ionization gauge attached to one of the ports on the level B is used to monitor the pressure inside the UHV chamber. This ion gauge was turned off during TOF measurements, because it affects the operation of the TOF mass spectrometer by charging the repeller plate.

2.9 Time of Flight Mass Spectrometer

In the following the principle of operation of a TOF mass spectrometer is described briefly [14]. The linear TOF mass spectrometer (Jordan TOF Products) (Figure 2.7) consists of an electron gun (EGUN) (Jordan TOF Products C-950), set of electrodes (ion source, accelerating and steering electrodes), a field free time-of-flight (drift) region (~42 cm) (Jordan TOF Products C-677) and a dual microchannel plate (MCP) ion detector (Jordan TOF Products C-701, 18mm diameter, chevron style). The ions are formed in the middle between the repeller and extractor plates (ionization region) by electron bombardment of neutral molecules drifting into this region (Figure 2.7). An electric field accelerates the positive ions into a field-free drift region, keeping them at a constant kinetic energy of $q \cdot V$, where q is the ion charge and V is the applied voltage. Since all ions have the same kinetic energy, lighter ions have a higher velocity than heavier ions and reach the detector at the end of the drift region sooner. In other words, a TOF mass spectrometer uses differences in transit time through a drift region to separate ions of different masses.

The TOF mass spectrometer operates in a pulsed mode. The ions are produced, extracted and accelerated in pulses (at a rate up to 200 kHz). At the beginning of a cycle the repeller plate is at 1800 V and the extraction grid at 1550 V. Following a trigger pulse, the voltage on the plates is equalized at 1800 V. Both plates remain at this voltage for a time determined by the pulse duration control (normally 4 μ s). During this time, electrons are injected between the plates and ionization takes

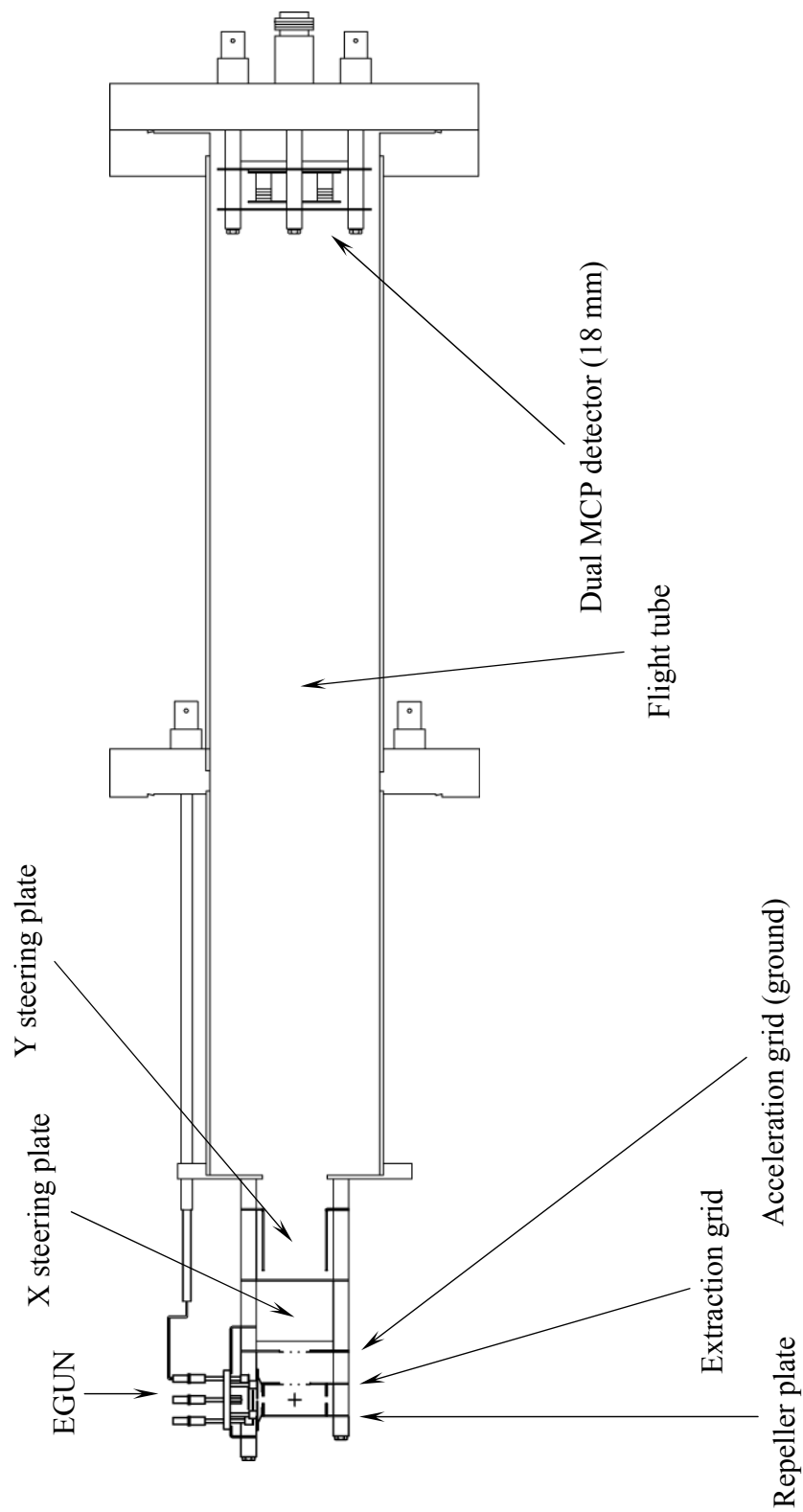


Figure 2.7. Schematic of a linear time-of-flight (TOF) mass spectrometer.

place. Then the voltage on the extraction grid returns to 1550 V so that ions can be extracted into the acceleration region (between extractor and acceleration grids). They are then accelerated through the grounded grid (acceleration grid) into the drift region. The drift time for water is approximately 4 μ s. The extraction grid will remain at 1550 V until the next triggering pulse. The voltages on the grids are optimized to provide the best mass resolution in the H₂O mass region (*i.e.* around 18 amu).

The output of the MCP detector is connected through a short cable (Jordan TOF Products, N type to BNC, 5 cm) to a fast amplifier (SRS DC-300 MHz). The amplification ratio can be set to $\times 5$, $\times 25$, or $\times 125$. The fast amplifier is connected to an analog-to-digital converter computer board (Gage CS8500, 8 bit, 512 kSamples). The temporal resolution of the board is 2 ns (500 MSamples/s). The board records the signal from the MCP detector for a certain time (typically 200 μ s) at every laser shot (10 Hz). During this time the TOF mass spectrometer completes 40 cycles. Thus the temporal profile of the TOF signal is also obtained. The data collected by the computer board is processed by a LabView program, which subtracts background and integrates peak areas.

2.10 References

1. S.A. Hawkins, *Fourier transform infrared spectroscopy and temperature programmed desorption of water thin films on the MgO (100) surface*, Ph. D. Thesis, Department of Chemistry, University of Southern California, Los Angeles, 2004.
2. G. Kumi, *Fourier transform infrared studies of guest-host interactions in ice*, Ph. D. Thesis, Department of Chemistry, University of Southern California, Los Angeles, 2007.
3. M.M. Suchan, *Molecules-surface interactions in HCl/MgO and Water/MgO Systems*, Ph. D. Thesis, Department of Chemistry, University of Southern California, Los Angeles, 2001.
4. D.A. Skoog and J.L. Leary, *Principles of Instrumental Analysis*, Harcourt Brace College Publishers: Fort Worth, 1992.
5. P. Griffiths and J.A. De Haseth, *Fourier Transform Infrared Spectrometry*, John Wiley and Sons, Inc.: New York, 1986.
6. B.C. Smith, *Fourier Transform Infrared Spectroscopy*, CRC Press: Boca Raton, 1996.
7. X.J. Yu and H.S. Kwok, *J. Appl. Phys.*, **93**, 4407, (2003).
8. K.H. Rieder, *Surf. Sci.*, **118**, 57, (1982).
9. V.E. Henrich and P.A. Cox, *The Surface Science of Metal Oxides*, Cambridge University Press: Cambridge, 1994.
10. L.K. Hodgson, *Photodissociation, molecule-surface collision-induced dissociation and direct adsorbate photolysis of nitroso molecules*, Ph. D. Thesis, Department of Chemistry, University of Southern California, Los Angeles, 1993.
11. L. Hodgson, G. Ziegler, H. Ferkel, H. Reisler, and C. Wittig, *Canadian Journal of Chemistry-Revue Canadienne De Chimie*, **72**, 737, (1994).
12. Sheikh, II and P.D. Townsend, *Journal of Physics E-Scientific Instruments*, **6**, 1170, (1973).
13. J. Yates, J. T., *Experimental Innovations in Surface Science*, AIP Press Springer-Verlag: New York, 1998.
14. W.C. Wiley and I.H. McLaren, *Rev. Sci. Instrum.*, **26**, 1150, (1955).

Chapter 3: Infrared Laser Source Based on Gaseous Deuterium

Raman Shifter

3.1 Overview

Among the various techniques used to generate tunable laser radiation in the UV–FIR spectral region, the most common are dye lasers, optical parametric oscillators (OPO's), difference frequency mixing, and stimulated Raman scattering (SRS). Although dye lasers were commonly utilized due to their tunability, because these laser systems are typically bulky, expensive to operate, and require frequent change of dyes, their use has recently waned. As the use of dye systems decreased, they were replaced by OPO's. The OPO's rely on the nonlinear response of a crystal for conversion of a high energy pump wave into two low-energy waves to produce a widely tunable output by using sum or difference frequency mixing techniques. The OPO's are still expensive and require a high degree of expertise and sophistication. Another option, difference frequency mixing, uses two lasers and a nonlinear crystal to get radiation with a frequency that is the difference of the two input laser frequencies. Usually LiNbO_3 and AgGaS_2 nonlinear optical crystals are used in difference frequency mixing devices. This technique is limited by a low damage threshold for AgGaS_2 , which prevents pulsed operation. Moreover, this technique is complicated by the requirement that the two single-mode lasers have to be phase-matched.

SRS is a very efficient way to generate high-power laser radiation at multiple wavelengths in a spectral region ranging from the vacuum ultraviolet (VUV) to the

far infrared (FIR) [1-4]. SRS-based laser systems are compact and easy to use. They have an advantage over the previously discussed systems because they combine a relatively inexpensive, simple setup with a stable, high-energy output laser beam. On the other hand, SRS-based laser systems have restricted wavelengths tunability. Nevertheless, high-power tunable laser sources based on this technique have been used in various scientific and commercial applications, including remote sensing in the atmosphere for ozone [5], aerosols [6] and methane [7], and in biomedical applications [8].

The SRS laser operates by shifting the frequency of an incoming pump laser beam either up or down by an amount equal to the vibrational frequency of the active medium, and is therefore often referred to as a Raman shifter (RS). Hydrogen, deuterium and methane gases are the most frequently used media for gaseous RS, and have vibrational frequencies of 4155 cm^{-1} , 2987 cm^{-1} , and 2917 cm^{-1} respectively. A schematic of the elementary Raman process is shown in Figure 3.1. The system initially consists of gas molecules in the ground vibrational state and a photon with frequency ω_1 . When the photon is inelastically scattered by the gas molecule, the final state of the system consists of a molecule in the first vibrationally excited state $\nu=1$, and the photon of frequency ω_2 , called Stokes wave. If the system is in an excited vibrational state $\nu=1$ to begin with and the final state of the system is a molecule in the ground vibrational state then the scattered photon is called anti-Stokes wave and it has frequency ω_2 larger than the incident photon frequency ω_1 . Many of these elementary processes occur

coherently (stimulated Raman scattering), so that the resulting radiation is a wave with frequency ω_2 . As the intensity of this inelastically scattered wave increases, more photons of ω_2 frequency are emitted, *i.e.* there is amplification. The

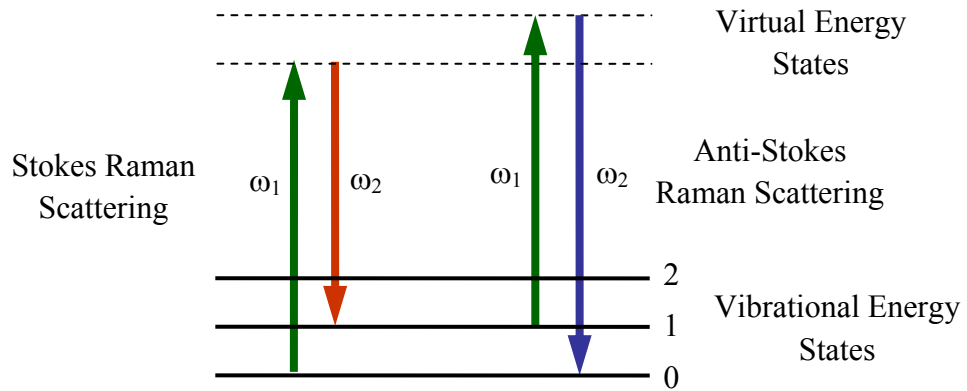


Figure 3.1. Energy diagram for Stokes and Anti-Stokes Raman processes.

stimulated Raman scattering is strongly dependent on incoming laser intensity. Therefore, the incoming beam is focused in the medium, where the Raman conversion occurs. The intensities of the Raman bands are highly dependent on the number of molecules occupying the different vibrational states. If the Raman medium is in thermal equilibrium, the relative numbers of molecules in states of different energy are determined by the Boltzmann distribution. Thus at room temperature the ground vibrational state has significantly more molecules than the excited vibrational states. Therefore, the Stokes radiation is more intense than the anti-Stokes radiation.

The focused incoming pump radiation can generate several subsequent Stokes and anti-Stokes waves. In this process the first scattered wave ω_2 acts as a pump wave which produces another shifted wave, called second Stokes (anti-Stokes) wave. This wave in turn can produce a third Stokes (anti-Stokes) wave. Thus, the frequency of n^{th} Stokes (S_n) radiation is

$$\omega_{S_n} = \omega_P - n\omega_g \quad (3.1)$$

and the frequency of n^{th} anti-Stokes (AS_n) radiation is

$$\omega_{AS_n} = \omega_P + n\omega_g, \quad (3.2)$$

where ω_P is the pump laser frequency and ω_g is the vibrational frequency of the gas molecule.

The stimulated emission process corresponds to an exponential gain of the Stokes radiation as it travels through the gaseous medium. In the simplest case, under plane-wave steady-state conditions and under the assumption that the depletion of the pump beam is neglected, the Stokes radiation intensity $I_S(z)$, as a function of distance z along the Raman cell is given by [9,10]:

$$I_S(z) = I_S(0) \cdot e^{\alpha_R \cdot z}, \quad (3.3)$$

where $I_S(z)$ is the amplified Stokes light intensity, $I_S(0)$ is the initial Stokes light intensity (provided by spontaneous Raman scattering), and α_R is the plane-wave Raman gain coefficient:

$$\alpha_R \sim \frac{nI_P}{\lambda_S(\lambda_S + \lambda_P)\Gamma_R}. \quad (3.4)$$

Here I_p is the pump beam intensity, n is the population density, λ_S is the Stokes wavelength, λ_p is the pump laser wavelength, and Γ_R is the FWHM Raman linewidth. Equations 3.3 and 3.4 are valid at the beginning of the nonlinear amplification process of the Stokes radiation and are useful for threshold energy dependence evaluations. The Stokes generation threshold increases as its wavelength increases. This makes it more difficult to obtain second and third Stokes waves. In principle one can obtain mid-infrared radiation by pumping the shifter with laser operating in visible region. However, due to the $1/(\lambda_S)^2$ dependence of Raman gain on λ_S (Equation 3.4), in practice the single-pass RS has only been used to generate the 2nd Stokes wave. The dependence on n makes it favorable for the Raman gain to use a denser medium. The Γ -dependence suggests using the media with the narrowest Raman linewidth while the bandwidth of a Raman shifted light (for a pump laser with negligible bandwidth) is determined by pressure broadening at high pressures (> 20 atm) of the gaseous Raman medium and by Doppler broadening at lower pressures (< 20 atm) [11]. The Raman linewidth is roughly proportional to the pressure for high pressures [12]. Therefore according to Equation 3.4 the Raman gain becomes mostly independent of pressure for high pressures.

Equations 3.3 and 3.4 provide only a qualitative description. There is no exact solution for the Stokes (anti-Stokes) light generation in a single-pass RS. Many factors such as the laser beam geometry, laser beam intensity, gaseous Raman medium and its pressure etc. affect significantly the RS operation. In practice, it is

impossible to predict theoretically the optimum conditions for these parameters and they have to be optimized experimentally.

3.2 Experimental Setup

The experimental arrangement of the Raman Shifter is outlined in Figure 3.2. It consists of a Q-switched Nd:YAG laser (1064 nm), a high pressure deuterium gas cell, and focusing and steering optics. The Nd:YAG pulsed laser (Continuum NY81C) has a 9 ns pulse duration, 10 Hz repetition rate and a pulse energy ≤ 800 mJ/pulse. The circularly polarized Nd:YAG laser beam is directed into the deuterium cell by two dielectric mirrors (Thorlabs NB1-J14, $\lambda = 1047 - 1064$ nm, 45° AOI) M1 and M2 and is converted to linear polarization by a quarter-wave plate (CVI QWPO-1064-05-4, 1064 nm, $\lambda/4$). The laser beam is focused into the gas cell by an input lens L1 (CVI PLCX-25.4-515.1-C-1064, AR 1064 nm) having 1 m focal length. The Raman cell output is collimated by the CaF₂ lens L2 (Thorlabs LA5956, $f=75$ cm). The various laser wavelengths generated by the SRS process (Table 3.1) are separated by a 60° CaF₂ prism. The incidence angle of the radiation is 56° to minimize reflection losses on the CaF₂ prism. The CaF₂ lens L3 (Thorlabs LA5835, $f=100$ cm) focuses the collimated output beam to create better spatial separation between the different spectral components after dispersing in the prism. The second Stokes radiation is detected by a calibrated Pyroelectric energy

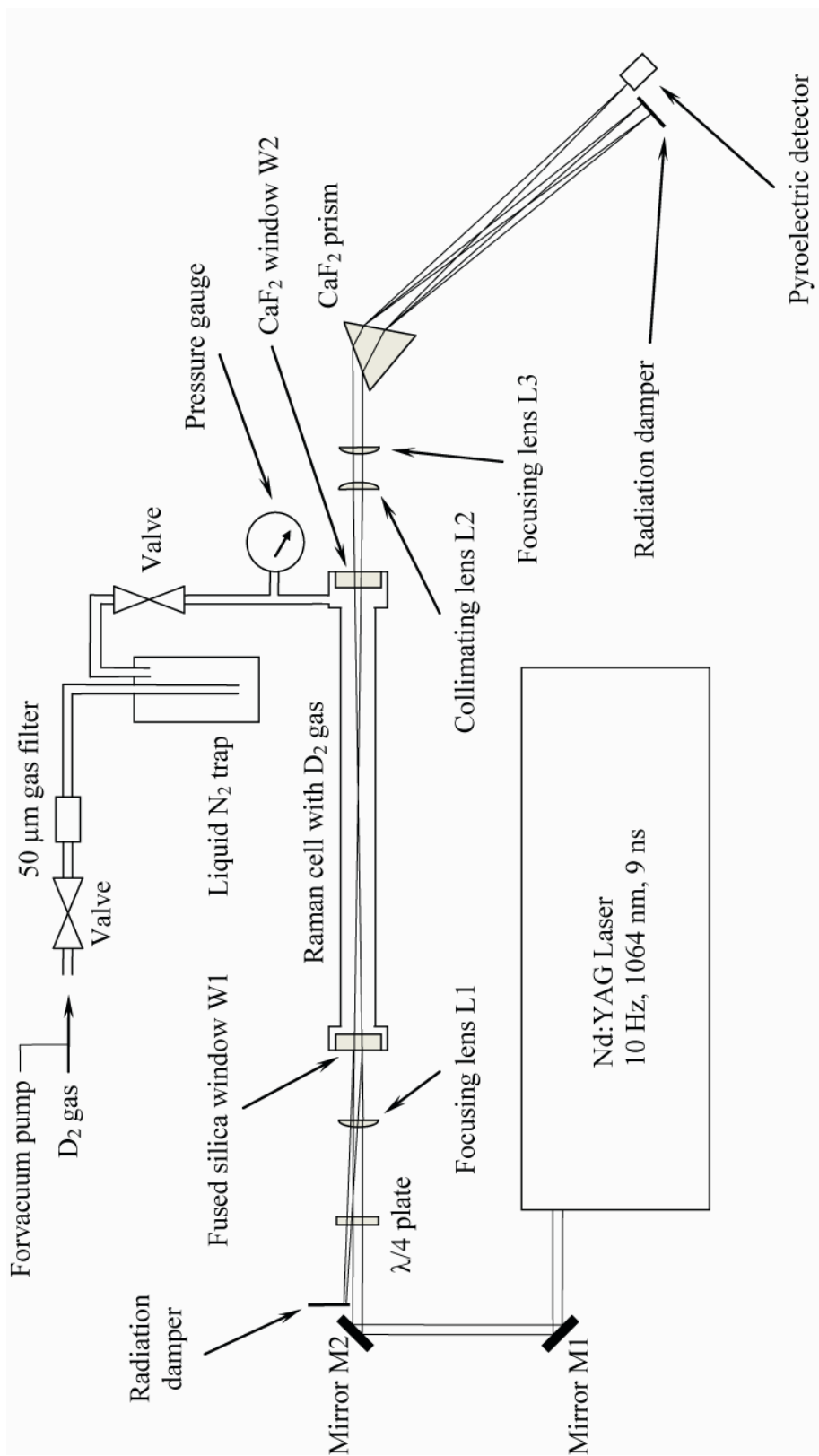


Figure 3.2. A schematic of the Raman shifter.

meter (OPHIR 3A-P-CAL-SH, 3Watts) or a fast liquid nitrogen cooled MCT detector (Cincinnati Electronics SDD-7854-S1-05M, 16 MHz) connected to a fast oscilloscope.

The Raman shifter gaseous deuterium is held in a custom-made 1.1 m long stainless steel tube (typically 900 PSI of D₂). The gas tube has two windows, designed to withstand an internal pressure more than 1200 PSI against the normal atmospheric pressure outside. The minimum thickness t_w (mm) of a window that can withstand the required pressure differential is calculated by the formula:

$$t_w = \sqrt{\frac{1.1PD^2}{MR}}, \quad (3.5)$$

where D is the unsupported diameter of the window (~21 mm), P is the pressure differential (PSI), and MR is the modulus of rupture (PSI) of the window material. Table 3.2 lists optical window materials and corresponding properties including transmission range, index of refraction, and modulus of rupture. The input fused silica window (CVI PW-1550-UV, $D = 38$ mm) has a thickness of 13 mm and it is slightly tilted to prevent the reflected laser light from going back into the laser. The output CaF₂ window (ISP Optics CF-W-38-13, $D = 38$ mm) has the same thickness as the input window and transmits ~90% of radiation at wavelengths up to 1400 cm⁻¹.

The exit flange is equipped with a gas connector. Gas filling, pumping out and pressure control are performed through this connector. The deuterium gas (99.999%) was purchased from Advanced Specialty Gases. It takes ~200 L of

	ν , cm^{-1}	λ , nm
V_{D_2}	2987	3348
S_2	3424.5	2920
S_1	6411.5	1560
Fundamental	9398.5	1064
AS_1	12385.5	807
AS_2	15372.5	650

Table 3.1. Wavelengths and frequencies for Raman output.

Window material	Transmission range	Index of refraction	Modulus of rupture
BK7	330 - 2100 nm	1.5164 @ 588 nm	2400 PSI
Fused silica	185 - 2500 nm	1.4858 @ 308 nm	7000 PSI
Sapphire	180 - 4500 nm	1.755 @ 1000 nm	65000 PSI
CaF_2	170 - 7800 nm	1.399 @ 5000 nm	5300 PSI
MgF_2	120 - 7000 nm	1.376 @ 700 nm	7200 PSI

Table 3.2. Properties of common optical window materials [13].

deuterium (STP) to fill the gas cell to 900 PSI. It is crucial to maintain high purity conditions to ensure highly efficient SRS processes. Therefore, the gas cell and liquid nitrogen trap are baked at 120°C for 2 – 3 days before every gas filling. Additionally, the gas is passed through the particulate filter (Swagelok SS-4F-05, 0.5 μm pore size) and a liquid nitrogen trap to remove any possible contamination.

3.3 Optimum Conditions for the Second Stokes Generation

Several factors have to be considered when optimizing the second Stokes generation. For instance, the dependence of the second Stokes light intensity on the focusing geometry, pump energy, and the deuterium gas pressure has to be taken into account. Several groups have reported on the importance of the focusing geometry for SRS processes in methane (which has similar Raman gain coefficient to deuterium) [2,14]. It is been shown experimentally that the optimal focusing distance for the pump beam into the Raman cell is 1.0 - 1.2 m [2,14]. In practice it is more convenient to use a lens with 1-m focal length because it requires a shorter Raman cell (the Raman cell has to be long enough to prevent damage to the input and exit windows by the focused pump laser beam). Lenses with shorter focusing length (50 - 75 cm) resulted in more than 50% second stokes intensity decrease in our experiments consistent with previous studies of SRS in methane [2,14].

The high energy density caused by the focused-geometry of the laser beam often lead to laser induced breakdown in the gaseous medium, which was shown to be a limiting factor in the conversion efficiency and the quality of the Stokes

radiation [15,16]. The gas breakdown can be achieved by multiphoton ionization, which is a nonlinear process that coexists with SRS [15]. Alternatively, seed electrons from impurities with subsequent laser induced avalanche ionization contribute to the formation of plasma [15]. Two main sources of impurities in the RS cell are its surface and the gas dosing line. The incoming gas is passed through a particulate filter (0.5 μm pore size) and liquid nitrogen trap to minimize impurities introduced with the deuterium gas. The presence of several monolayers of adsorbate on the RS surface can result in an impurity partial pressure of several Torr after long time outgassing. Early experiments showed that these impurities can cause complete degradation of the second Stokes generation because of gas breakdown. Baking ($\sim 120^\circ\text{C}$) of the Raman cell leads to faster outgassing from its surface and thus the RS can be effectively cleaned by pumping out impurities during its baking. The results of baking have to be checked by monitoring the pressure rise in the RS cell when it is pumped out and disconnected from the pump. The pressure in the cell should not increase by more than several mTorr in one hour.

The dependence of the second Stokes energy on deuterium gas pressure is shown in Figure 3.3 for 150 mJ/pulse pump energy. The threshold pressure for the second Stokes generation is ~ 400 PSI. . Increasing the pressure of the deuterium gas leads to a greater photon conversion efficiency. The quantum conversion efficiency of the SRS process, Y_{Sn} is given by,

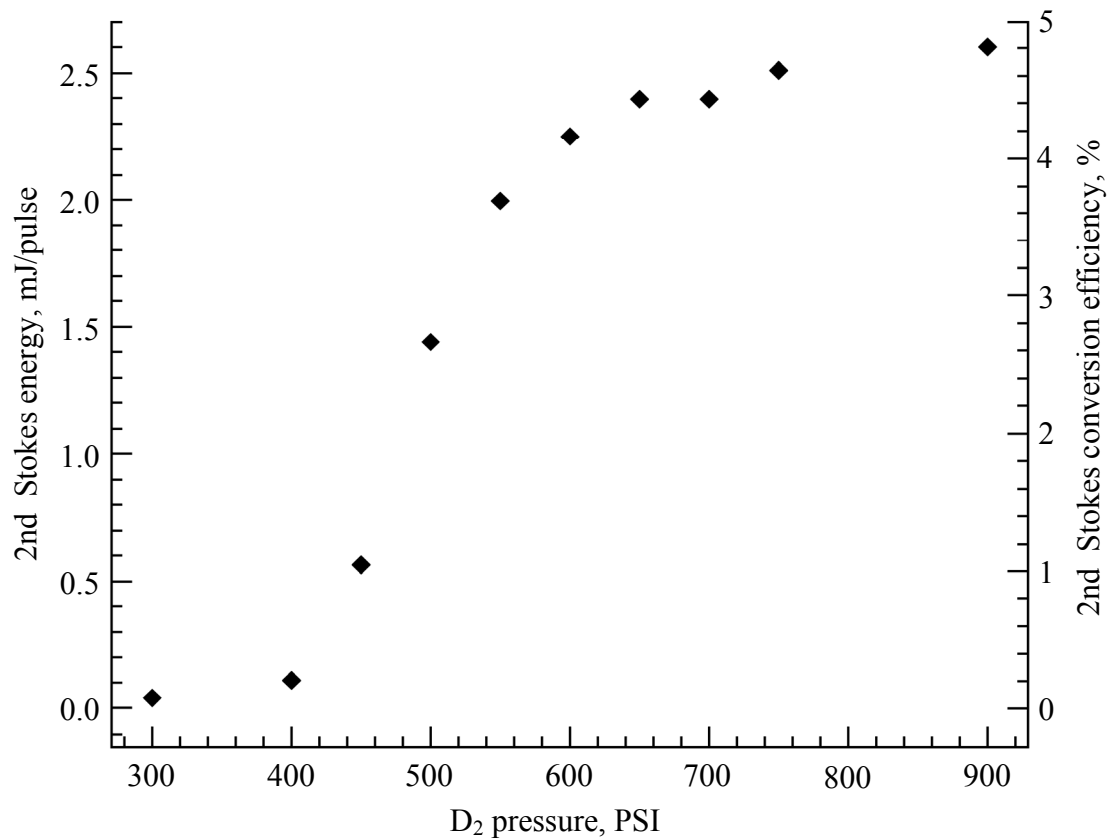


Figure 3.3. Dependence of the 2nd Stokes pulse energy and 2nd Stokes conversion efficiency on D₂ pressure at 150 mJ/pulse pump pulse energy.

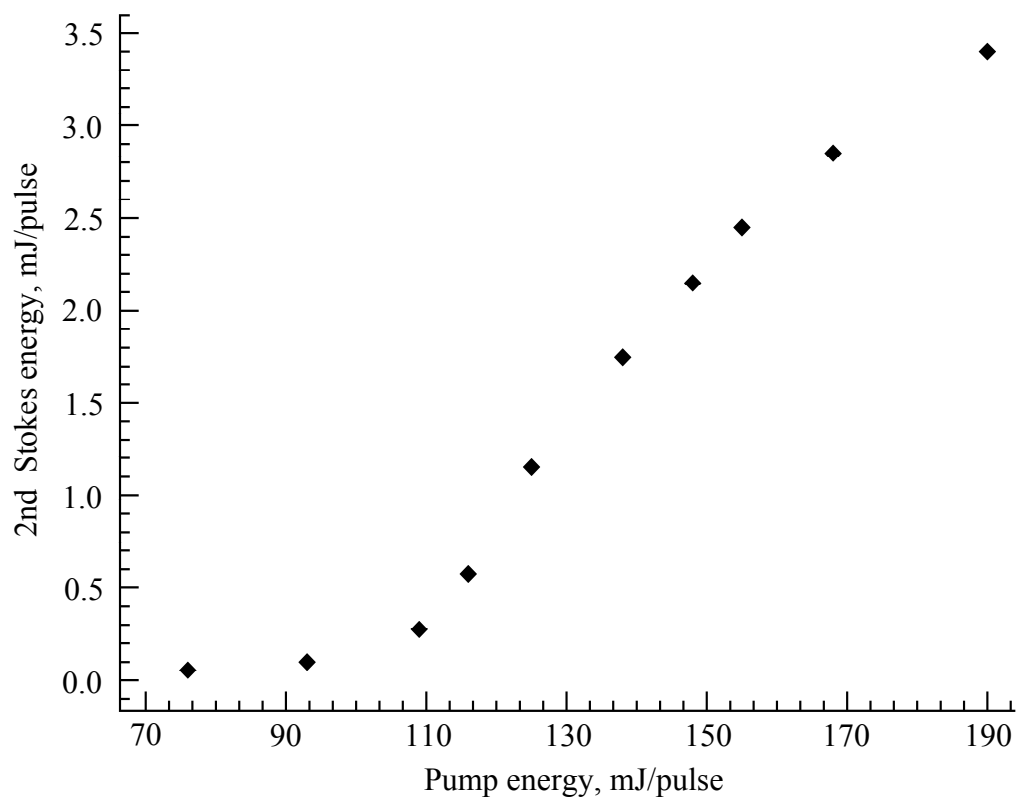


Figure 3.4. Dependence of the 2nd Stokes energy on pump pulse energy at D_2 pressure of 750 PSI.

$$Y_{Sn} = \frac{E_{Sn}}{E_p} \frac{\lambda_{Sn}}{\lambda_p}, \quad (3.6)$$

where E_{Sn} and E_p are the pulse energies of the Stokes radiation and of the pump beams, respectively, and λ_{Sn} and λ_p are the corresponding wavelengths. The second Stokes conversion efficiency for D_2 pressures > 700 PSI approaches $\sim 5\%$ and becomes almost independent of gas pressure. Due to a small gas leak in the system ($\sim 1 - 2$ PSI/month) it was preferable to use higher pressures of D_2 (~ 900 PSI) to ensure long operation of RS before having to add D_2 .

Figure 3.4 shows the dependence of the pulse energy of the second Stokes radiation on the pump pulse energy for 750 PSI D_2 pressure. The threshold energy for the second Stokes generation is ~ 110 mJ/pulse. The conversion efficiency is roughly 5% for pump pulse energies from 120 to 190 mJ/pulse. It was observed that for pump laser energies > 200 mJ/pulse the second Stokes generation becomes unstable and the second Stokes energy sharply decreases. This could be prevented by cooling the middle of the cell with dry ice. However, the temperature gradients formed during the cooling cause deformation of the stainless steel tube which in turn affects the optical alignment of the system. Second Stokes energy up to ~ 7 mJ/pulse was observed for a pump laser pulse of 400 mJ/pulse when the middle of the Raman cell was cooled with dry ice. Such configuration was difficult to use because it required frequent optical realignment and increased the risk of the pump laser damaging the cell windows. We find that up to 3.5 mJ/pulse of the Second

stokes radiation can be generated with an input energy of 190 mJ/pulse for long periods of time without cooling the gas cell.

The second Stokes pulse energies given above are averaged over time (20 – 30 s). A fast liquid-nitrogen cooled MCT detector (Cincinnati Electronics SDD-7854-S1-05M, BW 16 MHz) was used to study the second Stokes pulse-to-pulse energy variations. The second Stokes beam was unfocused and attenuated by several intensity reducing filters (the detector is very sensitive). The detector was calibrated by averaging readings over several hundred laser shots and then comparing this average with that measured by a slow Pyroelectric energy meter (OPHIR 3A-P-CAL-SH, 3Watts). Figure 3.5 shows the distribution of second Stokes pulse energies for ~250 consecutive laser shots at three different pump energies. It can be seen that the pulse-to-pulse spread of the second Stokes energy is significant (roughly $\pm 50\%$) for pump pulse energies greater than 130 mJ/pulse. The pulse-to-pulse variation of the second Stokes energy has to be taken into account in experiments when signal intensity depends on IR energy and there is no averaging over many laser pulses.

The generation of the infrared radiation at $\lambda = 2.92 \mu\text{m}$ by stimulated Raman scattering of Nd:YAG laser radiation ($\lambda = 1.06 \mu\text{m}$) in compressed deuterium was investigated in this chapter. In the presence of limiting factors such as an optical gas breakdown and damage to the input and exit windows of the RS by the focused pump laser beam, the conversion is strongly intensity dependent and the focusing conditions must be chosen with care. One of the key factors is to maintain high

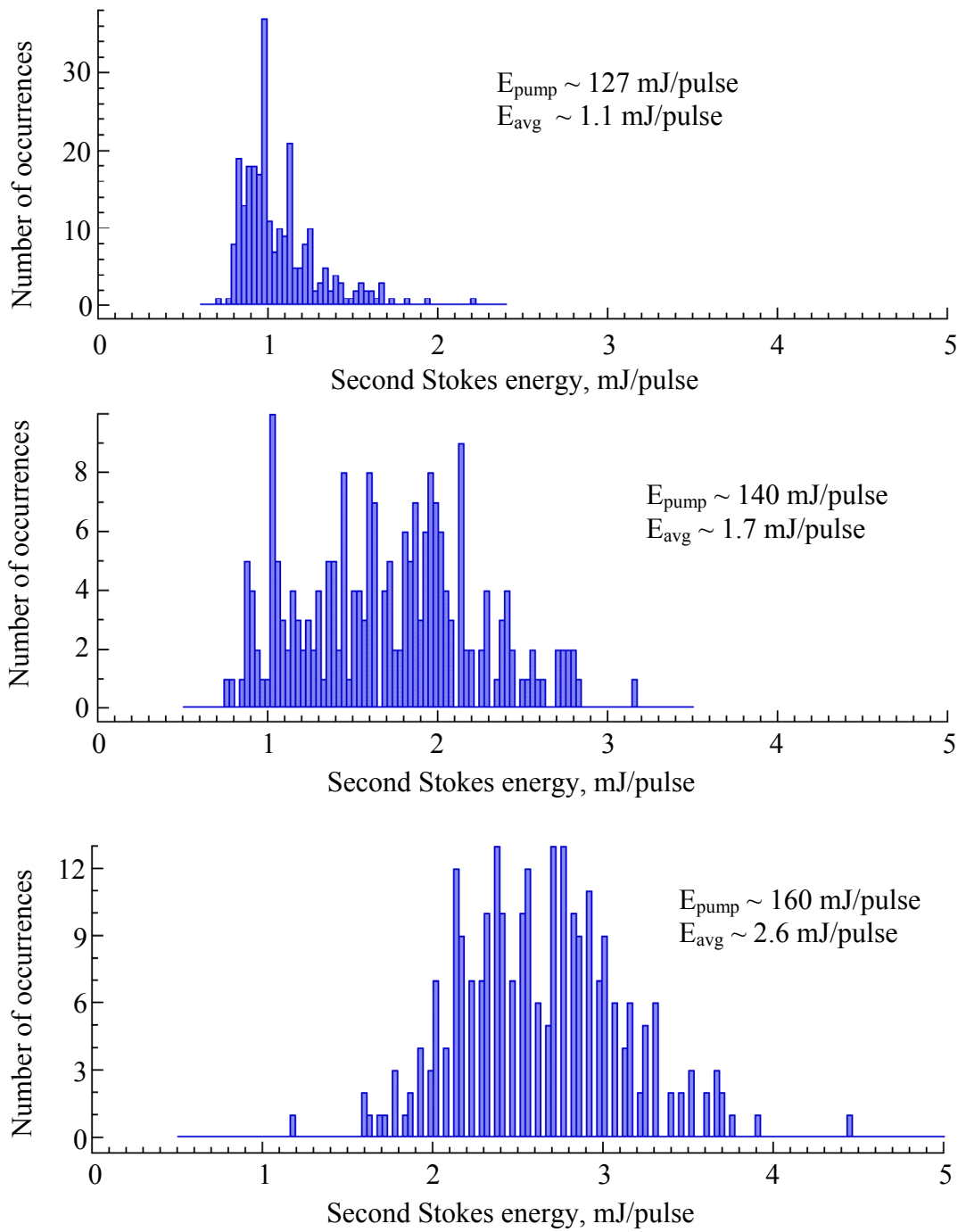


Figure 3.5 Distributions of the 2nd Stokes energies for ~250 consecutive laser shots at three different pump energies.

purity conditions of the deuterium gas in the RS cell to prevent the optical gas breakdown. It was found that the optimal focusing distance for the pump beam into the Raman cell is 1 m. Second Stokes conversion efficiency ~5% was obtained for deuterium pressures > 700 PSI. Pump laser energies > 200 mJ/pulse lead to optical breakdown and are difficult to use in the current RS design. The shot-to-shot stability of the second Stokes radiation decreases for pump laser energies greater than 130 mJ/pulse.

3.4 References

1. I. Fischer and T. Schultz, *Applied Physics B-Lasers and Optics*, **64**, 15, (1997).
2. C. Guntermann, V. Schulzvondergathen, and H.F. Dobele, *Appl. Opt.*, **28**, 135, (1989).
3. T.R. Loree, R.C. Sze, D.L. Barker, and P.B. Scott, *Ieee Journal of Quantum Electronics*, **15**, 337, (1979).
4. K. Sentrayan, A. Michael, and V. Kushawaha, *Applied Physics B-Lasers and Optics*, **62**, 479, (1996).
5. S. Godin, G. Megie, and J. Pelon, *Geophys. Res. Lett.*, **16**, 547, (1989).
6. W. Carnuth and T. Trickl, *Rev. Sci. Instrum.*, **65**, 3324, (1994).
7. D.G. Lancaster and J.M. Dawes, *Opt. Commun.*, **120**, 307, (1995).
8. D. Stern, C.A. Puliafito, E.T. Dobi, and W.T. Reidy, *Ophthalmology*, **95**, 1434, (1988).
9. W.R. Trutna and R.L. Byer, *Appl. Opt.*, **19**, 301, (1980).
10. Bloembergen, *American Journal of Physics*, **35**, 989, (1967).
11. R. Sussmann, T. Weber, E. Riedle, and H.J. Neusser, *Opt. Commun.*, **88**, 408, (1992).
12. A.D. Papayannis, G.N. Tsikrikas, and A.A. Serafetinides, *Applied Physics B-Lasers and Optics*, **67**, 563, (1998).
13. D.R. Lide, Editor, *CRC Handbook of Chemistry and Physics 75th Edition*, CRC Press: New York, 1998.
14. D.J. Brink, H.P. Burger, T.N. Dekock, J.A. Strauss, and D.R. Preussler, *Journal of Physics D-Applied Physics*, **19**, 1421, (1986).
15. L. deSchouepnikoff, V. Mitev, V. Simeonov, B. Calpini, and H. vandenBergh, *Appl. Opt.*, **36**, 5026, (1997).
16. T. Yagi and Y.S. Huo, *Appl. Opt.*, **35**, 3183, (1996).

Chapter 4: Trapping and Release of CO₂ Guest Molecules by Amorphous Ice

4.1 Introduction

Interactions of molecules with H₂O ices are of fundamental importance in a broad range of scientific fields such as atmospheric chemistry [1-3], cryobiology [4], and astrochemistry [5-11]. There are several distinct H₂O ice phases. Among these, amorphous ice has gained considerable attention as a model system for studying amorphous and glassy materials [12], and due to its importance in astrochemistry [5-11].

Amorphous ice, also referred to as amorphous solid water (ASW), can be prepared by vapor depositing H₂O onto a cold substrate (< 140 K) [13]. It is a metastable phase of ice with respect to the crystalline phase [14]. It is believed to be the most abundant component of comets, interstellar clouds, and planetary rings [5,15]. ASW does not display properties of a single well defined phase. For instance, there are discrepancies in the reported values of specific surface area [16-18], glass transition temperature [19,20], and the nature of supercooled water [19]. Recent studies show that ASW properties depend greatly on growth conditions [16] and the thermal history of the ASW [17,21,22].

Several studies indicate that ASW can trap volatile gas molecules [7,10,11,22-25]. This implies that volatile species can be present in interstellar ices at temperatures higher than their sublimation temperature. The ability of ASW to trap molecules depends on its morphology [23]. Concentrations of trapped molecules

also depend on how these molecules are deposited [23,25]. It was proposed that an increase in ASW temperature induces slight molecular rearrangements [23], and these rearrangements close escape pathways for the trapped molecules [23]. Indeed, there is evidence of ASW reorganization at temperatures well below the ASW-to-cubic ice transition [21].

Temperature programmed desorption (TPD) and IR spectroscopic studies of thin ASW films (< 100 layers) have shown that the release of trapped molecules occurs at several distinct temperatures [7,9,22-27]. This process does not depend on the binding energy of the guest molecules. The trapped molecules desorb during the phase transition, as well as during the sublimation of the cubic ice (CI) film. It is accepted that the release of guest molecules during the ASW-to-cubic ice transition occurs through pathways present in ASW during the phase transition [23].

The retention of guest molecules up to the CI sublimation temperature is not always observed [7,9,11,23]. It is unclear what mediates the ratio of trapped species released during the phase transition to trapped species that are retained within CI. Collings *et al.* reported that this ratio and the amount of guest species desorbing during CI sublimation depend on the ice film thickness [25]. It is not clear if this ratio can be manipulated (*e.g.*, independent of ASW thickness) by changing deposition conditions. Additionally, the nature of the site from which these molecules desorb remains speculative. Ayotte *et al.* [23] have suggested that this could be due to molecules being trapped in a simple pore, trapped in a clathrate hydrate cage, or buried under the water overlayer. Several studies show that only a few

molecules form clathrate hydrates under low temperature and UHV conditions [7,28].

The above issues were examined by using a combination of FTIR and TPD techniques. It was possible to monitor changes in the FTIR spectra of guest molecules trapped in the ASW, as well as the TPD traces of these trapped species. This permits comparison of FTIR and TPD spectra of the same samples, thereby providing information on the nature of the molecules that stay in ice after the phase transition. CO₂ has been shown to be a good candidate for probing ice morphology and studying the trapping and release of volatile molecules by ASW films [22]. Its large oscillator strength and narrow line widths facilitate the detection of small amounts of guest molecules and small frequency shifts.

4.2 Experimental

Experiments were carried out in an ultrahigh vacuum (UHV) chamber with a base pressure of $\sim 10^{-10}$ Torr. The experimental strategy and arrangement have been described in detail in the previous chapter, and will be outlined briefly here. The chamber is equipped with instrumentation to perform transmission FTIR and TPD studies. TPD spectroscopy was performed using a residual gas analyzer (Stanford Research Systems, RGA 300). FTIR spectroscopy was carried out using a Nicolet Protegé 460 spectrometer with a liquid nitrogen cooled InSb detector. Infrared radiation entered and exited the chamber through CaF₂ windows. It was brought to

a focus at the sample, and after exiting the chamber it was refocused onto the detector.

The substrate was a MgO single crystal (MTI) with typical dimensions of $\sim 1 \text{ mm} \times 10 \text{ mm} \times 10 \text{ mm}$. This was obtained by cleaving a MgO crystal twice in a dry nitrogen atmosphere. A cleaved MgO crystal with fresh (100) surfaces was quickly inserted into the UHV chamber. After baking the chamber and reaching the base pressure, the substrate was annealed in oxygen to remove oxygen vacancies and contaminants from the MgO(100) surface [29,30]. The surface temperature was measured using a *k*-type thermocouple glued to the front edge of the crystal with a high-temperature ceramic adhesive (Aremco 569).

The surface holder, which was used in previous FTIR studies [22], was modified to perform TPD (in addition to FTIR) and to keep the same level of sample cooling. Care was taken to minimize thermal gradients across the substrate. The substrate was attached to a thin copper plate ($\sim 0.3 \text{ mm} \times 10 \text{ mm} \times 14 \text{ mm}$) by laying the substrate on the plate and folding over two opposite edges of the plate onto the substrate. In this manner, only two thin strips ($\sim 1 \text{ mm} \times 10 \text{ mm}$) at the edges of the substrate were completely sandwiched by the plate. A square opening ($\sim 5 \text{ mm} \times 5 \text{ mm}$) in the middle of the copper plate allowed transmission FTIR experiments to be performed. The copper plate was connected with a stainless steel screw to one of two copper blocks attached to a liquid nitrogen reservoir. Using a sapphire disk and ceramic washers, these copper blocks were electrically isolated from each other and from the reservoir. The sample was resistively heated using a

homemade heater cemented (Aremco 569) onto the back of the copper plate. The heater was made from a tantalum wire (~ 0.4 mm) that was isolated from the copper plate by a ceramic thermocouple insulator (Omega ORX-020132). The wire was bent several times to form a rectangular shape (~ 10 mm \times 10 mm).

The reservoir was attached to a precision manipulator to provide XYZ translation and 360° rotation. A substrate temperature of ~ 90 K was obtained routinely by bubbling helium gas through liquid nitrogen in the reservoir. The sample temperature could be altered from 90 K to 500 K, and from room temperature to 700 K. The new surface holder design minimized mass spectrometer signals coming from the copper parts of the sample holder during TPD.

Purified and deionized H_2O was degassed by several freeze-pump-thaw cycles and dosed using a stainless steel tube (~ 4 mm diameter) connected to a leak valve. The distance from the tube to the substrate was ~ 50 mm. It was noticed that during backfilling of the chamber with H_2O (5×10^{-8} Torr) there was a small increase in the $m/e = 44$ (*i.e.*, $^{12}\text{CO}_2^+$) signal. In addition, the mass spectrometer showed an increase of $m/e = 44$ signal during desorption of the H_2O film from the substrate, whereas the FTIR spectrum indicated clearly that there was no CO_2 present on the substrate. The source of the aforementioned CO_2 is unknown. To lessen such complications, $^{13}\text{CO}_2$ (Icon Isotopes, 99%) was used instead of $^{12}\text{CO}_2$. The $^{13}\text{CO}_2$ sample was introduced into the chamber through a separate leak valve and dosing line.

Substrates were heated to 400 K to desorb contaminants before performing experiments. FTIR spectra (200 - 500 scans) covering the region 2000 – 4000 cm^{-1} were recorded at 1 cm^{-1} resolution. A background spectrum of the MgO(100) substrate was collected at 90 K. The substrate was tilted such that the angle between the propagation vector of the *p*-polarized IR radiation and the surface normal was 50°. In TPD experiments, a temperature ramp rate of ~ 1 K/s was used, and $m/e = 18$ (H_2O^+) and 45 ($^{13}\text{CO}_2^+$) were monitored with the mass spectrometer.

The thickness of a water film was estimated by comparing the integrated TPD intensity of the water film (approximately proportional to exposure time at constant dosing pressure) with that of a water monolayer. The water monolayer coverage was obtained using TPD, as in a previous study [30]. The $^{13}\text{CO}_2$ coverage could not be obtained easily from our experiments. The $^{13}\text{CO}_2$ TPD signal could not be calibrated due to the absence of a distinct $^{13}\text{CO}_2$ TPD feature that can be ascribed to the monolayer. This can be explained by a negligible difference in the binding energy of $^{13}\text{CO}_2$ molecules to $^{13}\text{CO}_2$ molecules, and $^{13}\text{CO}_2$ molecules to the ASW interface or to the MgO(100) surface [11,31,32].

4.3 Results

We have studied $^{13}\text{CO}_2$ interactions with amorphous and crystalline ice by means of TPD and FTIR spectroscopy. The experimental results consist mainly of

TPD spectra of $^{13}\text{CO}_2$ desorbing from ASW and FTIR spectra of $^{13}\text{CO}_2$ (ν_3 region) trapped within the ASW film.

The $^{13}\text{CO}_2$ deposited on a MgO(100) surface at 90 K forms a polycrystalline film. The IR spectrum of the film exhibits two distinct bands (Figure 4.1a) that can be ascribed to the longitudinal (LO) and the transverse optical (TO) modes in crystalline $^{13}\text{CO}_2$ [33]. Figure 4.1b shows the TPD spectrum of $^{13}\text{CO}_2$ desorbing from a MgO(100) surface. Only one feature, centered at 106 K, is evident. This peak corresponds to sublimation of $^{13}\text{CO}_2$. These results are similar to TPD results obtained from CO_2 on other surfaces [25].

When $^{13}\text{CO}_2$ is deposited on top of the ASW film at 90 K, three peaks are observed in the $^{13}\text{CO}_2$ TPD trace (Figure 4.2a). The TPD trace can be divided into two regions: low temperature (< 110 K) and high temperature (> 160 K). The peak at 106 K is similar to the feature observed for CO_2 desorbing from MgO(100) and is thus attributed to $^{13}\text{CO}_2$ desorption from atop the ASW film. For ASW films of the same thickness, the intensity of this peak increases with $^{13}\text{CO}_2$ coverage.

The TPD features at 165 and 185 K are assigned to $^{13}\text{CO}_2$ desorbing from the interior of the ASW film. For ASW films of the same thickness with low $^{13}\text{CO}_2$ coverages, the $^{13}\text{CO}_2$ TPD traces display only two TPD features at 165 and 185 K. The intensity of these peaks saturates as the $^{13}\text{CO}_2$ coverage increases and the 107 K feature appears. The intensity of the 107 K peak continues to increase as the

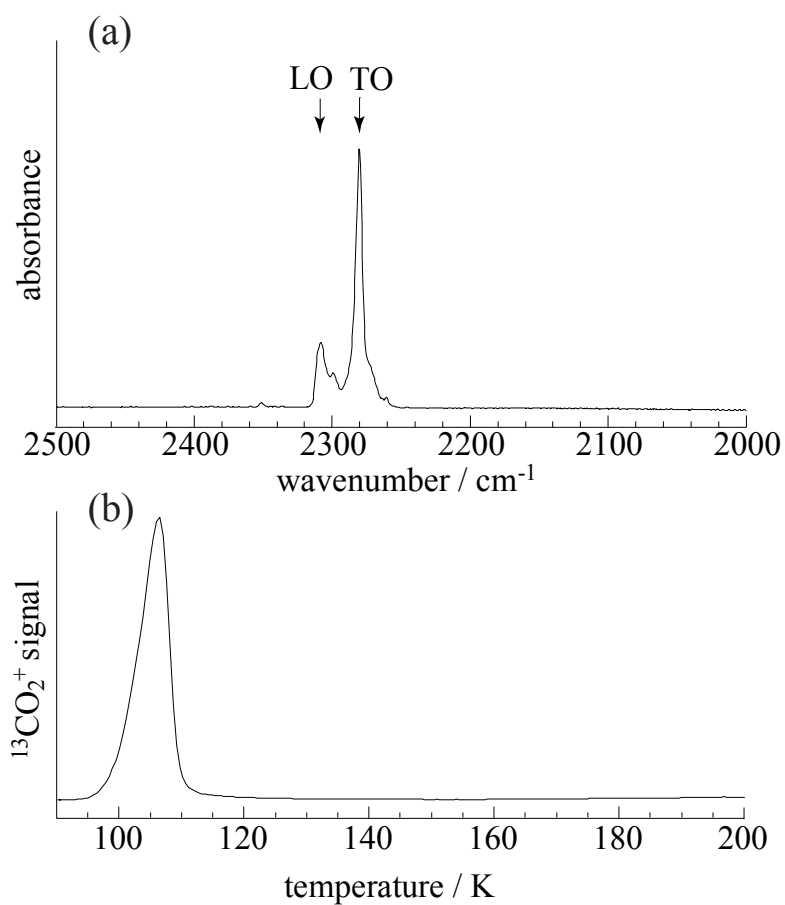


Figure 4.1. $^{13}\text{CO}_2$ was deposited (4×10^{-8} Torr, 3 minutes) onto MgO(100) at 90 K, at which time FTIR and TPD traces were recorded. Entries (a) and (b) show the $^{13}\text{CO}_2$ ν_3 spectral region and the TPD trace, respectively. The LO and TO modes of the $^{13}\text{CO}_2$ film are indicated in (a). TPD was carried out by heating the surface at 1 K / s while monitoring $m/e = 45$.

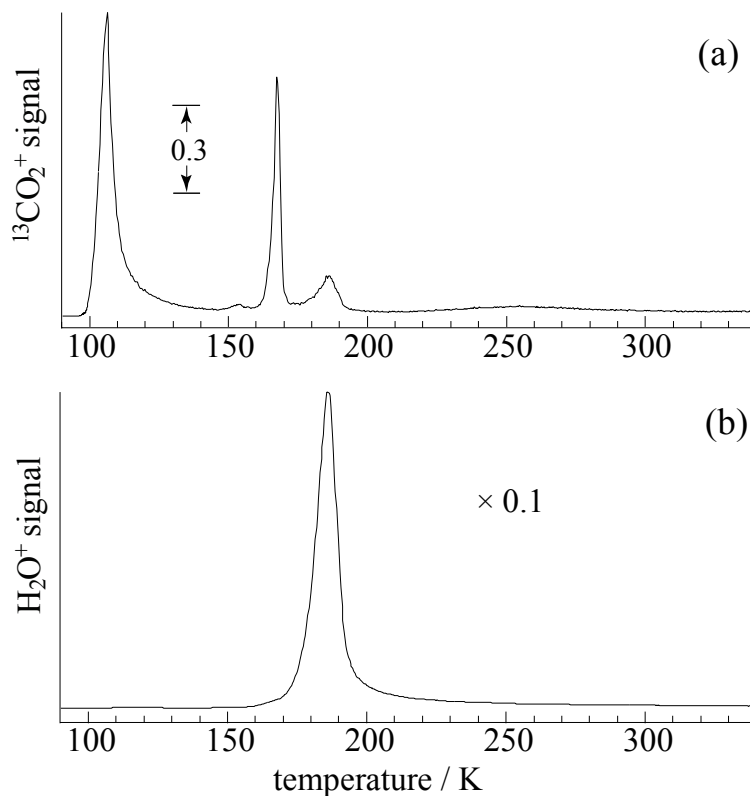


Figure 4.2. $^{13}\text{CO}_2$ was deposited (4×10^{-8} Torr, 30 s) onto an ASW film of ~ 40 layers (5×10^{-8} Torr, 8 minutes). H_2O and $^{13}\text{CO}_2$ desorption was monitored at $m/e = 18$ and 45, respectively. (a) and (b) show TPD traces for CO_2 and H_2O , respectively. Note that the H_2O TPD trace is scaled by a factor of 0.1. The scale factor of 0.3 shown in (a) is for comparison with Figures 4.3 - 4.5.

$^{13}\text{CO}_2$ coverage increases. The small bump at 155 K is due to $^{13}\text{CO}_2$ desorption from the sample holder. This was determined from experiments in which the sample holder position was varied relative to the mass spectrometer aperture. The 165 K peak (also known as the volcano peak [34]) corresponds to $^{13}\text{CO}_2$ desorption from the ASW film during the amorphous-to-cubic ice phase transition. The maximum peak intensity and the area of the 165 K peak are proportional to the ASW film thickness. The second peak (185 K) results from $^{13}\text{CO}_2$ that remains trapped after the ASW film has crystallized. The release of these $^{13}\text{CO}_2$ molecules occurs concurrently with desorption of the ice film (Figure 4.2b). Similar to the volcano peak, the maximum intensity and the area of this peak are proportional to the ASW film thickness.

FTIR spectra serve as good indicators of $^{13}\text{CO}_2$ in the ASW sample [11,22]. Figure 4.3a, trace i, shows the FTIR spectrum obtained after depositing $^{13}\text{CO}_2$ onto ASW at 90 K, annealing, and then re-cooling. Annealing the substrate to 115 K results in desorption of the solid $^{13}\text{CO}_2$ film atop ASW and the appearance of a residual band at 2275 cm^{-1} , similar to observations reported by Kumi *et al.* [22]. Figure 4.3a, trace ii, depicts the FTIR spectrum obtained after depositing $^{13}\text{CO}_2$ below ASW at 90 K, annealing, and then re-cooling. Deposition of $^{13}\text{CO}_2$ before the formation of ASW leads to an increase in the 2275 cm^{-1} band intensity.

The $^{13}\text{CO}_2$ TPD traces (obtained after recording the FTIR spectra shown in Figure 4.3a) of $^{13}\text{CO}_2$ deposited atop ASW and $^{13}\text{CO}_2$ deposited before ASW

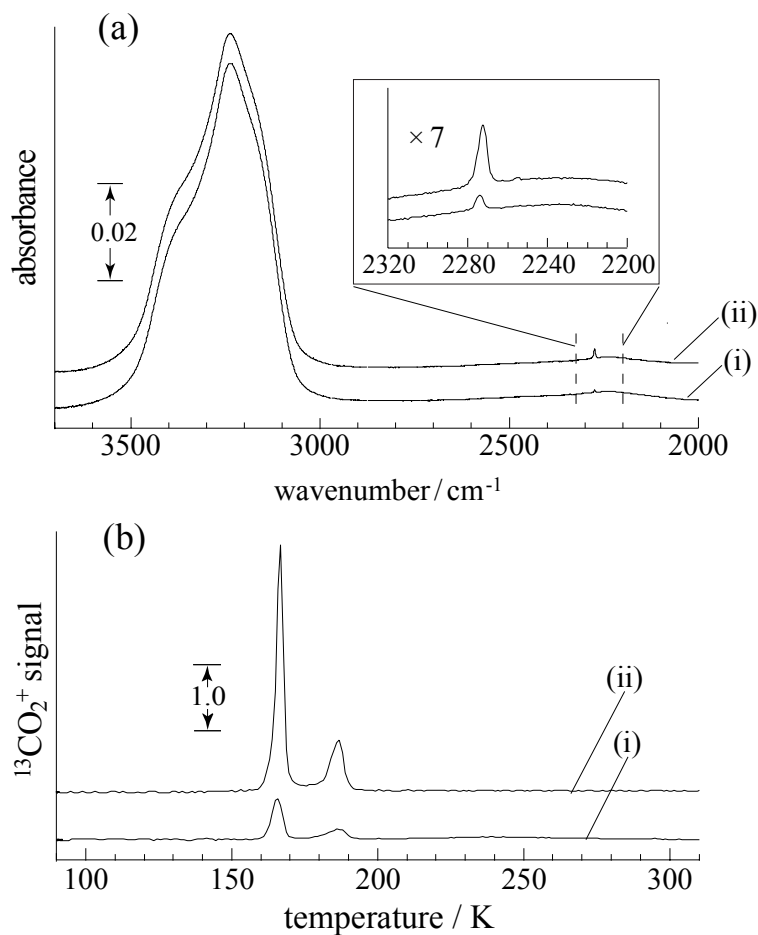


Figure 4.3. (a) FTIR spectra (*p*-polarization) of (i) ASW film (~40 layers) exposed to $^{13}\text{CO}_2$ and (ii) ASW film (~40 layers) deposited onto $^{13}\text{CO}_2$ film. Each sample was annealed to 115 K and re-cooled to 90 K. CO_2 was deposited at 4×10^{-8} Torr for 30 s. The inset shows the expanded scale of the $^{13}\text{CO}_2$ ν_3 region. (b) TPD spectra of $^{13}\text{CO}_2$ recorded for the samples in (a): (i) ASW film (~40 layers) exposed to $^{13}\text{CO}_2$ and (ii) ASW film deposited onto $^{13}\text{CO}_2$ film (TPD spectra were recorded after FTIR spectra). The scale factor of 1.0 is for comparison with Figures 4.2, 4.4, and 4.5.

formation (samples were annealed to 115 K) display the aforementioned two high-temperature TPD peaks. The intensities of both of these features are greater for the TPD trace from the sample in which $^{13}\text{CO}_2$ was deposited prior to ASW formation. However, the ratio of the peak area of the volcano peak to the peak area of the co-desorption peak is the same for both samples, as seen in Figure 4.3b, *i.e.*, this ratio does not depend on deposition sequence. In addition, it does not change with ice thickness.

Codeposition of $^{13}\text{CO}_2$ and H_2O increases the amount of $^{13}\text{CO}_2$ that desorbs during the phase transition. Figure 4.4b depicts $^{13}\text{CO}_2$ TPD traces obtained when $^{13}\text{CO}_2$ and H_2O are co-deposited using separate dosers. For $^{13}\text{CO}_2$ partial pressures less than 0.25 of the H_2O partial pressure, there is no desorption in the low temperature region. Only the two high temperature (*i.e.*, > 160 K) features are present. The intensity of the volcano peak depends on the $^{13}\text{CO}_2$ partial pressure during deposition. The TPD co-desorption feature at 185 K does not change significantly with $^{13}\text{CO}_2$ partial pressure.

The infrared absorption intensity of the ν_3 band depends on the partial pressure of $^{13}\text{CO}_2$ in the codeposition of $^{13}\text{CO}_2$ and H_2O (Figure 4.4a). The intensity of this band increases with $^{13}\text{CO}_2$ partial pressure. The area of the 2275 cm^{-1} band is approximately proportional to the amount of $^{13}\text{CO}_2$ that desorbs during thermal

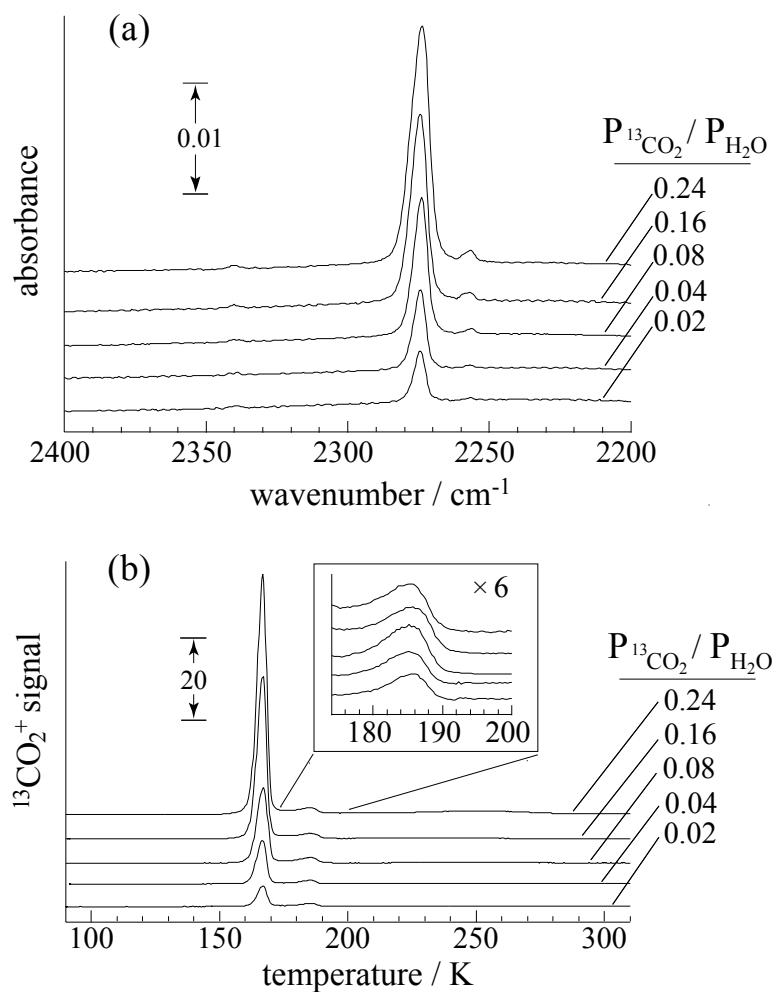


Figure 4.4. TPD and FTIR spectra of co-deposited (through separate dosers) $^{13}\text{CO}_2$ with H_2O : H_2O pressures and exposure times were the same in all experiments (5×10^{-8} Torr, 8 minutes); $^{13}\text{CO}_2$ pressures are given as fractions of the H_2O pressure $P_{\text{CO}_2} / P_{\text{H}_2\text{O}}$. Samples were annealed to 115 K and re-cooled to 90 K before recording each trace. Spectra are offset for clarity. (a) FTIR spectra (*p*-polarization); the bumps at 2256 cm^{-1} are due to $^{13}\text{C}^{18}\text{O}^{16}\text{O}$ (b) TPD spectra; the inset shows an expanded scale of the $^{13}\text{CO}_2$ codesorption peak (*i.e.*, $^{13}\text{CO}_2$ desorbing with the polycrystalline water film). TPD traces of H_2O were approximately the same.

desorption, *i.e.*, it is proportional to the areas of the volcano and co-desorption peaks.

Annealing ASW to 165 K leads to crystallization. Most of the trapped $^{13}\text{CO}_2$ escapes during the ASW-to-cubic ice transition. The intensity of the feature at 2275 cm^{-1} is reduced significantly after crystallization. Figure 4.5a shows FTIR spectra of three samples annealed to 165 K that were formed by: depositing $^{13}\text{CO}_2$ atop ASW (trace i), depositing $^{13}\text{CO}_2$ underneath ASW (trace ii), and co-depositing $^{13}\text{CO}_2$ and H_2O during ASW formation. The broad H_2O feature centered at 3250 cm^{-1} changes upon annealing to 165 K because of the ASW-to-cubic ice phase transition [35]. For the samples used in Figure 4.5a, the 2275 cm^{-1} band has largest intensity for $^{13}\text{CO}_2$ co-deposited with H_2O , and it is essentially zero for $^{13}\text{CO}_2$ deposited atop ASW.

The TPD trace of $^{13}\text{CO}_2$ trapped in cubic ice exhibits a single peak at 185 K. Figure 4.5b shows TPD traces of $^{13}\text{CO}_2$ desorbing from samples annealed to 165 K, which were formed by depositing $^{13}\text{CO}_2$ atop ASW (trace i), depositing $^{13}\text{CO}_2$ underneath ASW (trace ii), and co-depositing $^{13}\text{CO}_2$ and H_2O during ASW formation. The intensities of the 185 K TPD peaks behave similarly to the $^{13}\text{CO}_2$ IR feature. Namely, the maximum peak intensity and the peak area of the $^{13}\text{CO}_2$ TPD peak at 185 K are proportional to the maximum band intensity and integrated band area of the $^{13}\text{CO}_2$ 2275 cm^{-1} IR feature, respectively.

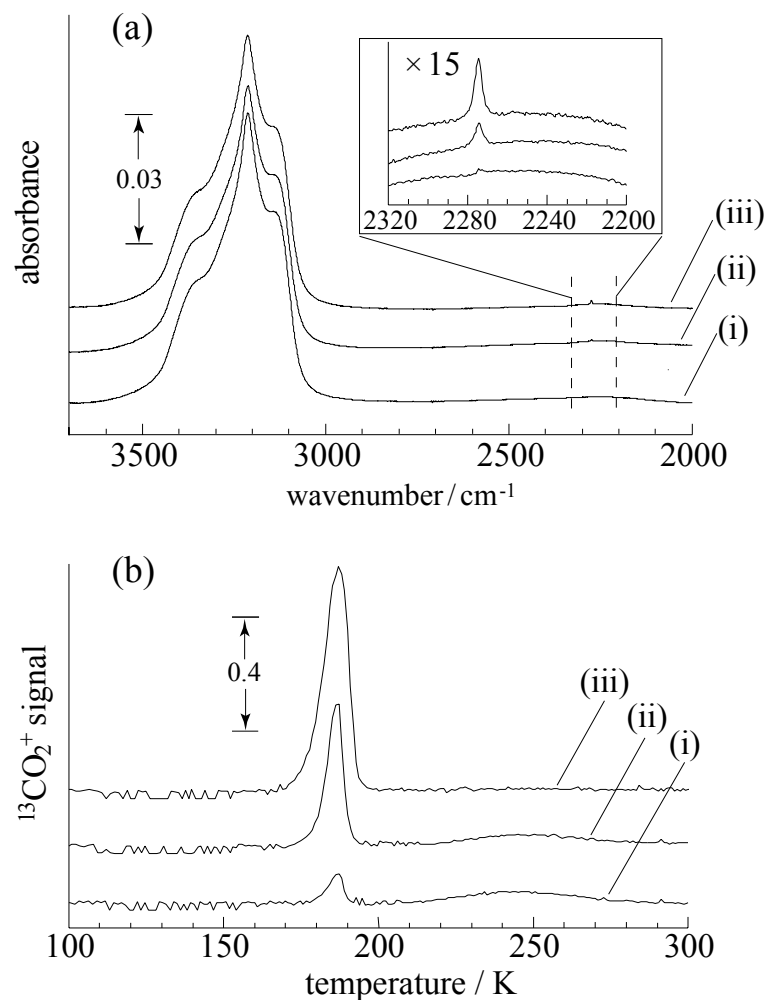


Figure 4.5. (a) FTIR spectra (*p*-polarization): (i) $^{13}\text{CO}_2$ deposited (4×10^{-8} Torr, 30 *s*) onto ASW film; (ii) $^{13}\text{CO}_2$ deposited (4×10^{-8} Torr, 30 *s*) before formation of ASW film; and (iii) $^{13}\text{CO}_2$ (2×10^{-9} Torr) codeposited with H_2O . Each sample was annealed to 165 K and recooled to 90 K. The H_2O exposure was approximately the same (5×10^{-8} Torr, 8 minutes) for all experiments. The inset shows the expanded scale of the $^{13}\text{CO}_2$ ν_3 region. (b) TPD spectra were recorded for the samples in (a) immediately after recording the FTIR spectra.

4.4 Discussion

The inclusion of guest molecules into ASW films depends on how these molecules are deposited and on film structure [16,23,25]. It is widely accepted that some of the guest molecules within porous ASW films can be trapped upon annealing [7,9-11,24,25,36,37]. The transport and trapping of guest molecules depend on the ASW pore network, the trapping sites, and changes that occur in the network upon annealing. The nature of trapping sites is hard to deduce by using TPD alone [23]. The present study of $^{13}\text{CO}_2$ transport and trapping in ASW films combines TPD and FTIR. Due to its sensitivity to the local environment and changes that occur upon annealing, the IR signature of the trapped molecules provides useful information.

It has been shown that CO_2 guest molecules dosed at 90 K possess enough mobility to diffuse into the porous ASW films [22]. Upon saturation of the sites within the film that can be accessed (*i.e.*, from either above or below), CO_2 forms a solid crystalline film atop ASW [22]. The TPD peak at 107 K is due to $^{13}\text{CO}_2$ desorbing from the ASW surface and from sites within the film that remain connected to the surface even after annealing (Figure 4.2). The TPD spectrum of $^{13}\text{CO}_2$ deposited underneath the film also shows the 107 K peak. This low-temperature peak shifts to slightly higher temperatures with increasing film thickness. The presence of the 107 K peak suggests that the ASW overlayer is porous enough to provide pathways connected to the ASW surface for $^{13}\text{CO}_2$

molecules to escape. Other studies showed that for dense ASW films guest molecules deposited underneath ASW stay trapped until the ice phase transition [23].

When $^{13}\text{CO}_2$ is deposited on top or underneath the ASW film, there is no appreciable desorption of $^{13}\text{CO}_2$ in the temperature range 115 – 160 K. Molecules trapped during thermally induced changes in ASW morphology do not escape until 160 K. The FTIR spectra (Figures 4.3a and 4.4a) show the presence of trapped $^{13}\text{CO}_2$ within the film. The amount of trapped $^{13}\text{CO}_2$ depends strongly on whether $^{13}\text{CO}_2$ was deposited on top or underneath the ASW.

The ASW film is able to trap ~ 4 times more molecules when $^{13}\text{CO}_2$ is deposited underneath it. This number was obtained by comparing the areas of the $^{13}\text{CO}_2$ ν_3 bands for $^{13}\text{CO}_2$ deposited atop and under the ASW (Figure 4.3a). A similar result was obtained by comparing the amount of trapped $^{13}\text{CO}_2$ desorbing during TPD (which is proportional to the area of the high temperature TPD peaks) for $^{13}\text{CO}_2$ deposited atop and under the ASW (Figure 4.3b). This suggests that guest molecules deposited underneath the porous ASW film sample more binding sites in the ASW as the temperature rises during annealing. This is intuitive, because they are inhibited from evaporating relative to those that access the bulk from above.

Most of the trapped $^{13}\text{CO}_2$ escapes during the ASW-to-cubic ice phase transition, and the rest desorbs during cubic ice removal at 185 K. The abrupt

release of guest molecules during crystallization apparently occurs through connected desorption pathways in the film; these pathways can be formed during the phase transition [23,34]. However, some molecules are not released from the cubic ice until the sublimation of the film (Figure 4.2). It is unlikely that these molecules simply reside under the H₂O overlayer, because when ASW is deposited on top of ¹³CO₂ the amount of trapped ¹³CO₂ is proportional to the ice film thickness. Probably these molecules reside within the cubic ice film. Presumably, they cannot escape from sites within the film because no connection to the outer surface has been formed during crystallization.

The TPD experiments show that the ratio of the areas of the co-desorption peak to the volcano peak does not change for ¹³CO₂ deposited atop or underneath the ASW. This conclusion can also be made by comparing the areas of the ¹³CO₂ v₃ band for ¹³CO₂ isolated after annealing to 115 K and 165 K. This supports the previous statement that depositing ¹³CO₂ molecules underneath the ASW simply allows them to better sample sites in the ASW film during transport through it.

Codeposition of ¹³CO₂ and H₂O affects trapping and desorption. For $P_{\text{CO}_2}/P_{\text{H}_2\text{O}} < 0.25$, all of the ¹³CO₂ that is absorbed by ASW becomes trapped upon annealing. The amount of trapped ¹³CO₂ is proportional to its partial pressure. The majority of these molecules are released during crystallization. In fact, both TPD and IR reveal that different ¹³CO₂ partial pressures (within 0.02 – 0.25 of the H₂O partial

pressure) do not affect significantly the amount of $^{13}\text{CO}_2$ released during removal of the cubic ice film at 185 K. However, the amount of $^{13}\text{CO}_2$ that desorbs when $^{13}\text{CO}_2$ is co-deposited with H_2O is larger than the amount that desorbs when $^{13}\text{CO}_2$ is deposited atop or under the ASW film.

Codeposition at $P_{\text{CO}_2}/P_{\text{H}_2\text{O}} > 0.25$ leads to saturation of the high-temperature TPD features. It also leads to appearance of the low-temperature TPD peak at 107 K, broadening of the $^{13}\text{CO}_2$ ν_3 feature and eventually (with increasing $^{13}\text{CO}_2$ partial pressures) appearance of the LO and TO bands. All of these confirm the formation of solid polycrystalline $^{13}\text{CO}_2$ atop the ASW. Thus, there is saturation of the trapping sites within the ASW film at high $^{13}\text{CO}_2$ pressures. The hydrogen-bonding interaction between H_2O molecules is much stronger than $\text{H}_2\text{O} - \text{CO}_2$ and $\text{CO}_2 - \text{CO}_2$ interactions [11,38]. Based on the saturation of the trapping sites and the aforementioned interaction strength, we speculate that codeposition of $^{13}\text{CO}_2$ does not alter the ASW structure significantly, under the present experimental conditions. Codeposition probably affects how the $^{13}\text{CO}_2$ molecules sample sites within the ASW film (*i.e.*, codeposition allows $^{13}\text{CO}_2$ to populate sites that are not directly connected to the vacuum).

The largest amount of $^{13}\text{CO}_2$ that can be trapped during codeposition is roughly one $^{13}\text{CO}_2$ molecule for every thirty H_2O molecules. This was obtained by comparing the area of the H_2O TPD peak to the area of the high temperature $^{13}\text{CO}_2$

TPD peaks. Approximately the same ratio is obtained using the integrated adsorption cross section per molecule of the CO_2 ν_3 band [39], together with the assumption that the ASW layer thickness is 0.4 nm and the ASW density is $0.9 \text{ g}\cdot\text{cm}^{-3}$. Most likely this ratio will depend on the deposition conditions, *e.g.*, via collimated molecular beam or when much thicker ASW films created [7,16,40].

Species that desorb during the sublimation of the ice film can be isolated in the film by annealing ASW- CO_2 samples to 165 K. The position of the $^{13}\text{CO}_2$ ν_3 band at 2275 cm^{-1} is the same for samples annealed to 115 and 165 K (compare Figures 4.3a, 4.4a, and 4.5a). The robustness of the $^{13}\text{CO}_2$ ν_3 band frequency suggests that trapping sites for the $^{13}\text{CO}_2$ that escapes from the ice during the phase transition are similar to those that desorb during ice film depletion. Previous IR studies of CO_2 clathrate hydrates [41-43] reported CO_2 ν_3 band positions that are shifted from the ν_3 band position for CO_2 trapped in ASW. Thus, it is unlikely that the release of $^{13}\text{CO}_2$ at 185 K (concurrent with sublimation of ice film) is due to molecules trapped in clathrate hydrate cages. We speculate that this release is related to molecules trapped in cavities within the ASW film similar to ones that trap the $^{13}\text{CO}_2$ released during the crystallization.

The area of the $^{13}\text{CO}_2$ ν_3 band is proportional to the number of trapped $^{13}\text{CO}_2$ molecules and the infrared absorption cross section of the $^{13}\text{CO}_2$ molecule. The area of the $^{13}\text{CO}_2$ TPD peaks at 165 and 185 K is proportional to the number of

desorbing $^{13}\text{CO}_2$ molecules. Thus, the ratio of the $^{13}\text{CO}_2$ ν_3 band area to the total area of the $^{13}\text{CO}_2$ TPD peaks at 165 and 185 K (or only the area of the 185 K peak if the sample was annealed to 165 K) should be proportional to the IR integrated cross section per molecule. In our experiments, this ratio was the same (within a 25% error margin) for $^{13}\text{CO}_2$ trapped within ASW ($^{13}\text{CO}_2$ deposited atop ASW, under ASW, and co-deposited with H_2O) and for $^{13}\text{CO}_2$ solid films. This indicates little change in the $^{13}\text{CO}_2$ infrared transition dipole moments in our experiments. This suggests that there is no significant difference in the local environment for $^{13}\text{CO}_2$ molecules trapped in the various sites.

The general assumption that ASW films are always porous is not always true. For instance, several studies show that the porosity and density of amorphous ice films significantly depend on factors such as the growth temperature and angle of deposition [6,16,40]. Only porous ASW is believed to trap guest molecules residing within its pores by subtle alterations in its structure. Moreover, for guest species to be retained, they must be located within pores during these structural alterations. At a specified temperature, the residence times of a molecule in an ASW pore depend on the molecule as well as its desorption rate. Thus, experimental conditions conducive to trapping different species in porous ASW are expected to vary. Our observations suggest that (i) the ASW films we prepare at 90 K are porous and (ii) at 105 K, some $^{13}\text{CO}_2$ is unable to desorb prior to the aforementioned ASW structural changes.

We were also able to alter the number of $^{13}\text{CO}_2$ guest molecules in the film by varying the method of deposition (*i.e.*, on top of the ASW, underneath the ASW, and codeposition). It has been suggested that the codeposition of H_2O with guest species may influence the structure of the ASW film [11,25]. No significant differences in the desorption temperatures and the IR signatures of the trapped species were discernible for the various methods of guest molecule deposition used in the studies reported herein. However, as mentioned previously, the ratio of trapped molecules released during the phase transition to trapped molecules that codesorb with crystalline ice depends upon the method of deposition.

Bar-Nun and coworkers observed that molecules trapped in thick (several μm) ASW films following codeposition were ejected at several distinct temperatures [7,37]. In contrast, our results indicate that the release of trapped species occurs in two distinct temperature regimes, which is consistent with other studies of thin (less than $1\ \mu\text{m}$) ASW films. It is possible therefore that there may be slight differences in the processes mediating the release of trapped species in thick and thin ASW films.

4.4 Summary

The experimental study described in this chapter has explored issues of the transport and trapping of guest molecules in ASW films. The probe molecule $^{13}\text{CO}_2$ provides IR and TPD spectral signatures that enable the distinction between the

surface films and their bulk inclusions in ASW hosts. Due to its sensitivity to the local environment the IR signature of the trapped $^{13}\text{CO}_2$ molecules provides valuable information about the nature of the trapping site. Good sensitivity is achieved because $^{13}\text{CO}_2$ has strong ν_3 absorption and relatively narrow spectral features, e.g., compared to those of the ASW host. The conclusions listed below constitute a qualitative picture of the associated phenomena.

- (1) The ASW films prepared at the deposition conditions used in the experiments reported herein are porous.
- (2) The $^{13}\text{CO}_2$ guest molecules dosed at 90 K possess enough mobility to diffuse into the porous ASW films.
- (3) Guest molecules are trapped within the ASW upon annealing it to temperatures > 105 K.
- (4) Guest molecules trapped within ASW films remain there as the temperature is increased from 90 K to 160 K. Some trapped molecules are released abruptly during the ASW to cubic ice transition (~ 165 K) while others remain within the cubic ice.
- (5) The number of $^{13}\text{CO}_2$ guest molecules in the film can be changed by varying the method of deposition (*i.e.*, on top of the ASW, underneath the ASW, and co-deposition).
- (6) $^{13}\text{CO}_2$ guest molecules retained in the crystalline ice are trapped in cavities similar to ones that trap $^{13}\text{CO}_2$ expelled during the phase transition.

4.5 References

1. B.S. Berland, D.E. Brown, M.A. Tolbert, and S.M. George, *Geophys. Res. Lett.*, **22**, 3493, (1995).
2. J.D. Graham and J.T. Roberts, *J. Phys. Chem.*, **98**, 5974, (1994).
3. S. Solomon, *Nature*, **347**, 347, (1990).
4. D. Rasmussen and A. Mackenzi, *J. Phys. Chem.*, **75**, 967, (1971).
5. P. Jenniskens and D.F. Blake, *Science*, **265**, 753, (1994).
6. K.P. Stevenson, G.A. Kimmel, Z. Dohnalek, R.S. Smith, and B.D. Kay, *Science*, **283**, 1505, (1999).
7. A. Bar-Nun, G. Herman, D. Laufer, and M.L. Rappaport, *Icarus*, **63**, 317, (1985).
8. L.J. Allamandola, S.A. Sandford, A.G.G.M. Tielens, and T.M. Herbst, *Astrophys. J.*, **399**, 134, (1992).
9. L.J. Allamandola, S.A. Sandford, and G.J. Valero, *Icarus*, **76**, 225, (1988).
10. S.A. Sandford and L.J. Allamandola, *Icarus*, **76**, 201, (1988).
11. S.A. Sandford and L.J. Allamandola, *Astrophys. J.*, **355**, 357, (1990).
12. C.A. Angell, *Science*, **267**, 1924, (1995).
13. M.G. Sceats and S.A. Rice, in *Water: A Comprehensive Treatise*, F. Franks, Editor; Plenum Press: New York, 1982.
14. C.A. Angell, *Annu. Rev. Phys. Chem.*, **34**, 593, (1983).
15. R. Smoluchowski, *Science*, **201**, 809, (1978).
16. G.A. Kimmel, K.P. Stevenson, Z. Dohnalek, R.S. Smith, and B.D. Kay, *J. Chem. Phys.*, **114**, 5284, (2001).
17. C. Manca, C. Martin, and P. Roubin, *Chem. Phys. Lett.*, **364**, 220, (2002).
18. R. Pletzer and E. Mayer, *J. Chem. Phys.*, **90**, 5207, (1989).

19. S.M. McClure, D.J. Safarik, T.M. Truskett, and C.B. Mullins, *J. Phys. Chem. B*, **110**, 11033, (2006).
20. R.S. Smith and B.D. Kay, *Nature*, **398**, 788, (1999).
21. C. Manca, C. Martin, and P. Roubin, *Chem. Phys.*, **300**, 53, (2004).
22. G. Kumi, S. Malyk, S. Hawkins, H. Reisler, and C. Wittig, *J. Phys. Chem. A*, **110**, 2097, (2006).
23. P. Ayotte, R.S. Smith, K.P. Stevenson, Z. Dohnalek, G.A. Kimmel, and B.D. Kay, *J. Geophys. Res. Plan.*, **106**, 33387, (2001).
24. R.L. Hudson and B. Donn, *Icarus*, **94**, 326, (1991).
25. M.P. Collings, M.A. Anderson, R. Chen, J.W. Dever, S. Viti, D.A. Williams, and M.R.S. McCoustra, *Mon Not R Astron Soc*, **354**, 1133, (2004).
26. J.D. Graham, J.T. Roberts, L.A. Brown, and V. Vaida, *J. Phys. Chem.*, **100**, 3115, (1996).
27. J.E. Schaff and J.T. Roberts, *Langmuir*, **14**, 1478, (1998).
28. G. Natesco and A. Bar-Nun, *Icarus*, **148**, 456, (2000).
29. M. Korolik, M.M. Suchan, M.J. Johnson, D.W. Arnold, H. Reisler, and C. Wittig, *Chem. Phys. Lett.*, **326**, 11, (2000).
30. S. Hawkins, G. Kumi, S. Malyk, H. Reisler, and C. Wittig, *Chem. Phys. Lett.*, **404**, 19, (2005).
31. S. Briquez, A. Lakhlifi, S. Picaud, and C. Girardet, *Chem. Phys.*, **194**, 65, (1995).
32. P.U. Andersson, M.B. Nagard, G. Witt, and J.B.C. Pettersson, *J. Phys. Chem. A*, **108**, 4627, (2004).
33. M.A. Ovchinnikov and C.A. Wight, *J. Chem. Phys.*, **99**, 3374, (1993).
34. R.S. Smith, C. Huang, E.K.L. Wong, and B.D. Kay, *Phys. Rev. Lett.*, **79**, 909, (1997).
35. W. Hagen, A.G.G.M. Tielens, and J.M. Greenberg, *Chem. Phys.*, **56**, 367, (1981).

36. A. Bar-Nun, J. Dror, E. Kochavi, and D. Laufer, *Phys. Rev. B*, **35**, 2427, (1987).
37. A. Bar-Nun, I. Kleinfeld, and E. Kochavi, *Phys. Rev. B*, **38**, 7749, (1988).
38. R.S. Smith and B.D. Kay, *Surf. Rev. Lett.*, **4**, 781, (1997).
39. H. Yamada and W.B. Person, *J. Chem. Phys.*, **41**, 2478, (1964).
40. Z. Dohnalek, G.A. Kimmel, P. Ayotte, R.S. Smith, and B.D. Kay, *J. Chem. Phys.*, **118**, 364, (2003).
41. D. Blake, L. Allamandola, S. Sandford, D. Hudgins, and F. Freund, *Science*, **254**, 548, (1991).
42. F. Fleyfel and J.P. Devlin, *J. Phys. Chem.*, **95**, 3811, (1991).
43. J. Hernandez, N. Uras, and J.P. Devlin, *J. Phys. Chem. B*, **102**, 4526, (1998).

Chapter 5: Laser Induced Desorption of Water Molecules:

Preliminary Results and Future Work

5.1 Introduction

Water ice is ubiquitous in nature and plays a significant role in many areas including biology [1,2], geology [2], physics [2], astrochemistry [3-5] and atmospheric and environmental chemistry [2,6-8]. Studies of chemical and physical processes occurring at the gas-ice interface and in the bulk of amorphous and crystalline ice are motivated by both fundamental and applied questions. Surface and bulk diffusion phenomena are closely related to the growth of crystalline and amorphous ice [2,9,10], amorphous ice crystallization [10], ice particle sintering [2], and the formation of a "liquidlike" layer on ice surfaces [11,12]. Diffusion processes are also related to various relaxation and transport properties in ice including mechanical and dielectric relaxation, electrical conductivity and ion mobility, and defect formation and migration [2]. The mechanisms for many important reactions between adsorbed molecules on ice involve reactant adsorption, possible dissociation, surface and/or bulk diffusion, possible formation of reactive intermediates, product surface and/or bulk diffusion, and product desorption [9,13]. Moreover, the kinetics of these processes may be significantly affected by H₂O mobility on the ice surface and in the ice bulk.

Despite the importance of diffusion in ice, very few measurements have been conducted at temperatures < 150 K because of experimental difficulties. The main complication is that the transport processes in ice below 150 K are sluggish [9,14-

16] and it is nearly impossible to observe any diffusional changes with macroscopic samples. To better understand surface and bulk diffusion in ice, a new IR laser resonant desorption (LRD) technique has been developed by George and coworkers [17-21]. Another name for LRD is the laser induced desorption (LID). In this chapter this technique will be referred as LID technique. In this technique, the IR laser light resonantly excites O-H stretching vibrations in the H₂O molecules that form the ice. The vibrational energy quickly converts to heat, which promotes thermal desorption of water molecules. This technique provides a means to desorb a well defined volume of ice with submicron resolution [17,19]. The mass spectrometric detection of desorbing molecules provides a probe of the molecular composition of doped ice films throughout the entire thickness of the thin ice film (depth-profiling analysis of thin ice films) [17,19]. In addition, surface diffusion measurements on ice can be performed by using the LID "prepare-refill-prove technique" [20]. In the method, a laser pulse first desorbs the adsorbates from the ice surface. The surrounding adsorbates diffuse into the initially evacuated region, and finally, a second laser pulse probes the diffusional refilling [20].

By using the LID technique George and coworkers studied bulk and surface diffusion in crystalline (hexagonal) ice of a wide variety of molecules including hydrogen chloride, formic acid, ammonia, methanol, sulfur dioxide, butane, benzene, and sodium [18-21]. However there is a lack of studies of bulk and surface diffusion in amorphous ice and amorphous-crystalline ice mixtures. In addition, the understanding of laser induced desorption processes in nature is very

limited. There are a number of important questions that are still unanswered. For instance: Are there any ice phase changes induced by the laser radiation? What is the exact mechanism of the laser induced desorption? What is the surface temperature in the irradiation region? Is the laser induced desorption of water molecules simple zero-order thermal desorption with an Arrhenius dependence of the desorption rate on the surface temperature, or it is complicated by breaking of water through the crust of solid ice on top of the partially melted film in a manner similar to the "molecular volcano"? What happens in the ice region that borders the region that is removed by the laser radiation? These questions are closely related to several fundamental phenomena such as: coexistence of amorphous and crystalline phases, molecular transport across boundaries, growth and contraction of boundaries, trapping and release of gases, and metastable phases, including how they are created and destroyed.

Some of the above issues can be examined using the (LID) technique recently employed in our lab. It was possible to extend the detection capabilities of the LID technique by using a pulsed TOF mass spectrometry to detect the desorbing molecules. This allowed studies of the temporal distribution of desorbed species in addition to their molecular composition. The temporal distribution of desorbed molecules can provide important information about the temperature of the desorbed species, mechanism of desorption *etc.*

5.2 Experimental Details

The experiments were performed in the same UHV chamber that was described in detail in the second chapter of this dissertation (base pressure $\sim 2 \times 10^{-10}$ Torr). Briefly, the UHV chamber has three levels with the surface manipulator attached to the upper level. The manipulator provides XYZ translation and 360° rotation of the substrate. The substrate was attached to the manipulator using a surface holder. The sample was cooled to ~ 90 K by bubbling helium gas through liquid nitrogen in the reservoir. The substrate could be heated up to ~ 500 K at a rate of ~ 2 K/s using a homemade resistive heater attached to the surface holder.

The substrate was a MgO single crystal with dimensions of ~ 1 mm \times 10 mm \times 10 mm. The substrate was obtained by cleaving a larger MgO(100) single crystal in dry nitrogen atmosphere. The freshly cleaved substrate was quickly inserted into the chamber and, after baking, cleaned via an established procedure. The surface temperature was measured with a *k*-type thermocouple adhered with high temperature ceramic adhesive to the front edge of the substrate.

The upper level of the chamber was equipped with instrumentation to perform FTIR and TPD experiments. A Nicolet Protegé 460 FTIR spectrometer with a liquid nitrogen-cooled InSb detector and IR steering optics permitted infrared studies of the samples. TPD studies were carried out using a Stanford Research Systems residual gas analyzer (SRS RGA 300). The RGA had a stainless steel cone with a small aperture (~ 8 mm) that was used to screen out molecules not originating from the surface during TPD.

The LID experiments were performed in the middle level of the UHV chamber. The sample can be moved between top and middle levels without breaking vacuum to allow IR and LID experiments with the same sample. LID of water molecules was accomplished using 2.93 μm IR laser radiation. The laser system is described in the third chapter of this dissertation. The IR laser radiation was obtained by Raman shifting 1.064 μm laser light from a pulsed Nd:YAG (10 Hz, 9 ns) laser using a 1.1 m deuterium Raman cell at 900 psi. The output energy of the IR laser system was ~ 3.5 mJ/pulse at 2.93 μm . The pulse-to-pulse stability was roughly $\pm 40\%$ at a pulse repetition rate of 10 Hz.

The laser beam entered the chamber through a CaF_2 window positioned at the port on the middle level of the UHV chamber. The laser radiation was focused by a CaF_2 lens (50 cm focal length) onto the substrate at a normal incident angle. The spatial profile at the focus of the CaF_2 lens was determined by measuring the laser energy transmitted through a 50 μm diameter pinhole as the laser beam was translated across the aperture. The measured spatial distribution of the laser pulse was Gaussian with a beam waist size of ~ 500 μm (FWHM).

A TOF mass spectrometer (Jordan TOF Products) was used to detect molecules desorbing from the surface in the LID experiments. This mass spectrometer operates in a pulsed mode (as described in chapter 3). The ions are produced, extracted and accelerated in pulses (up to 200 kHz). The TOF mass spectrometer was attached to the middle level of the UHV chamber through a custom-made

flange adapter. It was positioned to allow the majority of the desorbed molecules to reach the ionization region of the TOF mass spectrometer.

Sample molecules were introduced into the UHV chamber using two precision leak valves (MDC ULV-075). Water was dosed using a separate leak valve than other gases. H₂O distilled and purified by osmosis was degassed by several freeze-pump-thaw cycles. CO₂ (Glimore 99.99%) was used without further purification. Water and CO₂ coverages were obtained by backfilling the chamber with H₂O and CO₂ vapors for fixed time periods.

In future experiments, crystalline domains or voids (empty spaces) within an ASW film will be created by irradiating the surface with IR laser beam through a stainless steel wire mesh. The wire mesh can be positioned in front of the surface using a precision XYZ manipulator (Huntington Laboratories PM-600) and a custom-made mesh holder. The IR laser beam can be translated across the sample surface using a piezo-motor-driven mirror mount (Newport AG-M100L), whose movement is controlled by a computer program.

5.3 Preliminary Results and Discussion

To evaluate the ability of the LID technique to perform depth profiling of thin films of ice, the H₂O LID desorption yield was measured for successive IR laser pulses. The IR laser remained at the same spatial location and consecutive laser pulses progressively removed small volumes of the ice film. The H₂O LID relative desorption yield versus the number of laser pulses obtained for samples of ~3000

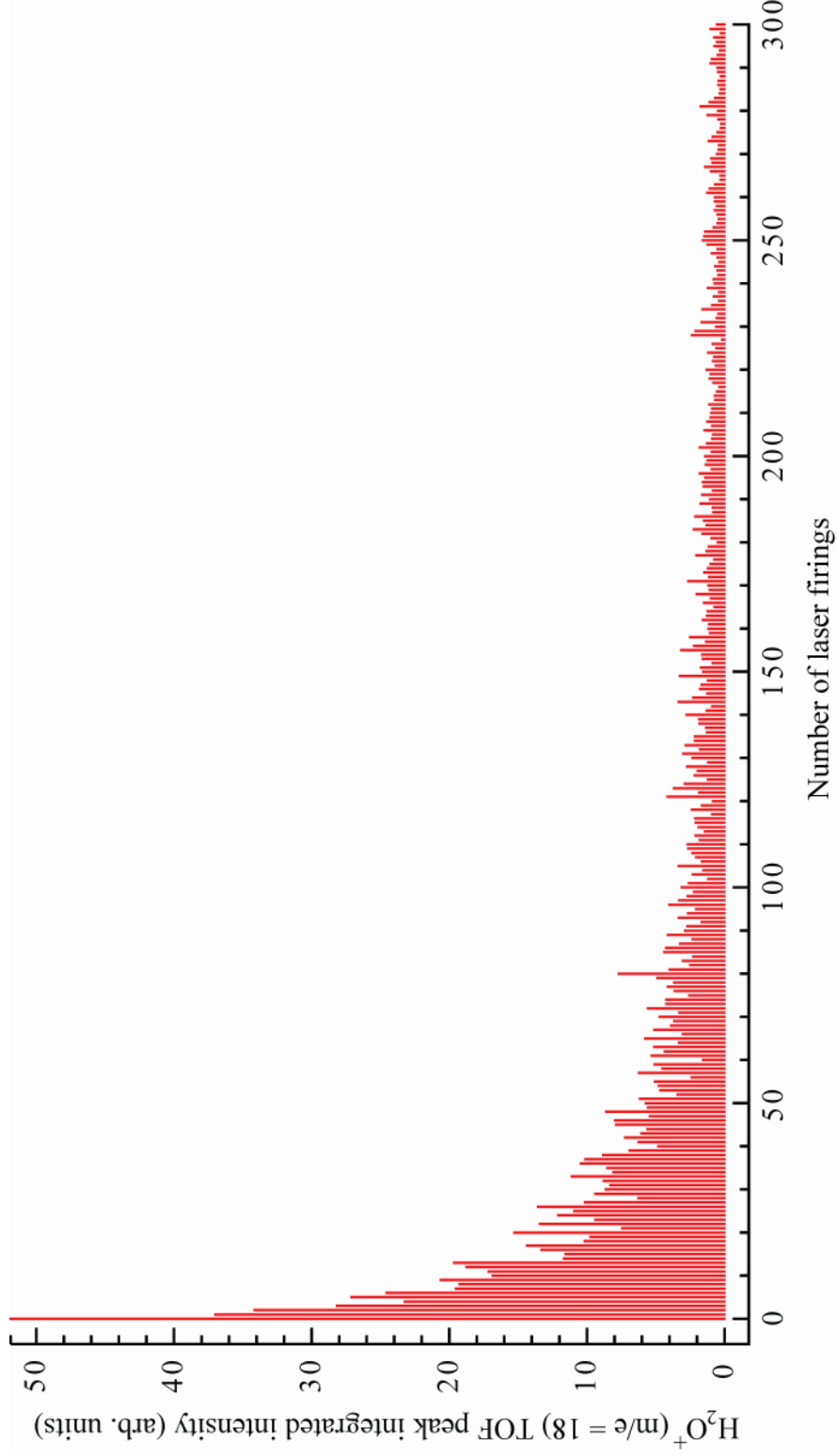


Figure 5.1. The H_2O LID relative desorption yield versus the number of laser pulses obtained for samples of ~3000 layers of ASW ice film (averaging results from 9 experiments). The IR laser energy was ~1.5 mJ.

layers ($\sim 1.2 \mu\text{m}$ thick) of ASW ice film is shown in Figure 5.1. The incident IR laser energy was $\sim 1.5 \text{ mJ}$ at the wavelength of $2.92 \mu\text{m}$ (3424 cm^{-1}). The temperature of the ice film during the LID probing was 100 K.

The H_2O LID signal decays to zero in ~ 300 consecutive laser pulses (Figure 5.1). The first laser pulse removes $\sim 5\%$ (150 layers) of the ice film while $\sim 30\%$ (900 layers) and $\sim 80\%$ (2400 layers) of the ice film are removed during first 10 and 100 consecutive laser pulses respectively. This gives the average desorption rate of ~ 30 molecules/pulse. George and coworkers observed similar behavior for $1\text{-}\mu\text{m}$ -thick crystalline ice films [17-21]. They proposed that the "tail" region of the LID signal can be qualitatively understood in terms of the optical penetration depth of the laser radiation and the efficient thermal transfer to the underlying substrate.

Ice films that are thinner than the optical penetration depth of the IR radiation absorb only a fraction of the IR laser radiation. In this case, the H_2O desorption yield will decrease due to a decrease in the energy transferred to the ice from the laser radiation. Thus, the H_2O LID signal should decrease as the ice film thickness decreases upon LID removal of water overlayers. The optical penetration depth of the IR radiation at $\lambda = 2.92 \mu\text{m}$ is

$$p = \lambda / 4\pi k, \quad (5.1)$$

where k is the imaginary refractive index of the media for this wavelength. The imaginary refractive indexes of water and crystalline ice are 0.28 and 0.21, respectively [22,23]. This gives penetration depth of the IR radiation $\sim 1.1 \mu\text{m}$ for crystalline ice and $\sim 0.84 \mu\text{m}$ for liquid water. The k value for amorphous ice is not

reported but considering that the IR absorbance of amorphous ice at $\lambda = 2.92 \mu\text{m}$ is approximately twice greater than the IR absorbance of crystalline ice [24], the optical penetration depth of the amorphous ice can be estimated as roughly $0.6 \mu\text{m}$. It is also plausible that the H₂O LID signal may be affected by dynamic changes in the optical penetration depth during a radiation-induced ice phase change. These ice phase change can happen either during the same laser pulse or previous laser pulses, but this effect is hard to estimate.

The average heat diffusion distance in ice, \bar{x} , can be estimated using the formula [19,25]

$$\bar{x} = \sqrt{4Dt}, \quad (5.2)$$

where D is the thermal diffusion coefficient, and t is the laser pulse duration. The thermal diffusion coefficient is given by [25]

$$D = \kappa / \rho C_p, \quad (5.3)$$

where κ is the ice thermal conductivity, ρ is the ice density, and C_p is the ice heat capacity. Using published values of the ice thermal conductivity ($\sim 1 \times 10^{-3} \text{ W/cmK}$), density ($\sim 0.9 \text{ g/cm}^3$), and heat capacity ($\sim 1 \text{ J/gK}$) [26-29], the thermal diffusion coefficient is $\sim 1.1 \times 10^6 \mu\text{m}^2/\text{s}$. This value is used in Equation 5.2 to give an average thermal diffusion distance of $0.2 \mu\text{m}$ for a 10 ns laser pulse duration. As a result, for ice film thickness $\gg 0.2 \mu\text{m}$, the laser heating remains localized in the ice on the time scale of the laser pulse duration. However, if the ice film thickness is smaller or comparable to the thermal transfer distance of $0.2 \mu\text{m}$, the underlying

substrate would act as an effective thermal energy sink resulting in reduced LID signal. Additionally, under these conditions, irradiated volume of ice will cool quickly (in roughly $< 1 \mu\text{s}$) after the IR laser pulse. The radiation-induced ice phase changes (and/or morphological changes) that happen either during the same laser pulse or previous laser pulses might significantly affect the ice thermal properties, and thus the attenuation of the LID signal.

Information about the duration of the desorption process, velocity distribution of desorbed molecules, temperature of the desorbed species, and hopefully the mechanism of desorption can be obtained from the time-of-flight distribution of desorbing water molecules. Figure 5.2 shows the sequence of 96 TOF mass spectra (5 μs period) of water desorbing from the ASW film (~ 3000 layers) following the IR laser pulse (1.5 mJ) at time zero. This collection of TOF spectra is referred to, for simplicity, as the temporal distribution of desorbed water molecules. The inset in Figure 5.2 shows an expanded scale of one TOF spectrum from the sequence. All the peaks are assigned to ionization products of water in the TOF electron impact ionizer. The measured temporal distribution is very wide (Figure 5.2) and thus it is unfeasible to infer from it directly the duration of the LID event itself, which is probably $< 100 \text{ ns}$.

Figure 5.3 shows the velocity distribution of water molecules desorbing from the ASW film (~ 3000 layers) following the IR laser pulse (1.5 mJ) at time zero. The velocity distribution of water molecules was obtained by integrating each H_2O^+ peak from the temporal profile (Figure 5.1) and multiplying the area by the

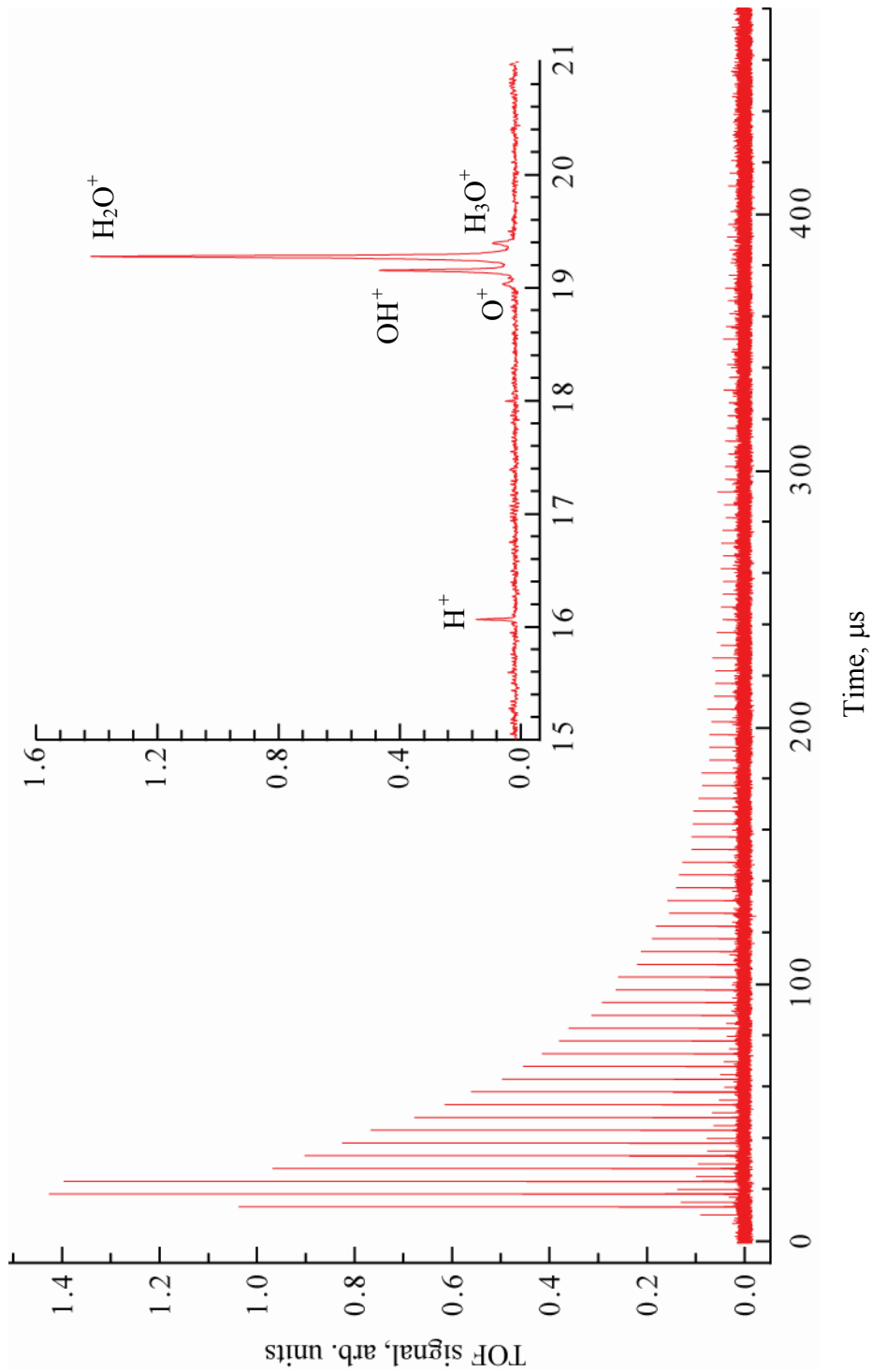


Figure 5.2. A sequence of 96 TOF mass spectra (5 μ s intervals) of water desorbing from the ASW film (\sim 3000 layers) following the IR laser pulse (1.5 mJ) at time zero. The inset shows an expanded scale of a single TOF spectrum from the sequence with masses assigned.

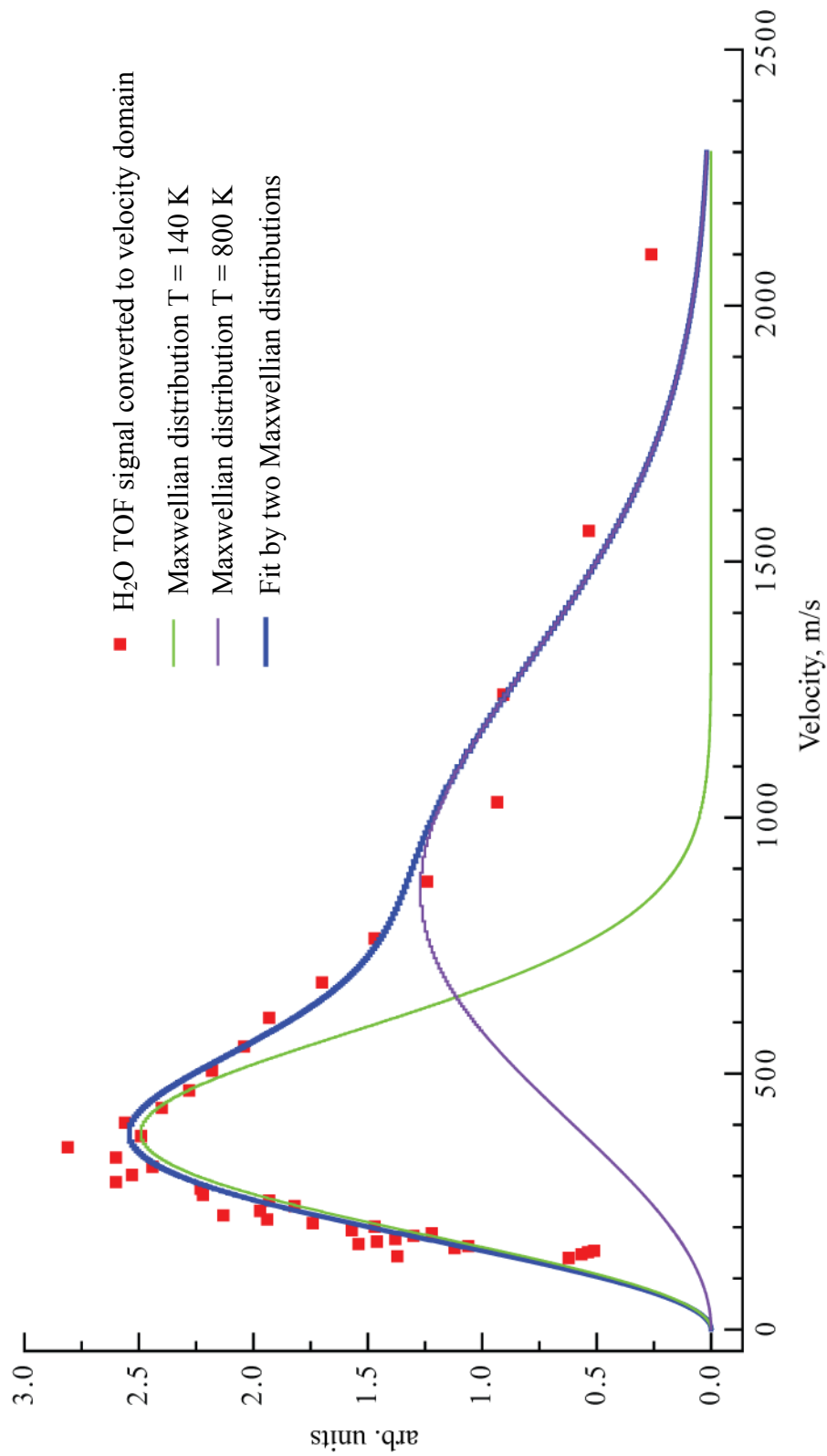


Figure 5.3. The velocity distribution of water molecules desorbing from the ASW film (~3000 layers) following the IR laser pulse (1.5 mJ) at time zero. The smooth thick line shows the best fit by a combination of two Maxwellian distributions.

Jacobian for transformation from time to velocity space ($\text{const} \cdot t^2$), where t is the time. The velocity v corresponding to each integrated peak (point) is calculated using $v = (0.03 \text{ m})/t$ where 0.03 m is the distance from the surface to the ionizer region of the TOF mass spectrometer. The flight time from the ionizer to the detector is negligible ($\sim 4 \mu\text{s}$). The velocity distribution of the desorbed water molecules can be analyzed as a combination of thermal Maxwellian velocity distributions with different temperatures.

Several studies of the evaporation kinetics of ice and supercooled water jets [30-32] reported that the velocity distribution of thermally desorbed water molecules at nearly collision-free conditions is the floating Maxwellian distribution [30]:

$$f(v)dv \sim v^2 \exp\left(-\frac{m(v-u)^2}{2k_B T_S}\right), \quad (5.4)$$

where v is the molecular thermal velocity, T_S is the local surface temperature, u is the average flow velocity (for supersonic expansion correction), and k_B is the Boltzmann constant. Furthermore, the floating Maxwellian distribution is commonly used to describe the velocity distribution of molecules ejected in laser ablation [33,34].

The thick solid line in Figure 5.3 shows a fit of the experimental velocity distribution of desorbed water molecules with a combination of two Maxwellian velocity distributions. In this fit, the average flow velocity is found to be zero for both Maxwellian distributions. The surface temperatures obtained from the fit are approximately 140 K and 800 K. However, laser ablation studies show that quite

often it is difficult to correlate the temperatures and stream velocities from the Maxwellian fit with meaningful physical parameters of the system [33,34].

The local temperature of the ice during desorption can be estimated by considering the thermal desorption kinetics of the ice film. The thermal desorption rate of ice is roughly independent of the ice sample thickness and sample history [32], and it demonstrates approximately Arrhenius behavior (often called zero-order desorption kinetics [35]) with an effective activation energy of ~ 50 kJ/mol at $T = 100 - 273$ K [32]:

$$-\frac{d\Theta}{dt} = \nu_0 \exp\left(-\frac{50 \text{ kJ/mol}}{RT}\right), \quad (5.5)$$

where $d\Theta/dt$ (monolayer/s) is the ice desorption rate, T is the surface temperature, R ($8.31 \text{ Jmol}^{-1}\text{K}^{-1}$) is the ideal gas constant, and ν_0 is typically $\sim 10^{13} \text{ s}^{-1}$ [32]. The average heat diffusion distance is about $0.7 \text{ }\mu\text{m}$ for a 100 ns time span. This is comparable to the thickness of 3000 layers ice film and thus the ice film will cool significantly in time less than 100 ns after the laser pulse. Cooling will greatly reduce desorption of water molecules after 100 ns due to Arrhenius character of the desorption rate. Therefore, assuming that $\Delta\Theta \sim 30 \text{ layers}$ (average desorption rate from the analysis of Figure 5.1) and $\Delta t \sim 100 \text{ ns}$ (upper estimate for the desorption time) desorption kinetics yield an estimate of the local ice film temperature of ~ 580 K.

The large value of the surface temperature estimate suggests that the ice undergoes phase changes and possibility becomes a liquid before it desorbs.

Several other studies also reported possible melting of ice induced by laser radiation heating [17,36]. Kubota et al. observed change in the sum frequency generation (SFG) spectrum of the D₂O crystalline ice residing on CO/Pt(111) substrate upon irradiating the substrate with the NIR pump laser [36]. The authors attributed changes in the D₂O SFG spectrum to the melting of the ice due to substrate heating [36]. Geroge and coworkers measured the H₂O LID signal from micrometer-thick crystalline ice films as a function of laser wavelength [17]. They observed that H₂O LID IR spectrum resembled the IR absorption spectrum of liquid water. This was explained by the melting of the ice film [17].

The evidence for ice melting during the LID process in crystalline ice brings up the question whether the amorphous ice becomes liquid without the intermediate crystallization steps. The ASW crystallization rate constant is governed by an Arrhenius dependence on temperature [10,37]. The heating rate of the ice by the IR laser is $\sim 10^{10}$ K/s, which is much higher than the crystallization rate of the amorphous ice at 165 K. Chonde et al. observed rapid crystallization of ASW delayed to 205 K (instead of 165 K in equilibrium conditions) using an ultrafast scanning microcalorimetry apparatus with heating rates $\sim 10^5$ K/s [38]. Therefore it is likely that the ASW film might melt during the LID rapid heating before a significant fraction has time to crystallize. This hypothesis can be studied in more detail in future experiments by utilizing probe molecules such as CO₂.

According to the LID desorption yield studies (Figure 5.1), only a fraction of the irradiated ice film desorbs. The irradiation region is several times larger than

the actual thickness of the ice that is removed during LID. So far it is not clear what happens in this region and regions adjacent to it. This also can be investigated by doping the ice film with CO₂ probe molecules.

The presence of cold water molecules in the H₂O LID signal (Figure 5.3 low temperature Maxwellian fit) does not agree with the ice melting and desorption rate analysis. One possible explanation invokes the breaking of water molecules through the crust of solid ice in a manner similar to the "molecular volcano" described above, but further experiments must be performed to investigate this.

5.4 Future Work

Preliminary study presented above has shown that the LID technique provides a means of depth-profiling analysis of thin ice films. The LID desorption signal in addition to the information about the molecular composition of the ice film contained information about the duration of the desorption process, velocity distribution of desorbed molecules, and temperature of the desorbed species. Our preliminary studies have indicated that the ice film heats up very quickly upon the laser irradiation and undergoes fast phase changes (possibly crystallization, transition to supercooled water, and melting). The LID process is still little understood despite the recent progress made in this field of study. The experiments started in this work have many interesting features left to explore. Some of the unanswered questions are: what ice film phase changes are induced by the laser radiation, and what are the temperatures for these phase changes. Another

intriguing issue that needs to be addressed is the presence of thermally cold (slow) water molecules in the water LID signal. Additional set of goals in continuing project is to study transport, phase changes, and flow in novel model ice systems obtained by IR laser patterning of the ASW films.

Amorphous solid water films are capable of influencing the desorption characteristics of certain molecules deposited onto their surfaces or codeposited during their formation [24,39-41]. Most of the experimental results are consistent with the idea that thermally induced structural changes in ASW films trap molecules residing within ASW, and they inhibit the release of these molecules until ASW crystallization and sublimation of the crystallized ice [24,39-42]. In addition, recent studies showed that molecules like CO₂ and N₂O can serve as probes of the ice film morphology and morphological changes that happen in the ASW ice film [24,42].

The introduction of probe molecules (like CO₂) into the ASW film and monitoring the release of probe molecules during the irradiation of the ice by the IR laser would present additional information about the laser-induced changes in the amorphous ice. For instance, the velocity distribution of probe molecules desorbing during LID would indicate the temperature during the release of trapped molecules from the ASW film. This would indicate either crystallization or melting of the ASW film.

The measurement of the desorption yield of probe molecules for several consequent laser pulses would show if there are any morphological changes in the

regions boundary to the LID region (region that is removed during LID process). For example, if the first laser pulse would result in crystallization of the boundary regions then probe molecules would be expelled from these boundary regions during the first laser pulse. Thus, the second laser pulse would result in lower intensity of the desorption signal of probe molecules. The estimate of the dimensions of the boundary regions that are affected by the LID process can be obtained by comparing the LID desorption signal of probe molecules for several consequent laser pulses.

The LID surface area is very small ($\sim 0.5 \text{ mm} \times 0.5 \text{ mm}$). Thus it is difficult to study LID induced changes in the ice film by FTIR or TPD techniques. This problem can be solved by translating the IR laser beam across the substrate and thus effectively irradiating the entire surface.

The LID signal is very small for thin ice films (< 40 layers). It is unclear if the IR radiation can result in desorption of such thin ice films. The FTIR studies of CO_2 -doped thin nanoscale ASW films can show if the IR laser radiation affects these films. The analysis of water and CO_2 IR spectral features would lead to information about how much of the ice film is left after irradiation and whether the ASW thin film undergoes phase changes during the laser irradiation.

The domains of crystalline ice evenly distributed throughout an ASW film and isolated regions of ASW evenly distributed on a supporting substrate represent novel model systems from which additional information about transport and flow in amorphous materials may be obtained. Crystalline domains or voids (empty spaces)

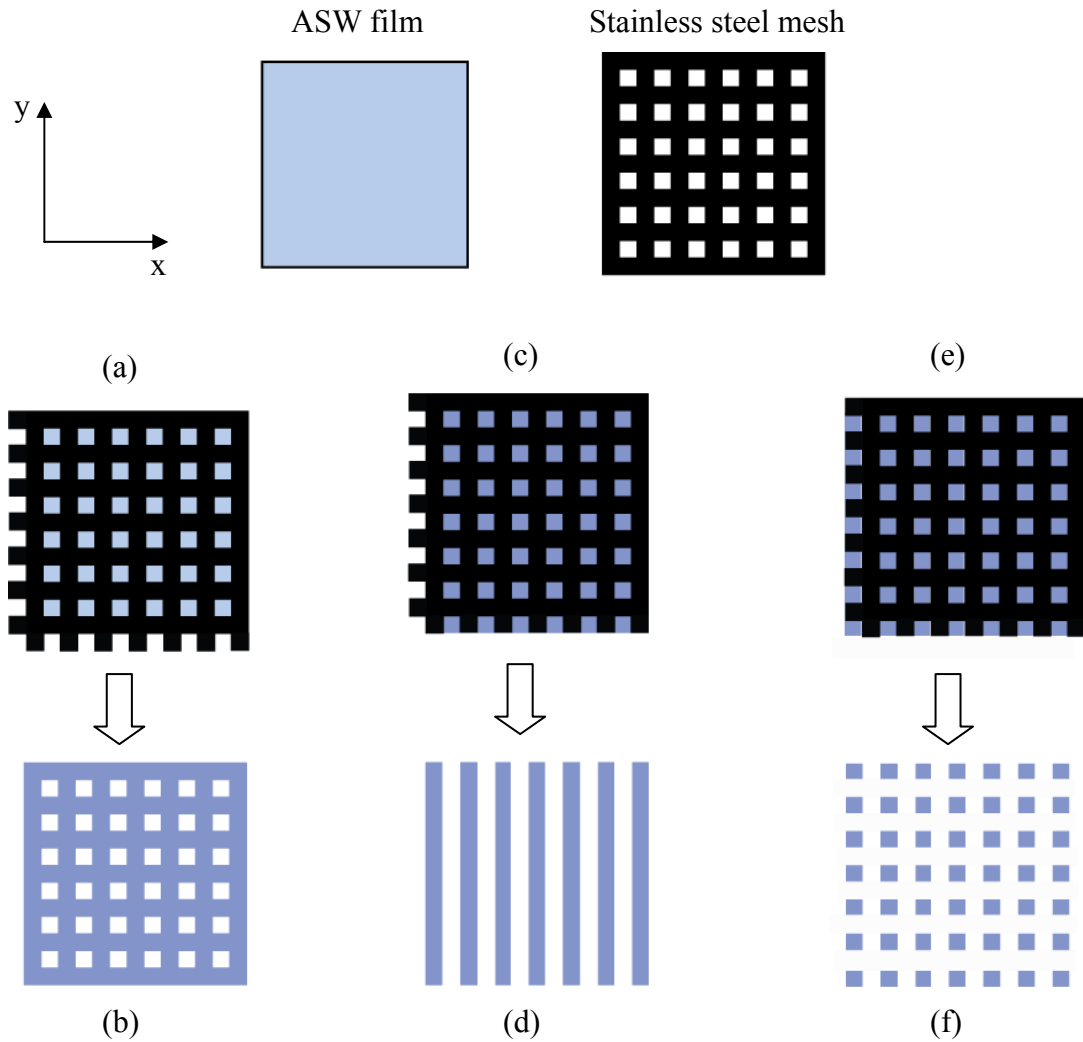


Figure 5.4. Fabrication of isolated regions of ASW on a supporting substrate. (a) Stainless steel mesh is placed in front of the ASW film, and the film is irradiated. (b) All the ASW in open areas desorb, leaving the structure shown in blue. (c), (d) To form isolated columns of ASW with the axes of the columns parallel to the y-axis shown, the mesh can be translated along the y-axis. After translation the substrate is irradiated to desorb any exposed ASW. (e), (f) To form isolated areas of ASW (blue squares), this process has to be repeated along x-axis.

within an ASW film can be created by irradiation of the ASW film surface with IR laser through a stainless steel wire mesh (see Figure 5.4 for details). These systems have a higher ratio of boundary to bulk H₂O molecules than in H₂O ice film and thus effects related to boundaries and surface can be more easily distinguished. Phenomena of participation of boundaries in phase transformations and dopants transport, lateral flow of amorphous materials and supercooled liquids can be addressed by studying these ice "nanoarrays". These structures can be probed using the LID technique or conventional FTIR. The mesh can be positioned to expose only the area of particular interest in the nanoarray.

One of the interesting and long-standing question, whether the water exhibits a glassy transition at ~135 K [14,43,44], can be addressed by monitoring the lateral flow between isolated regions of ASW evenly distributed on a supporting substrate. The ASW film is very stable at temperatures less than 120 K, and thus the isolated ASW regions will be stable at these temperatures. However, if the glass transition of amorphous ice indeed occurs at ~135 K then the boundaries of ASW regions should commence lateral spreading at temperatures higher than 135 K. The spreading of the ice nanoarrays upon annealing of the substrate can be checked by monitoring the LID signal from the empty spaces that did not have any water molecules at the beginning. CO₂ probe molecules can be used to gain more insights into the mechanism of the lateral spreading. Additionally, the ASW islands can be irradiated by the IR laser and possibly brought up very quickly to the melted state and then these "melts" should commence very efficient lateral spreading.

5.5 References

1. B.S. Berland, D.E. Brown, M.A. Tolbert, and S.M. George, *Geophys. Res. Lett.*, **22**, 3493, (1995).
2. P.V. Hobbs, *Ice Physics*, Claderon Press: Oxford, 1974.
3. L.J. Allamandola, S.A. Sandford, and G.J. Valero, *Icarus*, **76**, 225, (1988).
4. A. Bar-Nun, G. Herman, D. Laufer, and M.L. Rappaport, *Icarus*, **63**, 317, (1985).
5. P. Jenniskens and D.F. Blake, *Science*, **265**, 753, (1994).
6. J.D. Graham and J.T. Roberts, *J. Phys. Chem.*, **98**, 5974, (1994).
7. M.J. Molina, T.L. Tso, L.T. Molina, and F.C.Y. Wang, *Science*, **238**, 1253, (1987).
8. S. Solomon, *Nature*, **347**, 347, (1990).
9. D.E. Brown and S.M. George, *J. Phys. Chem.*, **100**, 15460, (1996).
10. Z. Dohnalek, G.A. Kimmel, R.L. Ciolli, K.P. Stevenson, R.S. Smith, and B.D. Kay, *J. Chem. Phys.*, **112**, 5932, (2000).
11. C. Girardet, P.N.M. Hoang, A. Marmier, and S. Picaud, *Phys. Rev. B*, **57**, 11931, (1998).
12. C. Girardet and C. Toubin, *Surface Science Reports*, **44**, 163, (2001).
13. A. Tabazadeh and R.P. Turco, *Science*, **260**, 1082, (1993).
14. C.A. Angell, *Chem. Rev.*, **102**, 2627, (2002).
15. C.A. Angell, *Annu. Rev. Phys. Chem.*, **55**, 559, (2004).
16. O. Mishima and H.E. Stanley, *Nature*, **396**, 329, (1998).
17. A. Krasnopoler and S.M. George, *J. Phys. Chem. B*, **102**, 788, (1998).
18. F.E. Livingston and S.M. George, *J. Phys. Chem. A*, **105**, 5155, (2001).
19. F.E. Livingston, J.A. Smith, and S.M. George, *Anal. Chem.*, **72**, 5590, (2000).

20. F.E. Livingston, J.A. Smith, and S.M. George, *J. Phys. Chem. A*, **106**, 6309, (2002).
21. F.E. Livingston, G.C. Whipple, and S.M. George, *J. Chem. Phys.*, **108**, 2197, (1998).
22. O.B. Toon, M.A. Tolbert, B.G. Koehler, A.M. Middlebrook, and J. Jordan, *Journal of Geophysical Research-Atmospheres*, **99**, 25631, (1994).
23. H.D. Downing and D. Williams, *J. Geophys. Res.*, **80**, 1656, (1975).
24. G. Kumi, S. Malyk, S. Hawkins, H. Reisler, and C. Wittig, *J. Phys. Chem. A*, **110**, 2097, (2006).
25. J.P. Holman, *Heat Transfer*, 9th Ed., McGraw-Hill: New York, 2002.
26. Y.P. Handa and D.D. Klug, *J. Phys. Chem.*, **92**, 3323, (1988).
27. O. Andersson and H. Suga, *Solid State Communications*, **91**, 985, (1994).
28. O. Andersson and H. Suga, *Phys. Rev. B*, **65**, 140201, (2002).
29. J. Hessinger, B.E. White, and R.O. Pohl, *Planetary and Space Science*, **44**, 937, (1996).
30. M. Faubel and T. Kisters, *Nature*, **339**, 527, (1989).
31. M. Faubel, S. Schlemmer, and J.P. Toennies, *Zeitschrift Fur Physik D-Atoms Molecules and Clusters*, **10**, 269, (1988).
32. V. Sadtchenko, M. Brindza, M. Chonde, B. Palmore, and R. Eom, *J. Chem. Phys.*, **121**, 11980, (2004).
33. F. Claeysens, S.J. Henley, and M.N.R. Ashfold, *J. Appl. Phys.*, **94**, 2203, (2003).
34. L.V. Zhigilei and B.J. Garrison, *Appl. Phys. Lett.*, **71**, 551, (1997).
35. K.W. Kolasinski, *Surface Science: Foundations of Catalysis and Nanoscience*, John Wiley & Sons Inc.: New York, 2002.
36. J. Kubota, A. Wada, S.S. Kano, and K. Domen, *Chem. Phys. Lett.*, **377**, 217, (2003).

37. R.S. Smith, C. Huang, E.K.L. Wong, and B.D. Kay, *Surf. Sci.*, **367**, L13, (1996).
38. M. Chonde, M. Brindza, and V. Sadtchenko, *J. Chem. Phys.*, **125**, 094501, (2006).
39. P. Ayotte, R.S. Smith, K.P. Stevenson, Z. Dohnalek, G.A. Kimmel, and B.D. Kay, *J. Geophys. Res. Plan.*, **106**, 33387, (2001).
40. A. Bar-Nun, J. Dror, E. Kochavi, and D. Laufer, *Phys. Rev. B*, **35**, 2427, (1987).
41. M.P. Collings, M.A. Anderson, R. Chen, J.W. Dever, S. Viti, D.A. Williams, and M.R.S. McCoustra, *Mon. Not. R. Astron. Soc.*, **354**, 1133, (2004).
42. S. Malyk, G. Kumi, H. Reisler, and C. Wittig, *J. Phys. Chem. A*, **111**, 13365, (2007).
43. S.M. McClure, D.J. Safarik, T.M. Truskett, and C.B. Mullins, *J. Phys. Chem. B*, **110**, 11033, (2006).
44. R.S. Smith and B.D. Kay, *Nature*, **398**, 788, (1999).

Bibliography

- L.J. Allamandola, S.A. Sandford, and G.J. Valero, *Icarus*, **76**, 225, (1988).
- L.J. Allamandola, S.A. Sandford, A.G.G.M. Tielens, and T.M. Herbst, *Astrophys. J.*, **399**, 134, (1992).
- O. Andersson and H. Suga, *Solid State Communications*, **91**, 985, (1994).
- O. Andersson and H. Suga, *Phys. Rev. B*, **65**, 140201, (2002).
- O. Andersson and A. Inaba, *Phys. Chem. Chem. Phys.*, **7**, 1441, (2005).
- P.U. Andersson, M.B. Nagard, G. Witt, and J.B.C. Pettersson, *J. Phys. Chem. A*, **108**, 4627, (2004).
- C.A. Angell, *Annu. Rev. Phys. Chem.*, **34**, 593, (1983).
- C.A. Angell, *Science*, **267**, 1924, (1995).
- C.A. Angell, *Chem. Rev.*, **102**, 2627, (2002).
- C.A. Angell, *Annu. Rev. Phys. Chem.*, **55**, 559, (2004).
- P. Ayotte, R.S. Smith, K.P. Stevenson, Z. Dohnalek, G.A. Kimmel, and B.D. Kay, *J. Geophys. Res. Plan.*, **106**, 33387, (2001).
- A. Bar-Nun, G. Herman, D. Laufer, and M.L. Rappaport, *Icarus*, **63**, 317, (1985).
- A. Bar-Nun, J. Dror, E. Kochavi, and D. Laufer, *Phys. Rev. B*, **35**, 2427, (1987).
- A. Bar-Nun, J. Dror, E. Kochavi, D. Laufer, D. Kovetz, and T. Owen, *Origins of Life and Evolution of the Biosphere*, **16**, 220, (1986).
- A. Bar-Nun and I. Kleinfeld, *Icarus*, **80**, 243, (1989).
- A. Bar-Nun, I. Kleinfeld, and E. Kochavi, *Phys. Rev. B*, **38**, 7749, (1988).
- R.A. Baragiola, *Microporous Amorphous Water Ice Thin Films: Properties and Their Astronomical Implications*, in *Water in Confining Geometries*, V. Buch and J.P. Devlin, Editors; Springer: Berlin, 2003.
- B.S. Berland, D.E. Brown, M.A. Tolbert, and S.M. George, *Geophys. Res. Lett.*, **22**, 3493, (1995).

- D. Blake, L. Allamandola, S. Sandford, D. Hudgins, and F. Freund, *Science*, **254**, 548, (1991).
- D.J. Brink, H.P. Burger, T.N. Dekock, J.A. Strauss, and D.R. Preussler, *Journal of Physics D-Applied Physics*, **19**, 1421, (1986).
- S. Briquez, A. Lakhlifi, S. Picaud, and C. Girardet, *Chem. Phys.*, **194**, 65, (1995).
- D.E. Brown and S.M. George, *J. Phys. Chem.*, **100**, 15460, (1996).
- V. Buch and J.P. Devlin, *Introduction*, in *Water in Confining Geometries*, V. Buch and J.P. Devlin, Editors; Springer: Berlin, 2003.
- E.F. Burton and W.F. Oliver, *Proceedings Royal Society*, **A153**, 166, (1935).
- W. Carnuth and T. Trickl, *Rev. Sci. Instrum.*, **65**, 3324, (1994).
- M. Chonde, M. Brindza, and V. Sadtchenko, *J. Chem. Phys.*, **125**, 094501, (2006).
- F. Claeysens, S.J. Henley, and M.N.R. Ashfold, *J. Appl. Phys.*, **94**, 2203, (2003).
- M.P. Collings, J.W. Dever, H.J. Fraser, and M.R.S. McCoustra, *Astrophysics and Space Science*, **285**, 633, (2003).
- M.P. Collings, M.A. Anderson, R. Chen, J.W. Dever, S. Viti, D.A. Williams, and M.R.S. McCoustra, *Mon Not R Astron Soc*, **354**, 1133, (2004).
- J.P. Devlin, *J. Phys. Chem.*, **96**, 6185, (1992).
- Z. Dohnalek, L.C. Ryan, A.K. Greg, K.P. Stevenson, R.S. Smith, and D.K. Bruce, *J. Chem. Phys.*, **110**, 5489, (1999).
- Z. Dohnalek, G.A. Kimmel, R.L. Ciolli, K.P. Stevenson, R.S. Smith, and B.D. Kay, *J. Chem. Phys.*, **112**, 5932, (2000).
- Z. Dohnalek, G.A. Kimmel, P. Ayotte, R.S. Smith, and B.D. Kay, *J. Chem. Phys.*, **118**, 364, (2003).
- H.D. Downing and D. Williams, *J. Geophys. Res*, **80**, 1656, (1975).
- M. Faubel, S. Schlemmer, and J.P. Toennies, *Zeitschrift Fur Physik D-Atoms Molecules and Clusters*, **10**, 269, (1988).
- M. Faubel and T. Kisters, *Nature*, **339**, 527, (1989).

- I. Fischer and T. Schultz, *Applied Physics B-Lasers and Optics*, **64**, 15, (1997).
- M. Fisher and J.P. Devlin, *J. Phys. Chem.*, **99**, 11584, (1995).
- F. Fleyfel and J.P. Devlin, *J. Phys. Chem.*, **95**, 3811, (1991).
- F. Franks, *The properties of Aqueous Solutions at Subzero Temperatures*, in *Water: A comprehensive treatise*, F. Franks, Editor; Plenum Press: New York, 1982.
- J.A. Ghormley, *J. Chem. Phys.*, **46**, 1321, (1967).
- J.A. Ghormley, *J. Chem. Phys.*, **48**, 503, (1968).
- C. Girardet, P.N.M. Hoang, A. Marmier, and S. Picaud, *Phys. Rev. B*, **57**, 11931, (1998).
- C. Girardet and C. Toubin, *Surface Science Reports*, **44**, 163, (2001).
- S. Godin, G. Megie, and J. Pelon, *Geophys. Res. Lett.*, **16**, 547, (1989).
- J.D. Graham and J.T. Roberts, *J. Phys. Chem.*, **98**, 5974, (1994).
- J.D. Graham, J.T. Roberts, L.A. Brown, and V. Vaida, *J. Phys. Chem.*, **100**, 3115, (1996).
- P. Griffiths and J.A. De Haseth, *Fourier Transform Infrared Spectrometry*, John Wiley and Sons, Inc.: New York, 1986.
- C. Guntermann, V. Schulzvondergathen, and H.F. Dobebe, *Appl. Opt.*, **28**, 135, (1989).
- W. Hage, A. Hallbrucker, E. Mayer, and G.P. Johari, *J. Chem. Phys.*, **100**, 2743, (1994).
- W. Hage, A. Hallbrucker, E. Mayer, and G.P. Johari, *J. Chem. Phys.*, **103**, 545, (1995).
- W. Hagen, A.G.G.M. Tielens, and J.M. Greenberg, *Chem. Phys.*, **56**, 367, (1981).
- A. Hallbrucker, E. Mayer, and G.P. Johari, *J. Phys. Chem.*, **93**, 7751, (1989).
- Y.P. Handa, O. Mishima, and E. Whalley, *J. Chem. Phys.*, **84**, 2766, (1986).
- Y.P. Handa and D.D. Klug, *J. Phys. Chem.*, **92**, 3323, (1988).

S. Hawkins, G. Kumi, S. Malyk, H. Reisler, and C. Wittig, *Chem. Phys. Lett.*, **404**, 19, (2005).

S.A. Hawkins, *Fourier transform infrared spectroscopy and temperature programmed desorption of water thin films on the MgO (100) surface*, Ph. D. Thesis, Department of Chemistry, University of Southern California, Los Angeles, 2004.

V.E. Henrich and P.A. Cox, *The Surface Science of Metal Oxides*, Cambridge University Press: Cambridge, 1994.

J. Hernandez, N. Uras, and J.P. Devlin, *J. Phys. Chem. B*, **102**, 4526, (1998).

J. Hessinger, B.E. White, and R.O. Pohl, *Planetary and Space Science*, **44**, 937, (1996).

P.V. Hobbs, *Ice Physics*, Claderon Press: Oxford, 1974.

L. Hodgson, G. Ziegler, H. Ferkel, H. Reisler, and C. Wittig, *Canadian Journal of Chemistry-Revue Canadienne De Chimie*, **72**, 737, (1994).

L.K. Hodgson, *Photodissociation, molecule-surface collision-induced dissociation and direct adsorbate photolysis of nitroso molecules*, Ph. D. Thesis, Department of Chemistry, University of Southern California, Los Angeles, 1993.

A.B. Horn, J.R. Sodeau, T.B. Roddis, and N.A. Williams, *J. Phys. Chem. A*, **102**, 6107, (1998).

R.L. Hudson and B. Donn, *Icarus*, **94**, 326, (1991).

P. Jenniskens and D.F. Blake, *Science*, **265**, 753, (1994).

P. Jenniskens and D.F. Blake, *Science*, **265**, 753, (1994).

P. Jenniskens and D.F. Blake, *The Astrophysical Journal*, **473**, 1104, (1996).

P. Jenniskens, S.F. Banham, D.F. Blake, and M.R.S. McCoustra, *J. Chem. Phys.*, **107**, 1232, (1997).

G.P. Johari, A. Hallbrucker, and E. Mayer, *Nature*, **330**, 552, (1987).

G.P. Johari, *J. Phys. Chem. B*, **102**, 4711, (1998).

G.A. Kimmel, K.P. Stevenson, Z. Dohnalek, R.S. Smith, and B.D. Kay, *J. Chem. Phys.*, **114**, 5284, (2001).

- G.A. Kimmel, K.P. Stevenson, Z. Dohnalek, R.S. Smith, and B.D. Kay, *J. Chem. Phys.*, **114**, 5284, (2001).
- K.W. Kolasinski, *Surface Science: Foundations of Catalysis and Nanoscience*, John Wiley & Sons Inc.: New York, 2002.
- M. Korolik, M.M. Suchan, M.J. Johnson, D.W. Arnold, H. Reisler, and C. Wittig, *Chem. Phys. Lett.*, **326**, 11, (2000).
- A. Kouchi, *Journal of Crystal Growth*, **99**, 1220, (1990).
- A. Kouchi, J.M. Greenberg, T. Yamamoto, and T. Mukai, *Astrophys. J.*, **388**, L73, (1992).
- A. Kouchi, T. Yamamoto, T. Kozasa, T. Kuroda, and J.M. Greenberg, *Astronomy and Astrophysics*, **290**, 1009, (1994).
- A. Krasnopoler and S.M. George, *J. Phys. Chem. B*, **102**, 788, (1998).
- J. Kruger and W.J. Ambs, *Journal of the Optical Society of America*, **49**, 1195, (1959).
- J. Kubota, A. Wada, S.S. Kano, and K. Domen, *Chem. Phys. Lett.*, **377**, 217, (2003).
- G. Kumi, S. Malyk, S. Hawkins, H. Reisler, and C. Wittig, *J. Phys. Chem. A*, **110**, 2097, (2006).
- G. Kumi, *Fourier transform infrared studies of guest-host interactions in ice*, Ph. D. Thesis, Department of Chemistry, University of Southern California, Los Angeles, 2007.
- D.G. Lancaster and J.M. Dawes, *Opt. Commun.*, **120**, 307, (1995).
- D. Laufer, E. Kochavi, and A. Bar-Nun, *Phys. Rev. B*, **36**, 9219, (1987).
- D.R. Lide, Editor, *CRC Handbook of Chemistry and Physics 75th Edition*, CRC Press: New York, 1998.
- F.E. Livingston, G.C. Whipple, and S.M. George, *J. Chem. Phys.*, **108**, 2197, (1998).
- F.E. Livingston, J.A. Smith, and S.M. George, *Anal. Chem.*, **72**, 5590, (2000).
- F.E. Livingston and S.M. George, *J. Phys. Chem. A*, **105**, 5155, (2001).

- F.E. Livingston, J.A. Smith, and S.M. George, *J. Phys. Chem. A*, **106**, 6309, (2002).
- T.R. Loree, R.C. Sze, D.L. Barker, and P.B. Scott, *Ieee Journal of Quantum Electronics*, **15**, 337, (1979).
- S. Malyk, G. Kumi, H. Reisler, and C. Wittig, *J. Phys. Chem. A*, **111**, 13365, (2007).
- C. Manca, C. Martin, and P. Roubin, *Chem. Phys. Lett.*, **364**, 220, (2002).
- C. Manca, C. Martin, and P. Roubin, *Chem. Phys.*, **300**, 53, (2004).
- C. Manca, C. Martin, and P. Roubin, *Chem. Phys.*, **300**, 53, (2004).
- E. Mayer and R. Pletzer, *Nature*, **319**, 298, (1986).
- S.M. McClure, E.T. Barlow, M.C. Akin, D.J. Safarik, T.M. Truskett, and C.B. Mullins, *J. Phys. Chem. B*, **110**, 17987, (2006).
- S.M. McClure, D.J. Safarik, T.M. Truskett, and C.B. Mullins, *J. Phys. Chem. B*, **110**, 11033, (2006).
- O. Mishima, L.D. Calvert, and E. Whalley, *Nature*, **310**, 393, (1984).
- O. Mishima, L.D. Calvert, and E. Whalley, *Nature*, **314**, 76, (1985).
- O. Mishima and H.E. Stanley, *Nature*, **396**, 329, (1998).
- M.J. Molina, T.L. Tso, L.T. Molina, and F.C.Y. Wang, *Science*, **238**, 1253, (1987).
- A.H. Narten, C.G. Venkatesh, and S.A. Rice, *J. Chem. Phys.*, **64**, 1106, (1976).
- G. Natesco and A. Bar-Nun, *Icarus*, **148**, 456, (2000).
- J.A. Nuth, H.G.M. Hill, and G. Kletetschka, *Nature*, **406**, 275, (2000).
- M.A. Ovchinnikov and C.A. Wight, *J. Chem. Phys.*, **99**, 3374, (1993).
- R. Pletzer and E. Mayer, *J. Chem. Phys.*, **90**, 5207, (1989).
- R. Pletzer and E. Meyer, *J. Chem. Phys.*, **90**, 5207, (1989).
- D. Rasmusse and A. Mackenzi, *J. Phys. Chem.*, **75**, 967, (1971).

- H.H. Richardson, P.J. Wooldridge, and J.P. Devlin, *J. Chem. Phys.*, **83**, 4387, (1985).
- K.H. Rieder, *Surf. Sci.*, **118**, 57, (1982).
- N.J. Sack and R.A. Baragiola, *Physical Review B*, **48**, (1993).
- V. Sadtchenko, K. Knutsen, C.F. Giese, and W.R. Gentry, *J. Phys. Chem. B*, **104**, 4894, (2000).
- V. Sadtchenko, M. Brindza, M. Chonde, B. Palmore, and R. Eom, *J. Chem. Phys.*, **121**, 11980, (2004).
- S.A. Sandford and L.J. Allamandola, *Icarus*, **76**, 201, (1988).
- S.A. Sandford and L.J. Allamandola, *Astrophys. J.*, **355**, 357, (1990).
- S.A. Sandford and L.J. Allamandola, *J. Astrophys.*, **355**, 357, (1990).
- N. Sartori, J. Bednar, and J. Dubochet, *Journal of Microscopy-Oxford*, **182**, 163, (1996).
- M.G. Sceats and S.A. Rice, in *Water: A Comprehensive Treatise*, F. Franks, Editor; Plenum Press: New York, 1982.
- M.G. Sceats and S.A. Rice, *Amorphous Solid Water and Its Relationship to Liquid Water: A Random Network Model for Water*, in *Water: A comprehensive treatise*, F. Franks, Editor; Plenum Press: New York, 1982.
- J.E. Schaff and J.T. Roberts, *Langmuir*, **14**, 1478, (1998).
- B. Schmitt, J. Ocampo, and J. Klinger, *Journal De Physique*, **48**, 519, (1987).
- K. Sentrayan, A. Michael, and V. Kushawaha, *Applied Physics B-Lasers and Optics*, **62**, 479, (1996).
- Sheikh, II and P.D. Townsend, *Journal of Physics E-Scientific Instruments*, **6**, 1170, (1973).
- D.A. Skoog and J.L. Leary, *Principles of Instrumental Analysis*, Harcourt Brace College Publishers: Fort Worth, 1992.
- B.C. Smith, *Fourier Transform Infrared Spectroscopy*, CRC Press: Boca Raton, 1996.

- R.S. Smith, C. Huang, E.K.L. Wong, and B.D. Kay, *Surf. Sci.*, **367**, L13, (1996).
- R.S. Smith, C. Huang, and B.D. Kay, *J. Phys. Chem. B*, **101**, 6123, (1997).
- R.S. Smith, C. Huang, E.K.L. Wong, and B.D. Kay, *Phys. Rev. Lett.*, **79**, 909, (1997).
- R.S. Smith and B.D. Kay, *Surf. Rev. Lett.*, **4**, 781, (1997).
- R.S. Smith and B.D. Kay, *Surf. Rev. Lett.*, **4**, 781, (1997).
- R.S. Smith and B.D. Kay, *Nature*, **398**, 788, (1999).
- R.S. Smith, Z. Dohnalek, G.A. Kimmel, K.P. Stevenson, and B.D. Kay, *Chem. Phys.*, **258**, 291, (2000).
- R.S. Smith, Z. Dohnalek, G.A. Kimmel, G. Teeter, P. Ayotte, J.L. Daschbach, and B.D. Kay, *Molecular Beam Studies of Nanoscale Films of Amorphous Solid Water*, in *Water in Confining Geometries*, V. Buch and J.P. Devlin, Editors; Springer: Berlin, 2003.
- R. Smoluchowski, *Science*, **201**, 809, (1978).
- S. Solomon, *Nature*, **347**, 347, (1990).
- D. Stern, C.A. Puliafito, E.T. Dobi, and W.T. Reidy, *Ophthalmology*, **95**, 1434, (1988).
- K.P. Stevenson, G.A. Kimmel, Z. Dohnalek, R.S. Smith, and B.D. Kay, *Science*, **283**, 1505, (1999).
- K.P. Stevenson, G.A. Kimmel, Z. Dohnalek, R.S. Smith, and B.D. Kay, *Science*, **283**, 1505, (1999).
- M.M. Suchan, *Molecules-surface interactions in HCl/MgO and Water/MgO Systems*, Ph. D. Thesis, Department of Chemistry, University of Southern California, Los Angeles, 2001.
- A. Tabazadeh and R.P. Turco, *Science*, **260**, 1082, (1993).
- O.B. Toon, M.A. Tolbert, B.G. Koehler, A.M. Middlebrook, and J. Jordan, *Journal of Geophysical Research-Atmospheres*, **99**, 25631, (1994).
- W.R. Trutna and R.L. Byer, *Appl. Opt.*, **19**, 301, (1980).

C.A. Tulk, C.J. Benmore, J. Urquidi, D.D. Klug, J. Neuefeind, B. Tomberli, and P.A. Egelstaff, *Science*, **297**, 1320, (2002).

Z.Y. Wang and S.K. Zhou, *Progress in Chemistry*, **16**, 49, (2004).

H. Yamada and W.B. Person, *J. Chem. Phys.*, **41**, 2478, (1964).

J. Yates, J. T., *Experimental Innovations in Surface Science*, AIP Press Springer-Verlag: New York, 1998.

X.J. Yu and H.S. Kwok, *J. Appl. Phys.*, **93**, 4407, (2003).

Y.Z. Yue and C.A. Angell, *Nature*, **427**, 717, (2004).

R. Zallen, *The Physics of Amorphous Solids*, John Wiley and Sons, Inc.: New York, 1983.

L.V. Zhigilei and B.J. Garrison, *Appl. Phys. Lett.*, **71**, 551, (1997).